

General Disclaimer

One or more of the Following Statements may affect this Document

- This document has been reproduced from the best copy furnished by the organizational source. It is being released in the interest of making available as much information as possible.
- This document may contain data, which exceeds the sheet parameters. It was furnished in this condition by the organizational source and is the best copy available.
- This document may contain tone-on-tone or color graphs, charts and/or pictures, which have been reproduced in black and white.
- This document is paginated as submitted by the original source.
- Portions of this document are not fully legible due to the historical nature of some of the material. However, it is the best reproduction available from the original submission.

3 "Made available under NASA sponsorship
in the interest of the widest possible dis-
semination of Earth Resources Survey
Program information and without liability
for any use made thereof."

E76-10382

NASA-TM-X-72599

THE APPLICATION OF SATELLITE DATA IN THE DETERMINATION
OF OCEAN TEMPERATURES AND CLOUD CHARACTERISTICS
AND STATISTICS

Final Report of the Skylab Investigation

(E76-10382) THE APPLICATION OF SATELLITE
DATA IN THE DETERMINATION OF OCEAN
TEMPERATURES AND CLOUD CHARACTERISTICS AND
STATISTICS Final Report (NASA) 124 p HC
\$5.50

N76-27620

CSCL 04B G3/43 00382

Unclassified

GODDARD SPACE FLIGHT CENTER
Greenbelt, Maryland

Final Report of the Skylab Investigation

entitled

THE APPLICATION OF SATELLITE DATA IN THE DETERMINATION
OF OCEAN TEMPERATURES AND CLOUD CHARACTERISTICS
AND STATISTICS

Prepared by:

Dr. Robert J. Curran, GSFC, Code 911

Dr. Vincent V. Salomonson

Mr. William Shenk

enq

Original photography may be purchased from:
EROS Data Center
10th and Dakota Avenue
Sioux Falls, SD 57198

GODDARD SPACE FLIGHT CENTER
Greenbelt, Maryland

**ORIGINAL CONTAINS
COLOR ILLUSTRATIONS**

TABLE OF CONTENTS

	<u>Page</u>
I. Summary	1
A. Introduction	1
B. Statement of Work — Technical Approach	2
C. Instrumentation Used in the Investigation	3
D. Initial Processing of the Digital Data and Use of the Photographic Data	4
II. Technical Background and Results of Basic Studies.	7
A. General Background.	7
B. Radiometric Techniques	9
III. Results of Use of the Skylab Data and Its Comparison with Theory .	17
A. Cloud Altitude from 11 μ m Radiometry	17
B. Determination of Thermodynamic Phase	18
IV. Conclusions	25
Appendix 1 — S-191	A1-1
Appendix 2 (separate cover)	A2-1
Appendix 3 — S-191 Data Tapes Received	A3-1
Appendix 4 — S-192 Data Tapes.	A4-1
Appendix 5 — S-190 Data.	A5-1
Appendix 6	A6-1

I. SUMMARY

Final Report of the Skylab Investigation

Investigation Number: 556-1

Principal Investigator: Dr. Robert J. Curran
Goddard Space Flight Center
Meteorology Branch, Code 911
Greenbelt, Maryland 20771

Co-Investigators: Dr. Vincent V. Salomonson
Mr. William Shenk

A. Introduction

The laboratory conditions of the Skylab space vehicle provided a unique opportunity for the simultaneous observation of terrestrial phenomena with a variety of instrumentation. The presence of a trained observer on Skylab allowed for the selection of specific sites and specific combinations of sensors. These advantages are particularly useful in the observation of meteorological phenomena. Atmospheric processes are typically short lived, having mean lifetimes ranging from fractions of a second to hours. Very large scale phenomena such as Hurricanes or Baroclinic waves (Fronts) are longer lived and have lifetimes of from days to weeks.

This experiment (556-1) made use of the ability of astronauts, trained to locate specific meteorological phenomena, to direct instrumentation at meteorological targets of opportunity. The most apparent feature associated with these phenomena are clouds. Clouds are strongly correlated in physical structure with most types of meteorological phenomena in the lower atmosphere. Because they are readily observable without the need of instrumentation, cloud types could be indicated by an investigator and this information could be given to the astronaut for selecting targets toward which to direct instrumentation.

The initial direction in which the investigation proceeded is indicated in the statement of work which follows.

B. Statement of Work—Technical Approach

The objectives of this investigation are: (1) acquire a set of three dimensional cloud statistics most representative of global cloudiness; (2) to determine cloud top heights and cloud types; and (3) to identify cloud characteristics associated with significant weather activity.

The PI shall use S-190 to acquire photography of sea surface and cloud formations, and use S-191 and S-192 to acquire radiance data from cloud tops and the atmosphere. A portion of the experiment will be repeated over as many as nine different cloud situations, most of which will be over water. The nature of the weather patterns to be investigated requires test sites from the equator to mid latitudes.

Stereographic techniques shall be applied to contour cloud field. In addition to satisfying part of the objectives, this product will provide cloud truth for the S-191 and S-192. Processing the spectrometer and scanner data involves use of modified computer programs performing radiative transfer calculations (currently in use with TIROS and NIMBUS) to acquire the "inversion" or radiance profiles to temperature and moisture profiles and to correct for the attenuation effects of the atmosphere.

Anisotropic information shall be analyzed to identify cloud types using data from spectrometer which will scan a cloud through its entire capability from 45° forward to 10° back. Analysis of storm cloud tops and characteristics can reveal protrusions with significant thermal patterns which are related to severity of storm activity, including development of tornadoes. Where possible, comparisons between weather radar data and EREP measurements shall be made.

Aircraft data are desired concurrent with the EREP pass to acquire cloud types, height of bases and tops from surface to 60,000 feet.

Standard radiosonde data shall be used when appropriate.

Cloud motion data in some of the test sites can be acquired from a series of views processed from data from the geosynchronous weather satellite, ATS-3. Cloud motion is an important factor affecting accuracies of cloud height computations when the motions are large.

ORIGINAL PAGE IS
OF POOR QUALITY

This statement of work was agreed upon by the first principal investigator on this project, William E. Shenk. Historically, the actual tasks have been restructured several times reflecting the slightly different technical approach of the present principal investigator and the type and quality of data actually received. The structure of the investigation and its scheduling are described in the following paragraph.

The principal objectives of this investigation were: (1) To determine from the limited set of measured data, the parameters available describing cloud physical structure as inferred from cloud radiance; (2) to use this measured data to map the physical parameters specified, and (3) to compare the inferred parameters with measurements made by other means. These objectives are merely a refocusing of the objectives given in the statement of work. In particular cloud type is a difficult attribute to quantify and therefore a more direct analysis of several parameters describing cloud physical structure was adopted. The determination of cloud altitude was hampered by one major problem which limited analysis. The problem found in using the measured radiances from the infrared portion of the S-191 data was that the "off-band" leakage of radiation made data from this part of the spectrum essentially unuseable. This problem was recognized by the S-191 instrument scientist, Dr. Thomas Barnett, and given in a cautionary note from Dr. Barnett. This cautionary note is given in full detail in Appendix 1 of this report. The effect of the problem indicated in the cautionary note was: 1) to completely invalidate use of the $15 \mu\text{m}$ CO_2 radiances for determining atmospheric temperature structure; and 2) to invalidate use of any of the infrared radiances for scientific analysis. These problems were correctable for radiances in the visible and near infrared part of the electromagnetic spectrum. However, even at these latter wavelengths there is a question as to whether the correction was applied twice. Processing at GSFC assumed that the corrections given by JSC were not applied to the S-191 data tapes sent. This was certainly the case for the tapes sent prior to the cautionary note but is questionable after that time.

C. Instrumentation Used in the Investigation

As stated in the original statement of work three main sources were to supply data for the present investigation. These sources were:

- i) S-190 Multispectral Photographic Camera
- ii) S-191 Infrared Spectrometer
- iii) S-192 Multispectral Scanner

A brief description of this instrumentation and relevant parameters pertinent to this investigation are given in Table 1 of this report. Earth resources experiment

package sensor performance evaluation reports have been received concerning these sensors and will not be commented upon in this report except for the few cases in which they seriously impact the analysis.

Table 1: Instrumentation Which Provided Data for the Present Investigation

Instrument Designation	Description	Relevant Parameters
S-190	Multispectral photographic camera	Six cameras with matched optical systems photographing the same area on the ground 10.6° fore and aft of nadir. Viewing a 163×163 km square at approximately 70 meter resolution. Very high geometric stability.
S-191	Infrared spectrometer	Measures spectral radiance in the wavelength bands 0.39 to $2.5 \mu\text{m}$ and 5.82 to $15.99 \mu\text{m}$. Spectral resolution to wavelength ratio 2/100. Nadir spatial resolution approximately 0.5 km. Spectrometer is pointable but locked in the nadir mode for most data of relevance to present investigation. 16 mm movie camera boresighted to spectrometer.
S-192	Multispectral scanner	Measures spectral radiance in 13 different wavelength intervals. Conical scan, spatial resolution approximately 70 meters covering a swath 74 km wide.

D. Initial Processing of the Digital Data and Use of the Photographic Data

Data collected from the S-191 and S-192 radiometers were processed at JSC and deposited on computer compatible magnetic tapes. These tapes were shipped to GSFC for analysis. A major portion of the activity associated with this investigation centered on the programming necessary to read the magnetic

tapes and analyze the data contained. This programming was handled under a subcontract to the Computer Sciences Corporation, (CSC), Silver Spring, Maryland. Work started on this project in June 1973. However because of several difficulties in preprocessing of the data at JSC, hands on analysis of the S-192 data did not start until September 1974 and the S-191 data in February 1975. Final versions of the S-191 tapes were received in April 1974 and the S-192 tapes six months prior to that date. During the period of development of the read programs contract personnel were in close communication with JSC personnel producing the computer compatible tapes. Early development of the read programs allowed feedback of tape formatting errors found by CSC personnel to be given to the JSC tape generating facility. This process resulted in multiple copies of both S-191 and S-192 data tapes as the correct format evolved. Final forms were sent to other principal investigators at their request. Investigators requesting either copies of the read programs or information on how to read data tapes are included on the following list:

Mr. John Alishouse
NESS-NOAA
Suitland, Maryland

Dr. David Tingey
Boeing Aerospace Company
Seattle, Washington

Mr. Carl Grey
C. S. Draper Laboratories
Cambridge, Massachusetts

Dr. David Anding
ERIM
Ann Arbor, Michigan

A description of the programs generated for reading and analyzing S-191 and S-192 data is given in Appendix 2. Several programs listed in this appendix were developed during the period preceding the receipt of the data tapes. In several cases because of the low quality of the S-191 infrared data, these analysis programs were not used.

A list of the S-191 data tapes received for scientific analysis is given in Appendix 3. Noted in that appendix are the start and end times for data tapes and the JSC tape number. In every case, two tapes correspond to the same time interval. The reason for this apparent duplication is due to the separation of each spectrum into two parts which, in turn are separated onto two tapes.

A list of all S-192 data tapes received is given in Appendix 4. Here again several tapes appear to cover the same time interval. In the case of the S-192 data these tapes are roughly temporally contiguous but have wrong times indicated.

Photographic data from the S-190 facility were obtained with sixty percent overlap. This amount of overlap allowed successive frames to be used to determine cloud altitude from the parallax found in the pictures. Contour maps of cloud altitude were generated by the Defense Mapping Agency under contract to the present task. The could height determinations were made on an AS11A stereographic analyzer. Variations in altitude, attitude and earth curvature were easily removed from the data with the use of this instrument. Several constraints were placed on the data before contouring could proceed. Two primary constraints were that the photographic data must show enough relief that easily identifiable features may be found in the frame pairs. Secondly, a surface feature such as a shore line (or even cloud shadows on the surface) must be present in the pair in order to serve as a baseline. This latter constraint was relaxed only in cases where several adjacent pairs were contoured, one of which had a baseline.

The S-190 data which were contoured in the manner described above are listed in Appendix 5. The models (photographic pairs) were chosen to include all cases in which S-192 multispectral scanner data was available. Beyond this amount, as much of the S-190 data as overlapped the S-191 infrared spectrometer data received, satisfied the constraints mentioned, and appeared to be of scientific interest; was chosen to be contoured. Samples of these contoured data are included in this report.

II. TECHNICAL BACKGROUND AND RESULTS OF BASIC STUDIES

A. General Background

Terrestrial clouds are composed of water in either the solid or liquid thermodynamic state. The most important properties of both liquid water and ice for describing the interaction of particulates composed of these substances with electromagnetic radiation is the refractive index of the material. The refractive index is a complex quantity that is wavelength dependent and differs according to the phase for a given material. Values of the real and imaginary parts of the refractive index for both liquid water and ice have been collected by Irvine and Pollack (1) and by Hale and Querry (2). These values are displayed in Figure 1 for the range of wavelengths that is of interest to the present study.

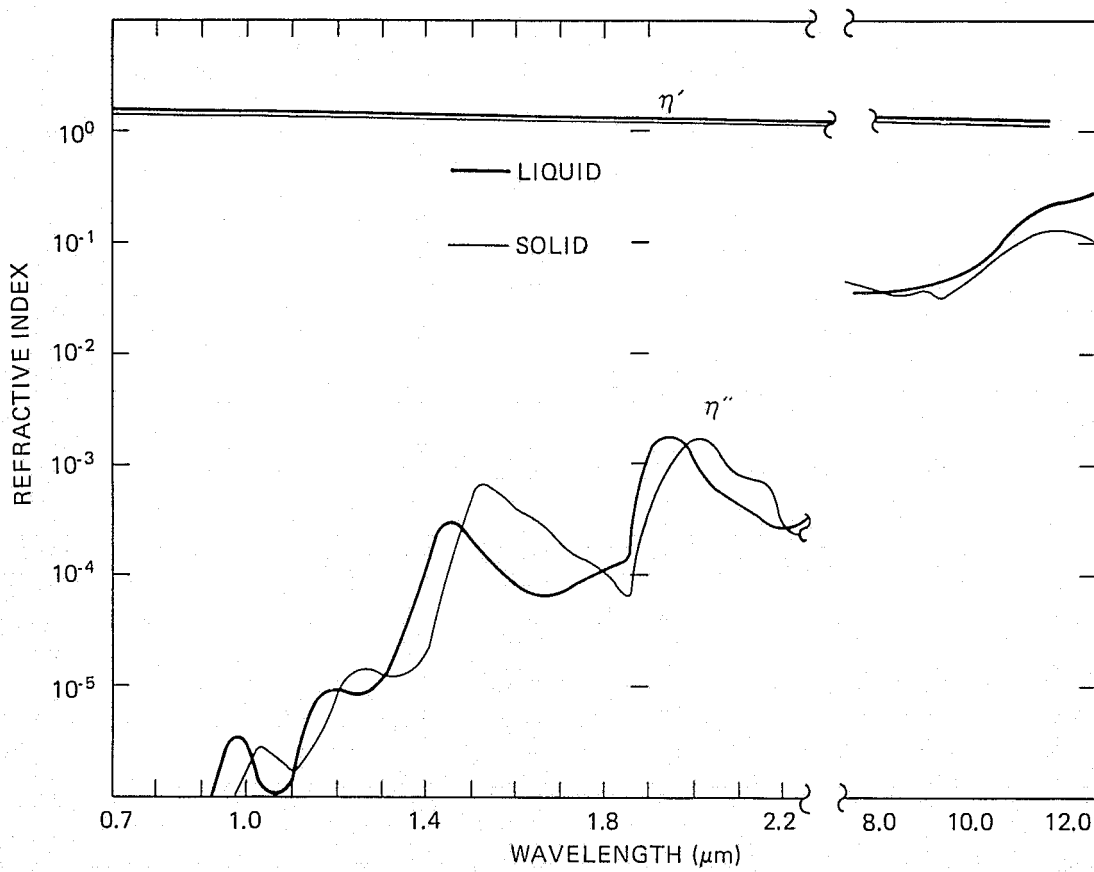


Figure 1: Refractive indices of ice and liquid water
(Irvine and Pollack (3), Hale and Querry (4)).

The real parts of the refractive indices of liquid water and ice differ only slightly from each other (Figure 1). However, large differences are evident between the imaginary parts of the refractive indices, for the two phases in the spectral region under consideration.

Although the manner in which the real and imaginary parts of the refractive index manifest themselves physically cannot be easily separated, it can be stated that, generally, the real part is strongly related to the scattering cross section of the particle and the imaginary part is strongly related to the absorption cross section of the particle. If the absorption effects of the imaginary part can be measured remotely, then it should be possible to determine the phase (liquid or solid) of the water that forms a particular cloud. If it is further assumed that the water particles are spherically symmetric in both phases, then the cross sections can be evaluated in a straightforward manner by the use of Mie theory.

In order to study the effects of scattering and absorption in the interaction of electromagnetic radiation with particulates, a useful quantity to consider is the ratio of the scattering cross section to the total cross section: the single-scattering albedo. Figure 2 shows the dependence of the single scattering albedo on wavelength for a cloud distribution of liquid water spheres. The cloud distribution employed for this figure was a modified gamma distribution, as discussed by Deirmendjian (4); \bar{r} is the mean radius (the mean here is the r^2 weighted mean). Each member of the family of curves shown in the figure corresponds to a different value of \bar{r} . In general, it may be noted that the single scattering albedo decreases as \bar{r} is increased. Figure 3 shows a similar family of curves for a distribution of ice spheres. A comparison of Figures 2 and 3 reveals that the wavelength dependence of the single scattering albedo is different for the two different phases of water. Naturally occurring ice particles are known to be non-spherical. However, present theory is not complete as to either the shapes anticipated in nature or the complete scattering and absorption properties of these crystals. Work is in progress by several workers (5, 6, 7, 8). Where possible, these results will be used in the analysis of the measured data collected in the present experiment.

Analyses of single-scattering calculations for distributions of both liquid-water and ice spheres indicate the strong dependence of the single scattering albedo on the size distribution of the spheres for both phases of water. In addition, thermodynamic phase determinations can be made in many wavelengths between 1 and $1.5 \mu\text{m}$ because of the large differences between the imaginary parts of the refractive indices of the two phases. Therefore, a knowledge of the wavelength dependence of the single scattering albedo for a cloud viewed in this spectral interval could be used in a determination of the physical properties of that cloud. The remote sensing of cloud radiances, however, detects not only single scattered radiation but the higher orders of scattering as well.

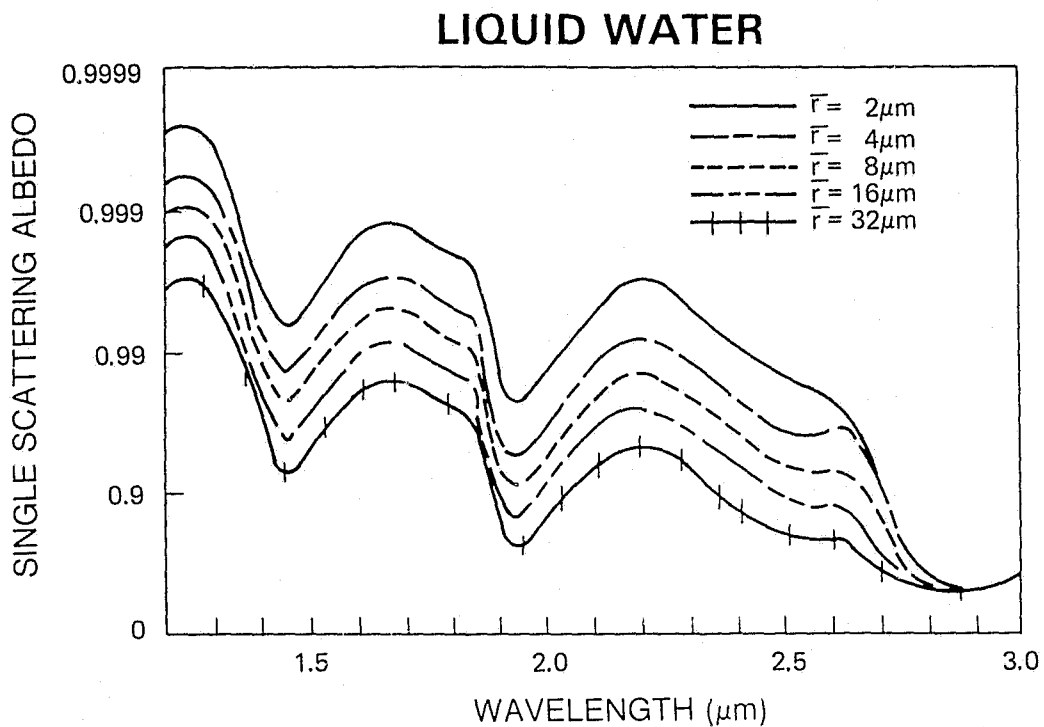


Figure 2: Single scattering albedo as a function of wavelength and particle size for spherical polydispersions having mean radii (\bar{r}) as shown. Refractive indices used were those of liquid water (Hansen and Pollack (5)).

In the radiative transfer process, the single scattering albedo plays an important role. Whenever a photon is incident upon a cloud particle, it will either be absorbed or scattered; the relative probability of the photon being scattered is the albedo for single scatter. Multiple scattering calculations show that the bidirectional reflectance of a cloud can be related by generalized expressions to the optical thickness of the cloud, the size distribution of particles composing the cloud, and the single scattering albedo. For wavelengths at which the atmospheric molecules are absorbing, the single scattering albedo and cloud optical thickness must be modified. A sample graph of the relationship between optical thickness, single scattering albedo and cloud reflectance is shown in Figure 4.

B. Radiometric Techniques

The optical thickness of a cloud is equal to the natural logarithm of its direct transmission. To determine the optical thickness of the cloud, we choose a wavelength at which the molecular absorption and scattering of the atmosphere are

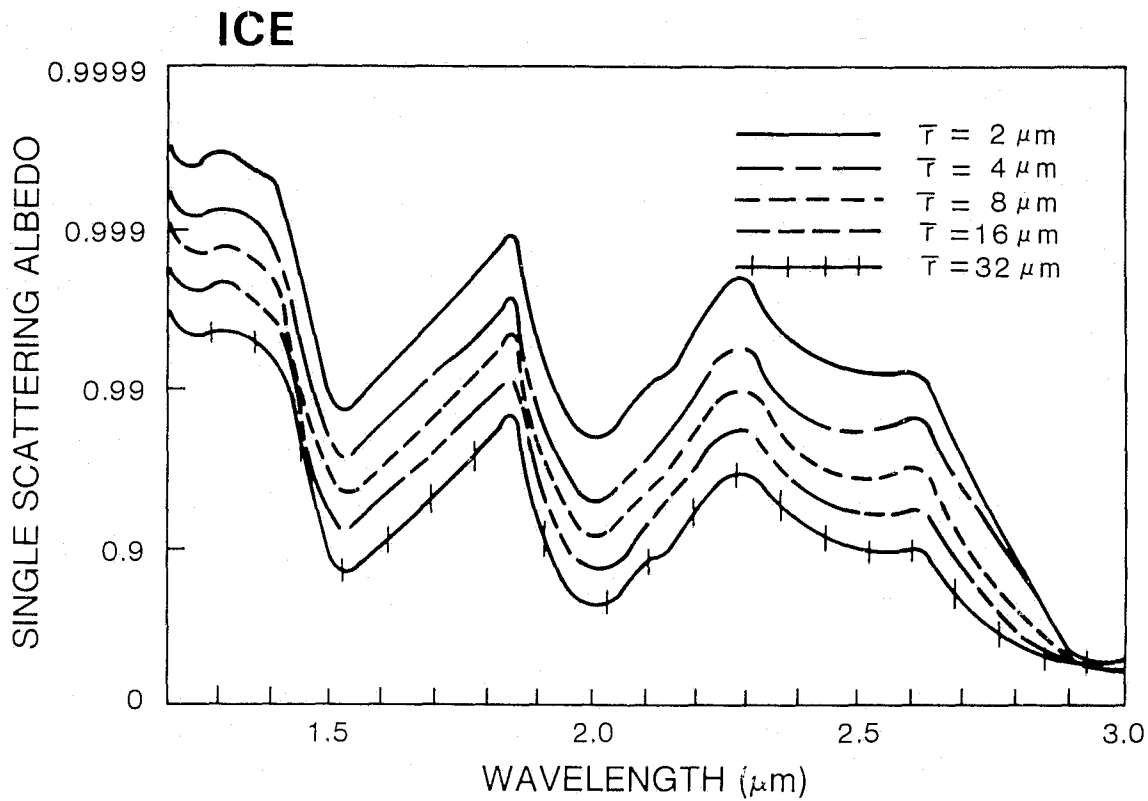


Figure 3: Single scattering albedo as a function of wavelength and particle size for a spherical polydispersion having mean radii (\bar{r}) indicated. Refractive indices used were those of ice (Hansen and Pollack).

negligible compared with the attenuation properties of the cloud alone. For the present study, this reference wavelength is $0.754 \mu\text{m}$. The optical thickness is a fundamental radiation parameter which is important in determining transmitted and reflected fluxes from a cloud. Thus, optical thickness is of first order importance in determining the energy budget of the atmosphere.

Because the imaginary refractive index for both ice and liquid water is less than 10^{-6} at $0.754 \mu\text{m}$ wavelength, the single scatter albedo for particles composed of these two phases of water is very close to unity. Furthermore, the small imaginary refractive index implies that the dependence of the single

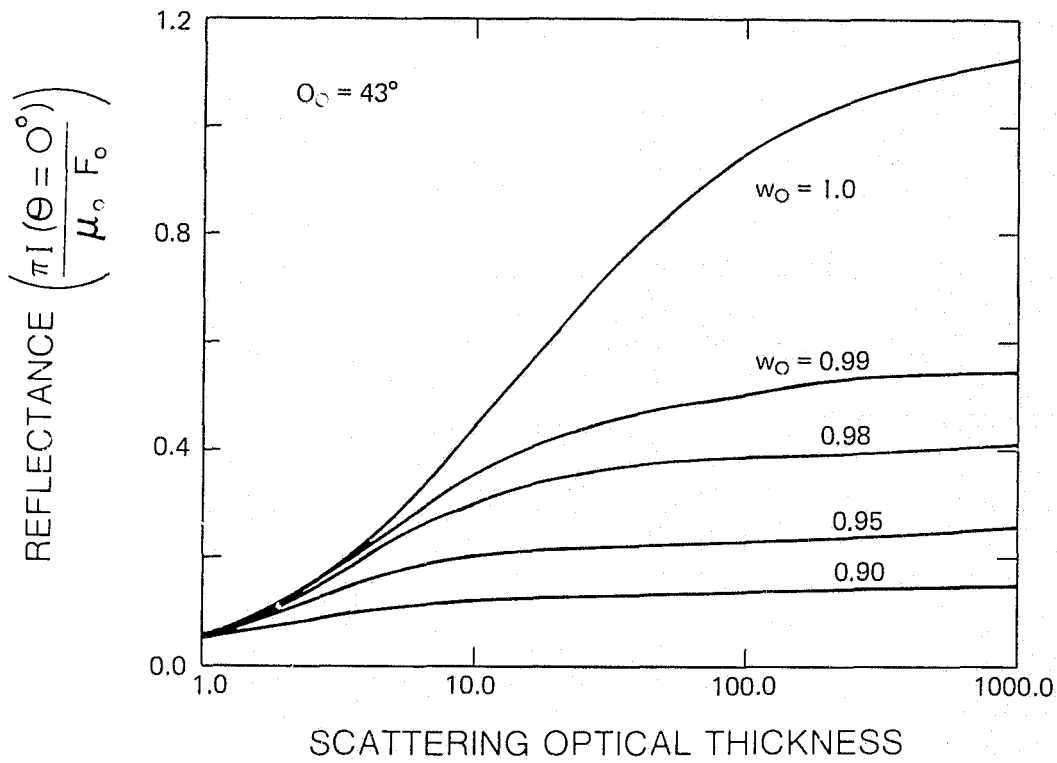


Figure 4: Cloud bidirectional reflectance as a function of optical thickness for several differing single scattering albedos, ω_0 . Wavelength for these calculations is $0.074 \mu\text{m}$ and the particle size distribution was typical of fair weather cumulus.

scattering albedo on particle size is negligible. Measurements of bidirectional reflectance at $0.754 \mu\text{m}$ may therefore be directly related to the optical thickness of the cloud at that wavelength by using a theoretically derived relationship such as that shown in Figure 4 for $\omega_0 = 1$. The effects of particle size distribution changing the angular scattering of radiation and thus changing the multiply scattered radiance has been shown to be small by Kyle (9) for commonly assumed cloud particle size distributions.

One measurement difficulty in determining cloud optical thickness is due to clouds of small horizontal spatial extent not filling the instrumental field of view. This problem has been considered by Cox and McKee (10) and by Davies (11) and is being studied in more detail by Thomas under NASA Contract NAS5-20857 in support of the presently proposed effort.

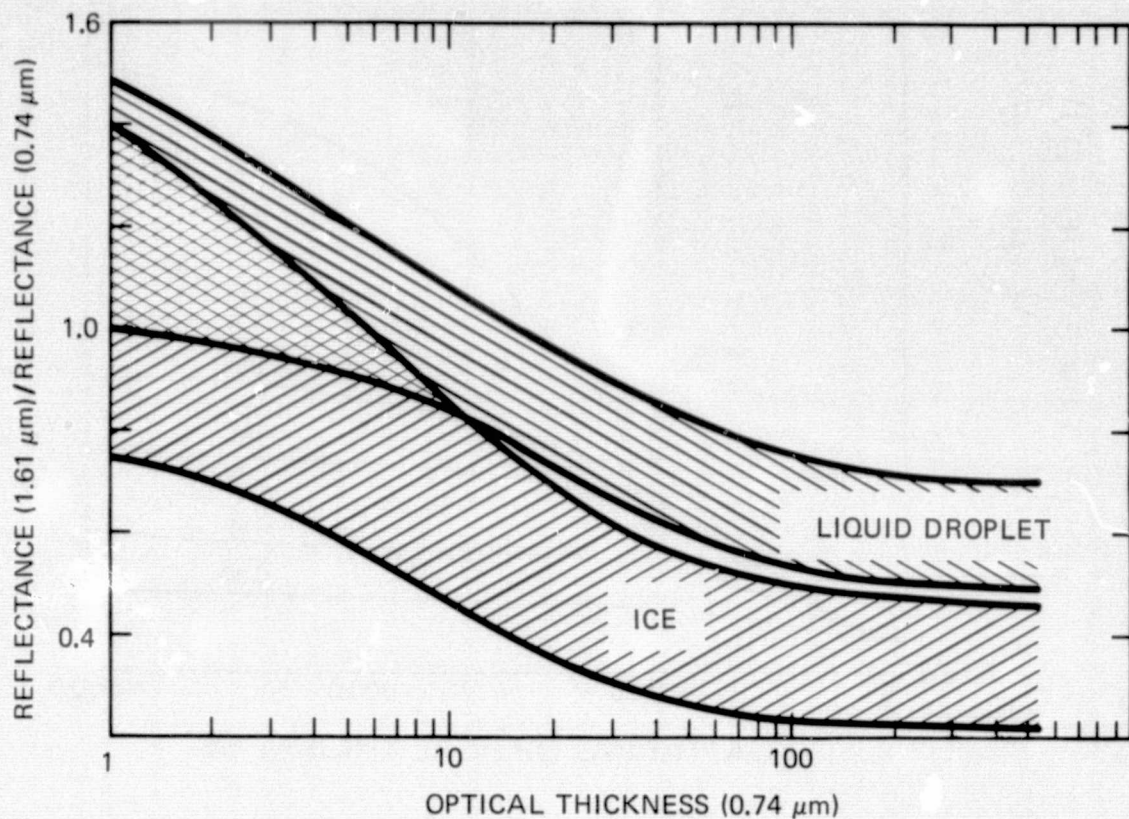


Figure 5: Ratio of cloud reflectance at $1.61 \mu\text{m}$ to that at $0.754 \mu\text{m}$ as a function of cloud optical thickness at the latter wavelength. The bands are formed by two extremes in particle size distribution with a small particle distribution ($\bar{r} = 4.5 \mu\text{m}$) forming the upper bound and a large particle distribution ($\bar{r} = 16.2 \mu\text{m}$) forming the lower bound.

Passive determination of particle phase and size make use of comparisons of bidirectional reflectances at wavelengths where the imaginary refractive index is appreciable. At the wavelength $1.61 \mu\text{m}$ the imaginary refractive index of ice is 3.8×10^{-4} and that of liquid water is 8.55×10^{-5} . Thus, particles of a given size have a smaller single scattering albedo for ice than they do for liquid water at this wavelength. A suitable measure for determining thermodynamic phase is the ratio of the cloud reflectance at $1.61 \mu\text{m}$ to that at $0.754 \mu\text{m}$. Figure 5 shows the relationship between the ratioed reflectances and the optical thickness at the reference wavelength. The bands in Figure 5 are formed by two extremes in particle size distribution. It may be noted in Figure 5 that multiple scattering

of the radiation enhances the small difference in single scatter albedo as evidenced by the separation in phases for optical thicknesses larger than approximately 10.

The technique for phase determination has been applied to data acquired by the S-192, multi-spectral scanner on Skylab. Using the appropriate channels, the optical thickness were determined and subsequently, the thermodynamic phase as shown in Figure 6. The accuracy of the determination of the parameter τ (0.754) is unknown because of the virtual impossibility of directly measuring such a parameter. However, in the present figure, the optical thickness is used as an internal parameter as outlined above. An indicator of the correctness of the phase determination is the $11 \mu\text{m}$ brightness temperature. The frequency histograms in Figure 6 indicate an ice cloud with a mean particle temperature of 238°K and a liquid water cloud at 270°K .

In a manner similar to the phase determination one may determine a parameter indicating particle size. However, to determine this parameter, a new wavelength is chosen such that a larger imaginary refractive index makes the cloud reflectance more strongly dependent on particle size. At $2.125 \mu\text{m}$, the imaginary refractive indices for ice and water are 7.56×10^{-4} and 3.9×10^{-4} , respectively. The two imaginary refractive indices are not different enough to be useful for phase differentiation. Figure 7 shows the effect of particle size on reflectance ratio as a function of cloud optical thickness. Using these theoretically derived curves, experimental data can be analyzed to determine particle size.

The $2.06 \mu\text{m}$ and $2.13 \mu\text{m}$ channels are multi-purpose. The transmittances can be combined with the A band transmittances to yield a correction for cloud penetration. By comparing Figures 8 and 9, it is seen that not only are the absolute magnitudes of the transmittances on the spectral intervals different, but also the slopes of the two transmission curves are different. Therefore, it should be possible to use the $2.0 \mu\text{m}$ transmittance as a correction for cloud penetration.

Preliminary results from Skylab indicate that it should be possible to delineate between snow and clouds by utilizing the $2.13 \mu\text{m}$ and $0.754 \mu\text{m}$ channels. Ratios for snow, cirrus and coastal stratus are shown below; where

$$\begin{aligned}\text{Ratio} &= R(2.125) / R(0.754) \\ &= [I(2.125) / I(0.754)] \times [F_0(0.754) / F_0(2.125)]\end{aligned}$$

<u>Scene</u>	<u>Ratio</u>
Coastal Stratus	0.545 ± 0.04
Cirrus	0.45 (range unknown)
Snow	0.089 ± 0.035

THERMODYNAMIC PHASE DETERMINATION USING SKYLAB S192 DATA

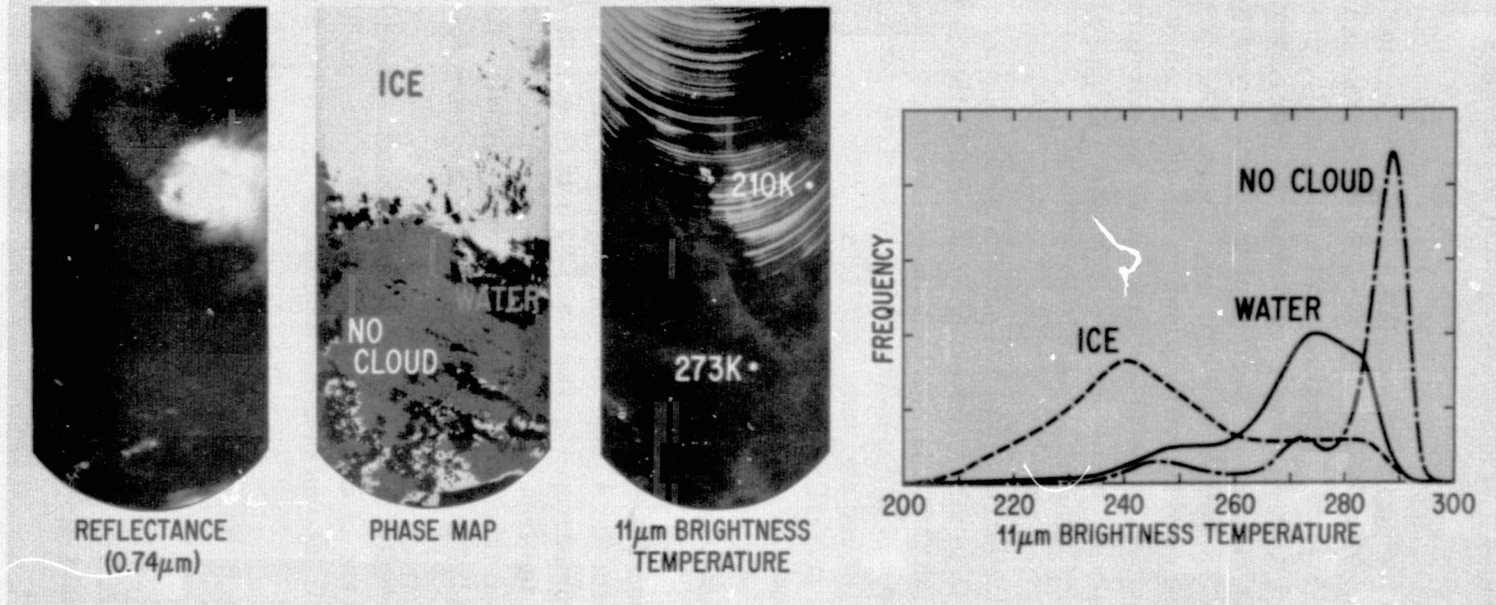
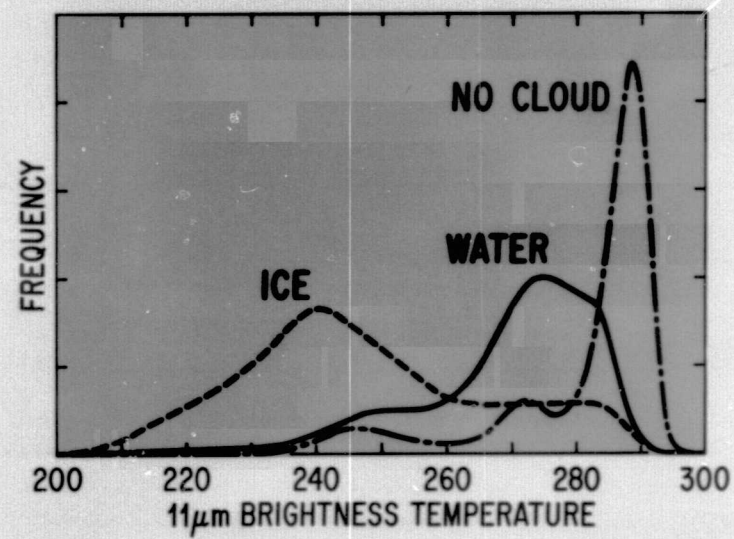
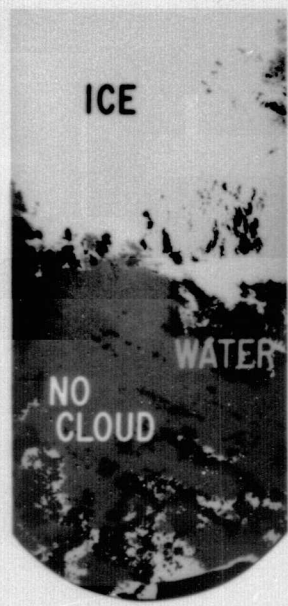
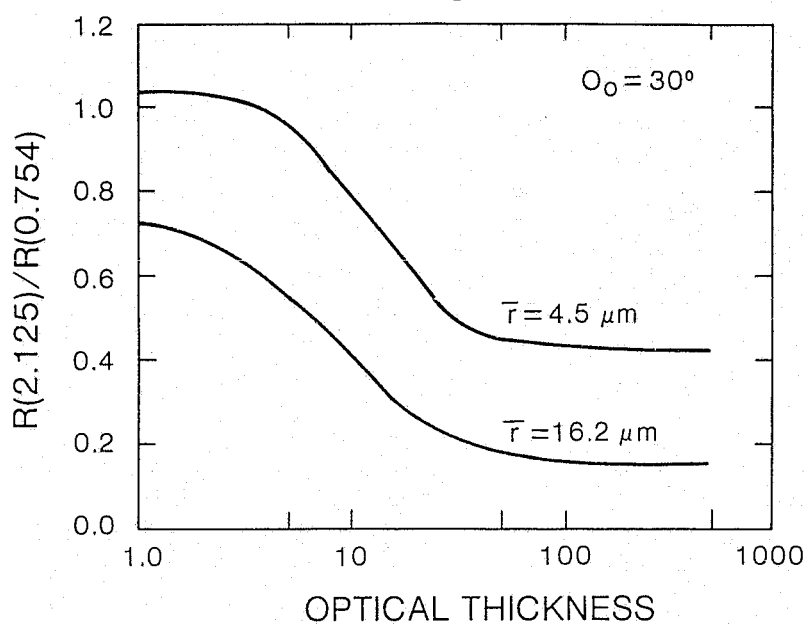


Figure 6: Sample of phase determination from Skylab S-192 data.
Graphs on right give frequency distribution of 11 μm brightness temperature for each phase.

THERMODYNAMIC PHASE DETERMINATION USING SKYLAB S192 DATA

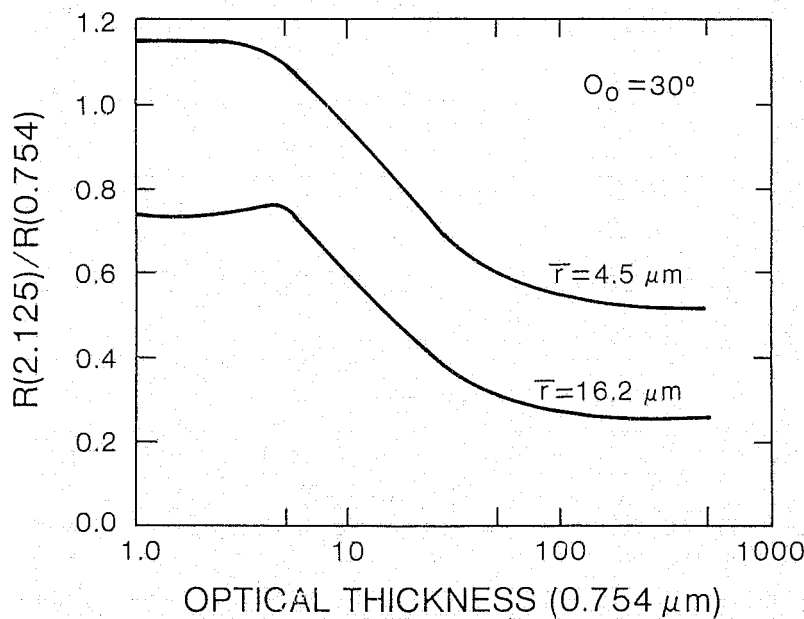


ICE



OPTICAL THICKNESS

LIQUID WATER



OPTICAL THICKNESS (0.754 μm)

Figure 7: Reflectance ratio of $2.125 \mu\text{m}$ to $0.754 \mu\text{m}$ as a function of optical thickness for two different size distributions.

The reason for the large standard deviations for the snow data is the extremely small value of the $2.125 \mu\text{m}$ signal.

In all of the preceding analyses, it was assumed that the clouds were composed of spherical particles. In practice the ice crystals that form naturally occurring cirrus clouds are quite non-spherical and usually are hexagonal needles hundreds of micrometers in length and several tens of micrometers in diameter (Heymsfield and Knollenberg (12) and Ono (13)). The comparisons be-

III. RESULTS OF USE OF THE SKYLAB DATA AND ITS COMPARISON WITH THEORY

A. Cloud Altitude from 11 μm Radiometry

The initial task which was addressed using the Skylab data was the comparison of altitude determinations using the 11 μm brightness temperature with the more accurate altitude determinations found by altitude contouring the S-190 photographic data. The process to be used in determining cloud altitude from 11 μm radiance has been discussed by several authors including Shenk and Curran (14). Optically thick clouds, in thermodynamic equilibrium with their surroundings, emit radiation according to their temperature. The radiation measured at satellite altitude then is related to the temperature of the cloud top by the inverse Planck function. For clouds that are not optically thick, the radiation detected at cloud top is partially due to the cloud emission and partially due to the surface radiation transmitted through the cloud. The relative contributions of these two radiation sources is dependent upon the optical thickness of the cloud.

The determination of cloud altitude uses an externally determined atmospheric temperature versus altitude profile to relate the 11 μm brightness temperature of the cloud to the altitude of the cloud top. The present investigation was to use the S-191 infrared radiometer to provide 15 μm CO_2 radiances from which the atmospheric temperature versus altitude profile could be obtained. As mentioned in the previous section, the data collected for the 6-15 μm spectral region using the S-191 infrared spectral radiometer, was not of sufficient quality for use in this study. With this lack of information detailed comparisons of the cloud heights obtained from the two methods was impossible.

Under normal conditions the lapse rate, change of temperature with altitude, is approximately $7^\circ\text{C}/\text{km}$. The multispectral scanner, S-192, contained an 11 μm spectral channel from which brightness temperature of clouds could be calculated. These brightness temperatures were grouped into intervals of 7°C , which should correspond to approximately one kilometer intervals. Maps of these brightness temperatures for all S-192 data received, are included in Appendix 6 of this report. Also included in that appendix are the contoured altitudes of the clouds as obtained from the S-190 data. Comparison of the two sources of data is difficult by any other means than detailed point by point comparisons.

B. Determination of Thermodynamic Phase

As indicated in section II, refractive indices in the near infrared are strongly dependent on the thermodynamic phase of the H_2O forming the clouds. The process outlined in section II for determining thermodynamic phase was applied to the Skylab data. The S-192 multispectral scanner had channels in the near infrared, suitable for the determination of thermodynamic phase. Maps of thermodynamic phase, using the process mentioned are included in Appendix 6. Each set of data included in that appendix shows reflectance, thermodynamic phase, $11 \mu m$ brightness temperatures and contoured altitudes. Comparisons of the data sources indicates the reasonability of the phase determinations. Unfortunately, corroborative *in situ* data was not taken. This data is the only source which can conclusively validate the radiometric determination.

An example of some of the reflectances found in the near infrared, several scenes have been chosen as representative. Figure 8 shows a scene observed by the S-192 multispectral scanner. Three parts of the scene have been identified for detailed study. The spectral channels used in the identification of thermodynamic phase are $1.65 \mu m$ and $0.74 \mu m$. Because it was found that the $0.74 \mu m$ channel saturated before reaching the large brightness values found in naturally occurring clouds, it was necessary to choose a second channel with similar optical properties and free of the saturation problem. The alternate channel chosen was centered at $0.83 \mu m$. Clouds are expected to have no wavelength dependent properties in this region of the spectrum other than that due to molecular absorption of H_2O vapor or O_2 .

Thus, the channels chosen to exhibit the phase behavior of clouds were channels numbered SDO 9 and SDO 11 corresponding to $0.83 \mu m$ and $1.65 \mu m$ respectively. Figure 9 is a scatter diagram of the ratio cloud reflectances in channels 11 and 9 versus the channel 9 reflectance. The faint line drawn in this figure is the discriminator line separating the two phases and corresponds to the region separating the phases in Figure 5. The surprising feature in Figure 9 is the fact that the majority of pixel elements lie in a region of the graph which is considered indicative of liquid water droplets. As is shown in Appendix 6 this cloud mass is at an altitude of 10 km and a temperature of approximately $240^\circ K$. This temperature, although not corrected for emissivity properties of the cloud at $11 \mu m$, is close to the temperature where pure water spontaneously changes into ice.

Several factors are included in determining the reflectances plotted in Figure 9. The two most suspect are the relative calibration of the channels and the relative values of the solar constant. The calibrations are difficult to determine (from the volume of material available concerning the performance

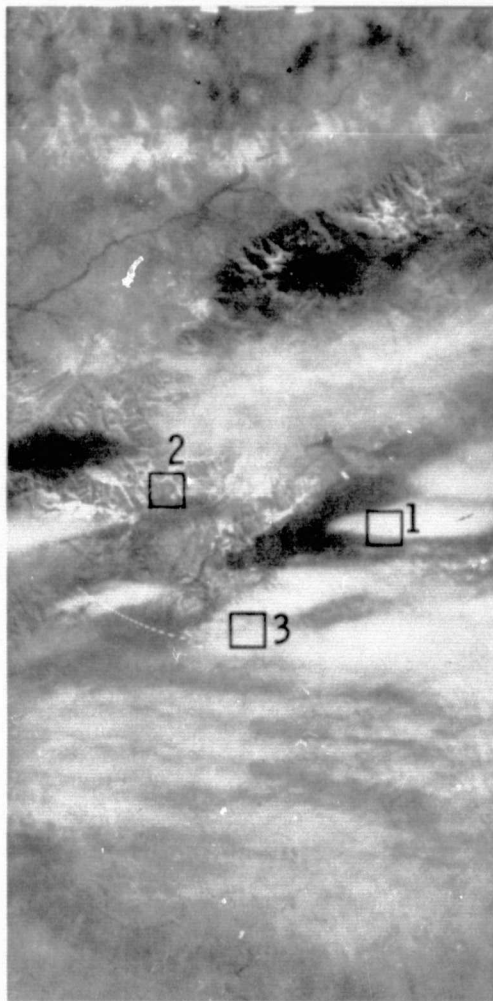


Figure 8: S-192 channel 9 reflectance, Day 335. Identified are 3 subsets of the scene in which radiance data was analyzed. More information about this scene may be found in Appendix 6.

of the instrument), but probably range from 5 to 10 percent relative value. The expected error in solar constant also is in the same range. The reflectances shown in Figure 9 can thus be moved a sufficient amount to place them in the ice region. However, it appears that the brighter portions of the cloud (where the channel 9 reflectances are greater than 0.7) would still remain in the liquid phase portion of the diagram.

The portion of cloud represented by the data in Figure 9 is expected to be of the same phase. This homogeneity of phase is expected because the large

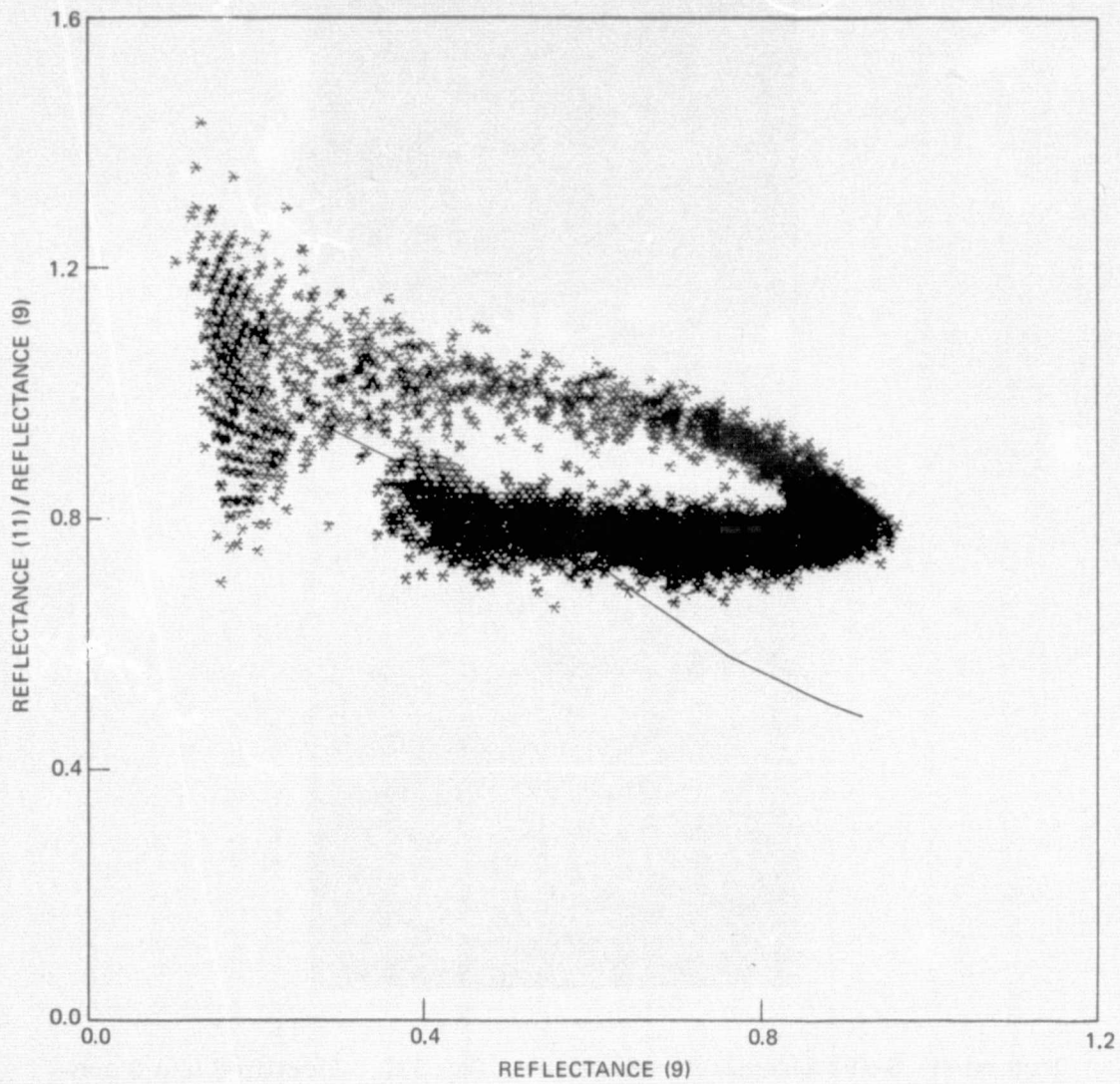


Figure 9

energy exchanges needed for the phase change in the cloud would cause a visible discontinuity in the structure of the cloud. Based on this argument it appears that values depicted in Figure 9 are not far from what is expected. This result implies either the calibrations and solar irradiances are near correct or, at least, are compensating. An interesting sidelight to this discussion is that the radiances found are directly comparable with calculations made assuming no other absorbers than due to the laboratory derived refractive indices of water or ice particles. This result is in contrast to discussion of absorption many times measured for clouds.

A portion of scene designated as subset number 2 contains a series of snow fields situated in mountain passes. This scene was chosen to be free from cloud contamination effects. A scatter diagram of the reflectance values from this portion of the scene is shown in Figure 10. The largest reflectance values for channel 9 are certainly due to snow. The smaller values of channel 9 reflectance are due to older or thinner snow or pixel elements only partially filled with snow. As is evident in Figure 10, the snow reflectance ratio is approximately 0.2. This ratio is appreciably smaller than the band of values expected

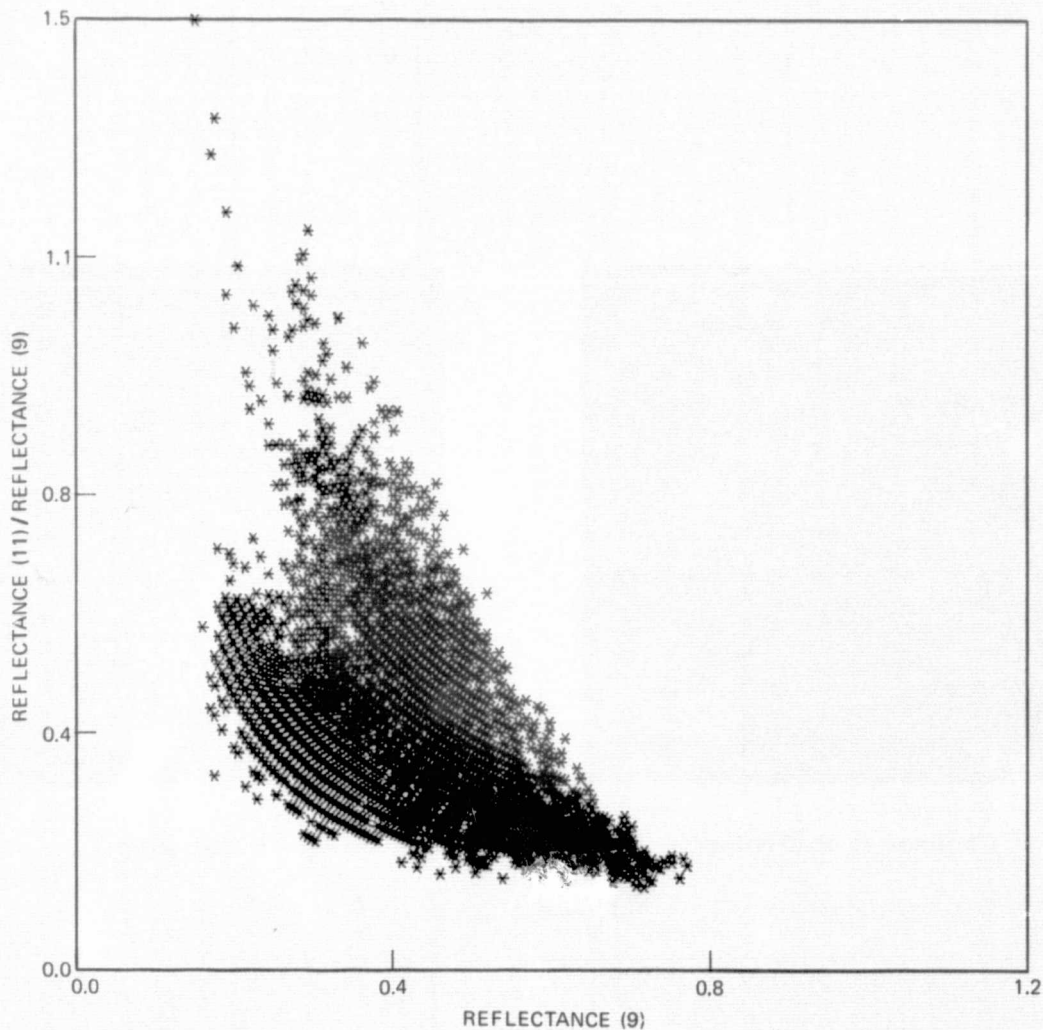
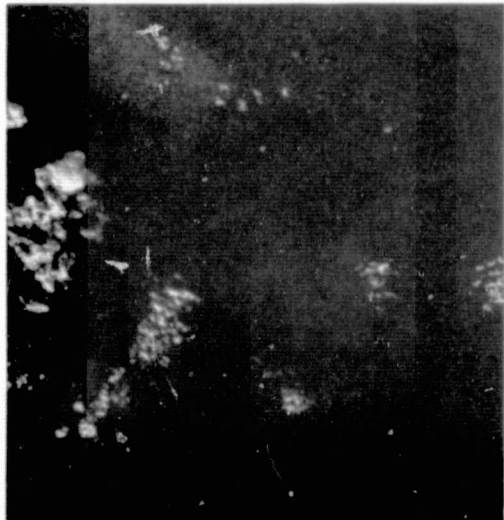


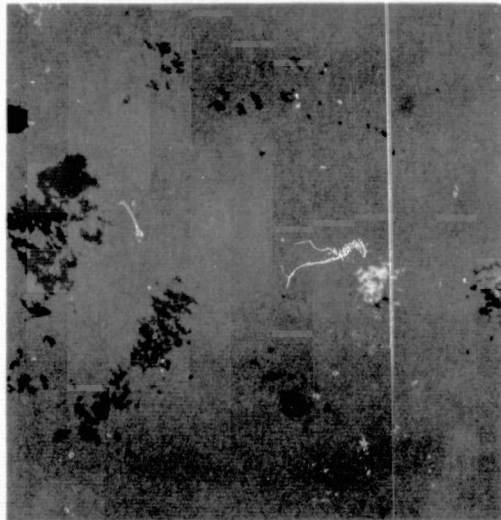
Figure 10: Reflectance ratio between channels 11 and 9 versus channel 9 reflectance. This portion of the scene includes several large snow fields with no clouds.

for an ice cloud as shown in Figure 5. However, the snow particles, which are much larger than ice cloud particles are in a portion of the phase diagram where abnormally large ice particles would be found. This result may be surprising because the calculations for multiple scattering of the radiation are made with the assumption that the scattering particles are separated by more than a few wavelengths and distances between particles is random. These two conditions appear to not be met for snow surfaces.

A scene containing clouds identified as being composed of water droplets over an ocean surface is shown in Figure 11.



Channel 11 Reflectance



Phase Map

Figure 11: S-192, channel 11 reflectance for Day 336. These clouds are low altitude cumuli as indicated in Appendix 6.

A scatter diagram of the reflectances found in the previous figure are shown in Figure 12. All pixel elements with channel 9 reflectances larger than 0.3 are identified as liquid water droplets. These data are consistent with the remarks made in the previous scene.

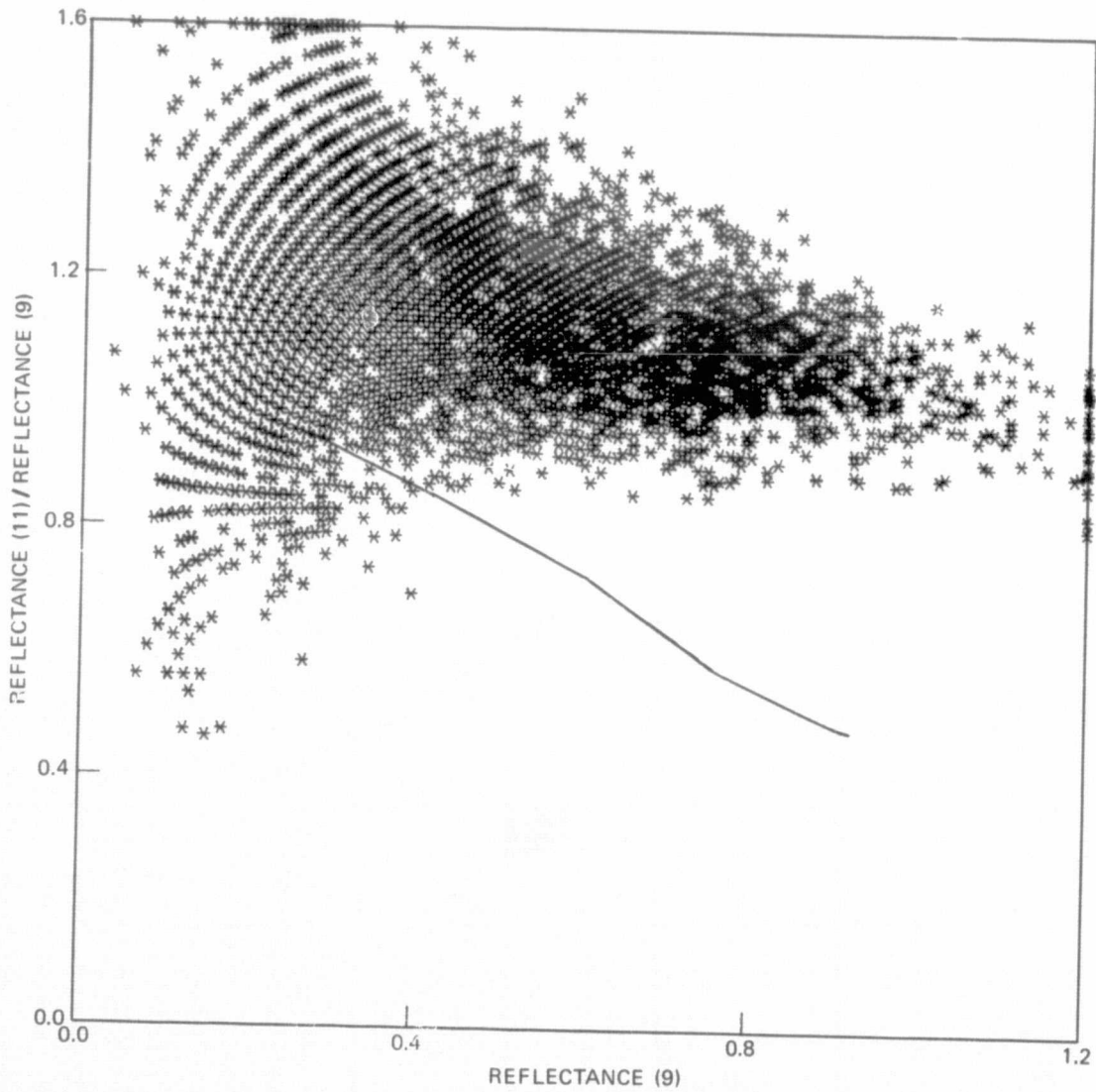


Figure 12

An example of ice cloud reflectance ratios is given in Figure 13. The data for this scatter diagram were taken from the large ice cloud found on Day 255 (see Appendix 6 for analysis of this data). The portion of the cloud chosen for presentation in Figure 13 was quite uniform. The uniformity caused the many points to be clustered very close to one another. The data given in Figure 13 may be found to lie close to the large particle boundary of the ice band of Figure 5. Thus the effective radius is slightly less than 16 μm radius.

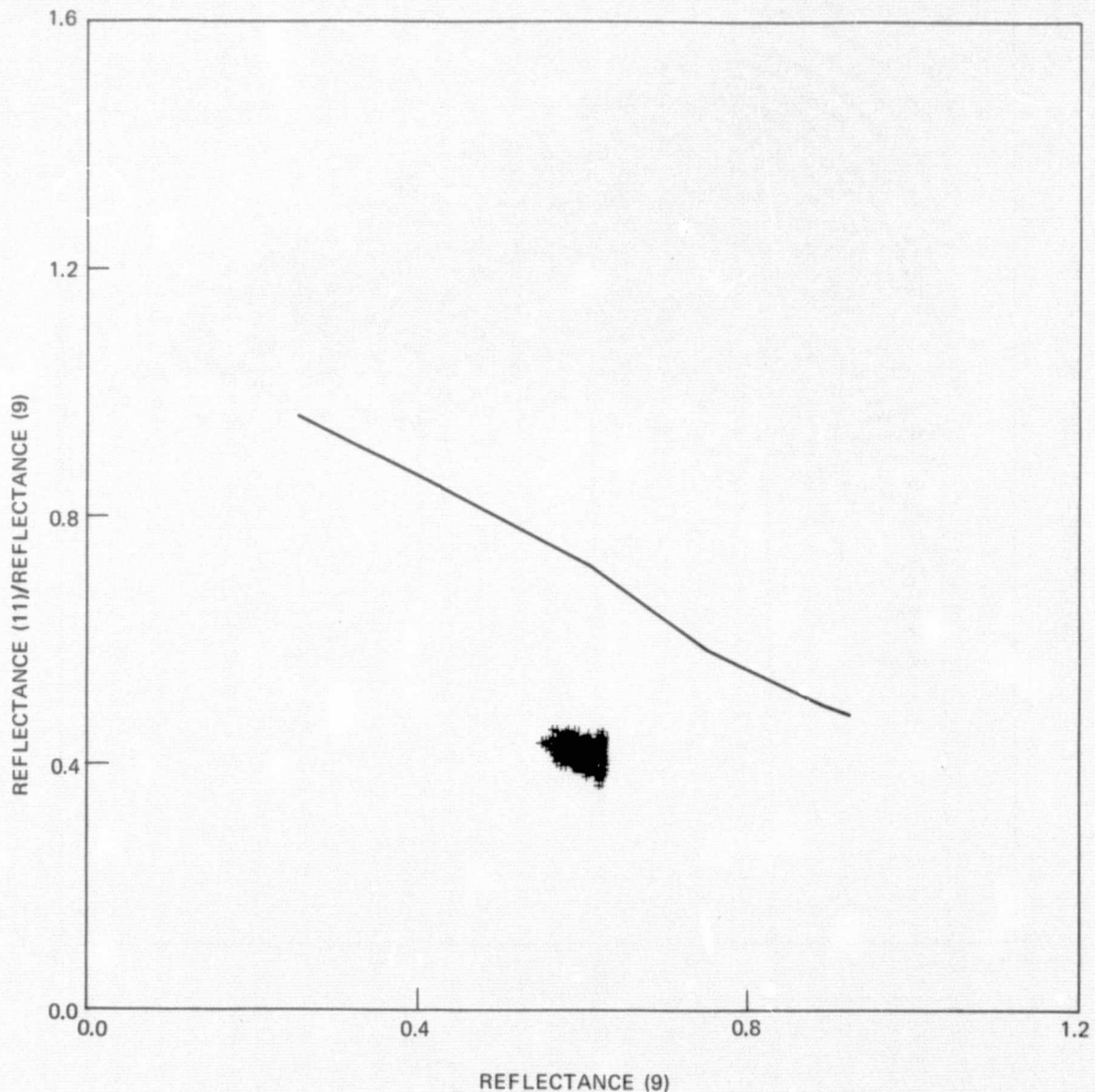


Figure 13

An example of ice cloud reflectance ratios is given in Figure 13. The data for this scatter diagram were taken from the large ice cloud found on Day 255 (see Appendix 6 for analysis of this data). The portion of the cloud chosen for presentation in Figure 13 was quite uniform. The uniformity caused the many points to be clustered very close to one another. The data given in Figure 13 may be found to lie close to the large particle boundary of the ice band of Figure 5. Thus the effective radius is slightly less than 16 μm radius.

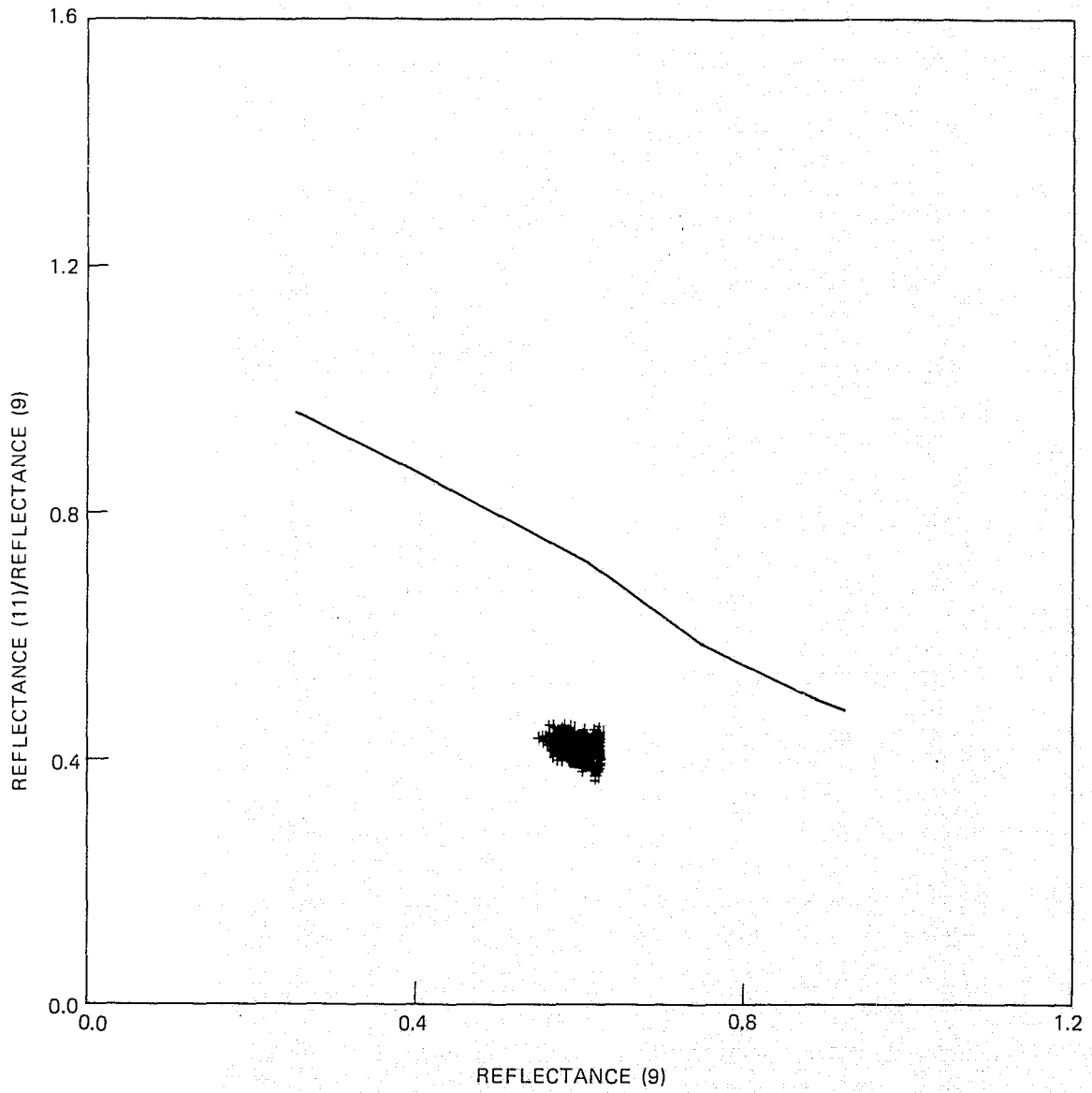


Figure 13

IV. CONCLUSIONS

As is the case with many experiments the results derived do not measure up to the results anticipated before the experiment. In the present case the major shortcoming of the data was the loss of the infrared radiances from the S-191 spectrometer. This was a key part of the present experiment because it allowed comparison of radiometrically derived cloud heights with the more accurate stereographic cloud height determination. However, the investigation was restructured with a new set of tasks replacing the original set. In many cases the new tasks were an attempt, for the first time, to compare theoretical calculations with satellite cloud radiance measurements. In this respect the investigation was a success and resulted in several interesting findings.

The cloud thermodynamic phase determination procedure was derived and tested with the data collected by the S-192 multispectral scanner. This scanner is the first NASA satellite to contain the spectral intervals necessary in applying the procedure. The results of the test indicate a large fraction of the data could be classified thermodynamically. An added bonus was the inclusion of snow in the classification approach. The conclusion to be drawn from this portion of the effort is that in most cases considered ice clouds, liquid water droplet clouds and snow fields can be spectroscopically separated to a high degree of accuracy.

The largest single element missing from the present investigation was the lack of supporting cloud truth information. This data was missing because of the change in the structure of the investigation after it was found that the cloud height task was not possible. The cloud height task had sufficient cloud truth from the combination of stereographic contouring of the S-190 data and aircraft underflights. The new set of tasks were centered in the area of cloud physics and no corroborative in situ data of this type was taken. Although many elaborate satellite radiometric instruments were used in the investigation, the lack of cloud truth data to validate the results severely weakened the conclusions to be drawn from the results.

The data analysis techniques applied to the Skylab data were useful in forming the data analysis system to be used on aircraft flights commencing in CY 1976. The instrumentation to be used for these aircraft flights was designed partly as a result of the present Skylab investigation. The S-192 spectral intervals which were found to be most useful in observing cloud characteristics were included in the design of the Cloud Physics Radiometer, the aircraft instrument. Thus, an additional conclusion would be that the experience gained in working with the Skylab EREP data was a useful step in the design of instrumentation and data handling procedures to be used on future aircraft missions and satellite missions. The present direction of effort is toward the laboratory experiments of the Space Shuttle. The Skylab, then, is logically connected to the Shuttle Spacelab through investigations similar to the present investigation.

REFERENCES

1. Irvine, W. M., and J. B. Pollack, *Icarus*, 8, 324, (1968).
2. Hale, G. M., and M. R. Querry, *Appl. Opt.*, 12.
3. Hansen, J. E. and J. B. Pollack, *J. Atmos. Sci.*, 27, 265-281 (1970).
4. Deirmendjian, D., Electromagnetic Scattering on Spherical Polydispersions, Elsevier Publishing Co., New York (1969).
5. Holland, A. C., and G. Gagne, *Appl. Opt.*, 9, 1113-1121 (1970).
6. Liou, K. N., *Appl. Opt.*, 11, 667-674 (1972).
7. Jacobowitz, H. J., *Quant. Spectrosc. Radiat. Transfer*, 11, 691-695 (1971).
8. Slutsker, A. I. and V. A. Marikhin, *Optics and Spectroscopy*, 8, 116-119 (1960).
9. Kyle, H. L. and R. J. Curran, "Cloud Top Altitude Measurements using Albedos near 13100 cm^{-1} ," AMS, Second Conference on Radiation, Arlington, Va., October 29-31, 1975.
10. McKee, T. and S. K. Cox, *J. Atmos. Sci.*, 31, 1885-1892 (1974).
11. Davies, R., "Three Dimensional Transfer of Solar Radiation in Terrestrial Clouds," AMS, Second Conference on Radiation, Arlington, Va., October 29-31, 1975.
12. Heymsfield, A. J. and R. G. Knollenberg, *J. Atmos. Sci.*, 29, 1358-1366 (1972).
13. Ono, A., *J. Atmos. Sci.*, 26, 138-147 (1969).
14. Shenk, W. E. and R. J. Curran, *J. Appl. Met.*, 12, 1213-1216 (1973).

APPENDIX 1

S-191

Cautionary Note sent with cover letter TF6-74-7-19 dated July 23, 1974

S191

Cautionary Note for Data
Processed According to
PHO TR 524 CH 2

July 3, 1974

ORIGINAL PAGE IS
OF POOR QUALITY

Enclosure

A1-2

The following anomalies remain in the S191 products being sent to users. Final resolution of all the anomalies and refinement of the software before reprocessing would cause unwarranted delays for most users. Thus, the anomalies are discussed so that the user may evaluate their effect on his data, and where appropriate, recommendations are made on how the user may correct his own data if necessary.

1: Spurious effects in raw data tabs (S042-5) or tapes (S041-2).

Look for jumps of greater than ten counts in wavelength ramp channel A4. This is pathological. Times in the vicinity of the gap are incorrect, viewed at the sub-second level, but detector voltages correlate properly against the wavelength ramp voltage. To produce the error, a frame of detector and wavelength data was dropped and time was stretched to fill the gap. The stretching will affect no more than six frames (one record). Request rerun of very short time segment including that scan if it is critical. The raw data processor is scheduled to be revised in mid to late July to eliminate this rarely occurring error.

2: Saturation of the A3 short wavelength channel is marked by an abrupt transition from radiance values .XXXE-02 to .XXXE-11 (due to having entered responsivities of 10^{10} for saturated values). Where this occurs, channel A5 takes over. Use the A3 radiances until this occurs, then the A5 radiances until A3 desaturates. Don't trust the last A3 value before saturation or the first value after desaturation; use A5. Channel A5 should never saturate; but in such a case A2 would take over.

3: Change of PHO TR524 document.

Change 2 to Rev. A is coming out soon. (Draft review copies will be available July 17, 1974) All data processed after June 1 were done against that change. The processing date is indicated in the tab data header located in the upper right hand corner.

4: Peak voltage variation.

Peak voltage in the A4 wavelength ramp is checked every 10th scan and the wavelength vs A4 calibration is rescaled at this time. However, even the normal ± 1 count variations of V_{A4} /peak can cause a few percent variation in those regions of very low signal and low

ORIGINAL PAGE IS
OF POOR QUALITY

sensor responsivity, i.e., the 0.4 - 0.45 μ regions. It is doubtful that a worthwhile improvement in accuracy is feasible, even with more complex treatment of the wavelength ramp "A4. This seems to be a more or less intrinsic uncertainty of the S191 instrument.

A user requiring the utmost in accuracy in this region might consider ordering raw data for hand reduction. Realize, however, this is the same region where off-band radiation and sensor drift also hit hardest.

5: Sensor Drift.

For reasons as yet unknown the sensor responsivity drifts slightly with time. Corrections based on internal component temperatures, as described in PHO TR524, do not fully correct for such temporal effects. The drift in both short wavelength and thermal regions seems to be about 3% in 20 min. or 0.15%/min. For reasons dictated by the computer program as written and computer core storage available for coding, calibration is done using only the first (pre-pass) autocal. The accuracy is "perfect" at that time but degrades in a presumably linear fashion throughout the pass.

Fortunately, this drift, if it presents a problem to the user, is readily corrected. Radiances will be run for the ambient blackbody and SWL cal lamp during the post-pass autocal. Refinement of data can be made as follows:

SWL

At any wavelength:

N_{cal} is the correct SWL cal source radiance from column "SWL SPECTR RAD RADNCE" in pre-pass responsivity tabs. (See Table I)

t_1 is time of pre-pass autocal

t_2 is time of post-pass autocal

t is time of data take; $t_1 < t < t_2$

N_{524} is radiance calculated for site at time t :

"SWLI APERT CH-A2," "A3," or "A5" (as appropriate)

N_{post} is radiance calculated for cal source in post-pass autocal: "SWLI APERT CH-A2," "A3," or "A5" (as appropriate)

Assuming a drift in responsivity that is linear in time between the two autocals,

$$N_{corrected} = \frac{t - t_1}{t_2 - t_1} \cdot \frac{N_{post}}{N_{cal}} \cdot N_{524}$$

Note that $(N_{\text{post}}/N_{\text{cal}})$ shows the extreme correction that would be applied to interior data. If it's close enough to unity for the applications analysis being performed, this linear scaling is not necessary.

Thermal

In the thermal region, the quantity proportional to responsivity is not $N_{\text{cal source}}^{-1}$ but $(N_{\text{cal source}} - N_{\text{reference}})^{-1}$. (See eq 6 & 7, paragraph 4.3.4.2.E of PHO TR 524 CH 1 where $I_a(\lambda) = N_{\text{cal source}}$ and $I_r(\lambda) = N_{\text{reference}}$). The blackbody radiance from the ambient cal source at post-pass time t_2 is calculable at any wavelength $\lambda(\mu)$ from

$$B(\lambda, T_{\text{amb}}) = \frac{11909}{\lambda^5 [\text{Exp}(\frac{14388}{\lambda T_{\text{amb}} (\text{K})}) - 1]} \quad \text{in } \frac{\text{watts}}{\text{cm}^2 \text{ster } \mu}$$

The difference between this radiance at each wavelength and the corresponding radiance from column "LWLI CALIB CH-A6" for the post-pass autocal radiances is the error accumulated during the pass. Taking that error as zero at the time t_2 of the pre-pass autocal and the variation as linear in time, one can easily interpolate a ΔN for the time of his data, t , t_2 be added to the value of "LWLI CALIB CH-A6" (or "A1") at that time. In principle, to correct the radiance of real interest, "LWLI APERT CH-A6" (or "A1") one should proceed as in PHO TR524 to correct for mirror effects. In practice, the uncertainties in accounting for the mirror effect are probably larger than the error generated by taking $(\text{LWLI APERT})' = (\text{LWLI APERT}) + \Delta N$ as the corrected aperture radiance.

6: Off-Band Radiation.

The filterwheel leaks a small amount of off-band radiation - about 0.01%. This is a normal characteristic of such filter-wheels and normally presents no problems. However, in those cases from 0.4 - 0.5 μ , 2.0 - 2.5 μ , 6.0 - 7.0 μ , and 14 - 15 μ where (a) signals from a terrestrial target are low, (b) sensor responsivity is low, and (c) filterwheel transmission is low (as in most of the cases), the 0.01% leaking through, integrated over the entire detector response range, may become an appreciable compared to the in-band radiation

through the filterwheel narrow spectral resolution bandpass. We have formulated an approach to correcting the off-band contamination, and are in the process of evaluating its usefulness. A second pass processing is being considered to correct for these effects after S191 processing has been completed. Implementation of this processing at JSC, however, is by no means certain. Meanwhile, the user may consider our algorithms to evaluate his sensitivity to off-band radiation and, if desired, perform his own corrections:

Define the dimensions of some quantities:

$$\text{Radiance responsivity: } [R] = \frac{V}{W/cm^2 \cdot \text{str}} \quad (1)$$

$$\text{Spectral radiance responsivity: } [r] = \frac{V}{W/cm^2 \cdot \text{str} \cdot \mu} \quad (2)$$

$$\text{Spectral radiance: } [N] = \frac{W}{cm^2 \cdot \text{str} \cdot \mu} \quad (3)$$

(N is radiance in the SWL; and radiance difference, $I_{\text{source}} - I_{\text{reference}}$, in the IWL, as defined in PHO TR524.)

Consider the filter transmission, $\tau(\lambda, \lambda_0)$, to be separable into on-band and off-band transmissions. Take $\tau_{\text{on}}(\lambda_0)$ as the peak on-band transmission, with half-width $\Delta\lambda(\lambda_0)$. Take $\tau_{\text{off}}(\lambda, \lambda_0)$ as the transmission at λ at the position of maximum transmission for λ_0 .

$$\tau(\lambda, \lambda_0) = \tau_{\text{on}}(\lambda_0) + \tau_{\text{off}}(\lambda, \lambda_0) \quad (4)$$

The voltage out of the instrument at initial wavelength λ_0 is then

$$V(\lambda_0) = \int_0^{\infty} R(\lambda) N(\lambda) \tau(\lambda, \lambda_0) d\lambda \quad (5)$$

In practice the range of integration is the range of sensor non-zero response. Define $\Delta\lambda$ for the on-band transmission as the half-peak bandwidth.

Then, approximately,

$$V(\lambda_0) = R(\lambda_0) N(\lambda_0) \tau_{\text{on}}(\lambda_0) \Delta\lambda(\lambda_0) + \int_{\lambda_0}^{\infty} R(\lambda) N(\lambda) \tau_{\text{off}}(\lambda, \lambda_0) d\lambda \quad (6)$$

In most of the S191 calibration work so far, τ_{on} and $\Delta\lambda$ have been implicitly incorporated into the definition of radiance responsivity, $r^0(\lambda)$, as calculated in PHO TR524:

$$r^0(\lambda_0) = \frac{V(\lambda_0)}{N(\lambda_0)} \quad (7)$$

The SWL cal source effective radiance used to determine r^0 is in Table I. Keep in mind the distinction between R and r :

$$r = R \tau_{\text{on}} \Delta\lambda \quad (8)$$

ORIGINAL PAGE IS
OF POOR QUALITY

To calculate the off-band contamination, obtain the voltage output from a known input radiance. For the short wavelength, this known source is the calibrator used at KSC in pre-launch testing. Define the zeroth order responsivity:

$$R^0(\lambda_o) = \frac{V_o(\lambda_o)}{N_o(\lambda_o)\tau_{on}\Delta\lambda} \quad (9)$$

Using equation (7) in rewriting equation (6) as an integral equation in R , and putting the rearrangement into the form of a recursion:

$$R^{n+1}(\lambda_o) = R^n(\lambda_o) - \frac{1}{N_o(\lambda_o)\tau_{on}(\lambda_o)\Delta\lambda(\lambda_o)} \int_0^\infty N_o(\lambda)R^n(\lambda)\tau_{off}(\lambda)d\lambda \quad (10)$$

Iterate toward a stationary value of R^n and define that as being "the" value of responsivity:

$$R(\lambda_o) = \lim_{n \rightarrow \infty} R^n(\lambda_o) \quad (11)$$

Initial attempts at this technique point to a necessary revision of some of our values for the indicated parameters.

The quantity r^0 contains off-band contamination. For a source with the same relative spectral distribution as the cal source, the data calculated from r^0 will have compensating contamination. The quantity R is the result of attempts to eliminate off-band contamination from the responsivity. In applying R to detector output voltages, the contamination in those voltages must be taken into account, for there is (purposefully) no compensation present in that responsivity.

So, using the value of R as calculated above, perform a similar manipulation to get the uncontaminated target radiance.

$$N^0 = V/R \tau_{on}\Delta\lambda = V/r \quad (12)$$

$$N^{n+1}(\lambda_o) = N^n(\lambda_o) - \frac{1}{r(\lambda_o)} \int_0^\infty N^n(\lambda)R(\lambda)\tau_{off}(\lambda,\lambda_o)d\lambda \quad (13)$$

$$N = \lim_{n \rightarrow \infty} N^n \quad (14)$$

in order to ascertain whether off-band effects are significant in any particular spectrum, assume zeroth order values for N and R , and take $\tau_{\text{off}}(\lambda, \lambda_o)$ as a constant 0.01%.

$$\begin{aligned}
 \Delta N(\lambda_o) &\simeq \frac{1}{r^o(\lambda_o)} \int_0^\infty N^o(\lambda) R^o(\lambda) \tau_{\text{off}}(\lambda, \lambda_o) d\lambda \\
 &= \frac{1}{r^o(\lambda_o)} \int_0^\infty N^o r^o \frac{\tau_{\text{off}}}{\tau_{\text{on}} \Delta \lambda} d\lambda \\
 &\simeq \frac{10^{-4}}{r^o(\lambda_o)} \int_0^\infty N^o r^o \frac{1}{\tau_{\text{on}} \Delta \lambda} d\lambda
 \end{aligned} \tag{15}$$

In this equation, the responsivity is the one provided in tabular form with the radiance data; τ_{off} and $\Delta\lambda$ are included here (Table II).

The off-band contamination solution is being pursued further and evaluated under the Sensor Performance Evaluation project.

7: Missing SWL Wavelengths

S191 responsivity products processed from June 1, 1974, to June 25, 1974, lack wavelengths and radiance between 0.990μ and 1.10μ . This affects tape, tab, and plot radiance products S041-1, S042-3, and S043-2. The wavelength set has been revised as follows effective 6/26/74:

<u>λ set 6/1/74 - 6/25/74</u>	<u>λ set all later dates</u>
0.86 μ	0.86
0.87	0.88
0.88	0.90
0.89	0.92
0.90	0.94
0.915	0.96
0.93	0.98
0.945	1.00
0.96	1.02
0.975	1.04
0.990	1.06
1.10	1.08
1.12	1.10
.	1.12
.	.
.	.

0.86 μ	0.86
0.87	0.88
0.88	0.90
0.89	0.92
0.90	0.94
0.915	0.96
0.93	0.98
0.945	1.00
0.96	1.02
0.975	1.04
0.990	1.06
1.10	1.08
1.12	1.10
.	1.12
.	.
.	.

ORIGINAL PAGE IS
OF POOR QUALITY

Note that this generates a revision A to Table I, as appended to Table I.

PI's who are seriously affected by the earlier wavelength set during the affected SL3 passes should contact his PIMO representative.

TABLE I
S191 SWL Calibration Source Effective Radiance

$\lambda(\mu)$	$N(\text{W/cm}^2\text{-str-}\mu)$	$\lambda(\mu)$	$N(\text{W/cm}^2\text{-str-}\mu)$	$\lambda(\mu)$	$N(\text{W/cm}^2\text{-str-}\mu)$
.400	.8349 E-3	.740	.1744 E-1	1.44	.1355 E-1
.405	.8574 E-3	.750	.1800 E-1	1.48	.1238 E-1
.410	.8868 E-3	.760	.1848 E-1	1.50	.1192 E-1
.415	.9232 E-3	.770	.1892 E-1	1.52	.1197 E-1
.420	.9664 E-3	.780	.1932 E-1	1.54	.1162 E-1
.425	.1017 E-2	.790	.1967 E-1	1.56	.1128 E-1
.430	.1074 E-2	.800	.1998 E-1	1.58	.1095 E-1
.435	.1138 E-2	.810	.2033 E-1	1.60	.1065 E-1
.440	.1209 E-2	.820	.2055 E-1	1.62	.1036 E-1
.445	.1287 E-2	.830	.2071 E-1	1.64	.1008 E-1
.450	.1372 E-2	.840	.2083 E-1	1.66	.9815 E-2
.460	.1562 E-2	.850	.2053 E-1	1.68	.9560 E-2
.470	.1780 E-2	.860	.2050 E-1	1.70	.9316 E-2
.480	.2026 E-2	.870	.2046 E-1	1.72	.9189 E-2
.490	.2207 E-2	.880	.2041 E-1	1.74	.8929 E-2
.500	.2496 E-2	.890	.2034 E-1	1.76	.8666 E-2
.510	.2826 E-2	.900	.2026 E-1	1.78	.8398 E-2
.520	.3197 E-2	.915	.2012 E-1	1.80	.8159 E-2
.530	.3609 E-2	.930	.1945 E-1	1.81	.7643 E-2
.540	.4062 E-2	.945	.1929 E-1	1.88	.7101 E-2
.550	.4660 E-2	.960	.1917 E-1	1.92	.6317 E-2
.560	.5178 E-2	.975	.1909 E-1	1.96	.5804 E-2
.570	.5727 E-2	.990	.1905 E-1	2.00	.5411 E-2
.580	.6306 E-2	1.10	.1960 E-1	2.04	.5021 E-2
.590	.6915 E-2	1.12	.1987 E-1	2.08	.4786 E-2
.600	.7555 E-2	1.14	.1976 E-1	2.12	.4445 E-2
.610	.8365 E-2	1.16	.1957 E-1	2.16	.3945 E-2
.620	.9044 E-2	1.18	.1931 E-1	2.20	.3580 E-2
.630	.9734 E-2	1.20	.1823 E-1	2.24	.3174 E-2
.640	.1044 E-1	1.22	.1786 E-1	2.28	.2922 E-2
.650	.1134 E-1	1.24	.1756 E-1	2.32	.3173 E-2
.660	.1206 E-1	1.26	.1734 E-1	2.36	.3120 E-2
.670	.1278 E-1	1.28	.1790 E-1	2.40	.2923 E-2
.680	.1348 E-1	1.30	.1764 E-1	2.44	.2581 E-2
.690	.1416 E-1	1.32	.1723 E-1	2.48	.2095 E-2
.700	.1484 E-1	1.34	.1683 E-1		
.710	.1566 E-1	1.36	.1623 E-1		
.720	.1629 E-1	1.38	.1583 E-1		
.730	.1688 E-1	1.40	.1506 E-1		

ORIGINAL PAGE IS
OF POOR QUALITY

TABLE I ADDENDUM I

$\lambda(\mu)$	$N_{eff}(w/cm^2 \cdot str \cdot \mu)$
.92	.01958
.94	.01934
.98	.01907
1.00	.01979
1.02	.01981
1.04	.01980
1.06	.01977
1.08	.01970

ORIGINAL PAGE IS
ON POOR QUALITY

Table II

a. Spectral Resolution $\Delta\lambda$.

λ range	$\Delta\lambda$
.40 μ - .71 μ	0.0115 μ
.72 μ - 1.36 μ	0.0185 μ
1.38 μ - 2.48 μ	0.015 $\times \lambda$
6 μ - 16 μ	0.019 $\times \lambda$

b. In-Band Transmission τ_{on}

Assume $\tau_{on}(\lambda)$ is a smooth envelope for each region on which the τ_{on} values at the specified λ 's are samples.

Region	$\lambda(\mu)$	τ_{on}
.4 - .71 μ	.4	.20
	.49	.26
	.62	.22
	.73	.24
.72 - 1.36 μ	.68	.16
	.90	.21
	1.16	.18
	1.40	.20
1.38 - 2.48 μ	1.32	.23
	1.51	.40
	1.75	.53
	1.96	.61
	2.20	.63
	2.32	.60
	2.52	.63
... - 9.2 μ	5.8	.62
	6.5	.62
	7.5	.60
	8.5	.54
	9.5	.53
9.3 - 15.4 μ	9.2	.67
	10.7	.66
	12.3	.52
	13.7	.51
	14.9	.38
	15.8	.20

c. Off-Band Transmission τ_{off}

The noise in the measurement of τ_{off} by the filterwheel manufacturer is several times larger than the mean value. The mean off-band transmission throughout the entire range 0.4μ to 16μ is somewhere between 0.00% and 0.02% with 0.01% the best estimate presently possible. Updates will be provided when measurements are completed.

APPENDIX 3

S-191 DATA TAPES RECEIVED

Day	START AND END TIMES (HH:MM:SS)		JSC Tape Numbers
160	15:08:13	15:11:43	926493
160	15:08:13	15:11:43	926494
160	15:14:50	15:17:50	926501
160	15:14:50	15:17:50	926502
160	15:17:50	15:19:50	926503
160	15:17:50	15:19:50	926504
160	15:11:50	15:14:50	926500
160	15:11:50	15:14:50	926499
161	14:27:12	14:28:18	926333
161	14:27:12	14:28:18	926334
161	14:38:02	14:39:49	926337
161	14:38:02	14:39:49	926338
163	12:57:48	13:00:10	926605
163	12:57:48	13:00:10	926606
163	13:12:46	13:14:34	926609
163	13:12:46	13:14:34	926610
164	13:51:00	13:53:00	926544
164	13:59:00	13:53:00	926545
164	13:51:00	13:53:00	926543
164	13:51:00	13:53:00	926546
164	14:00:00	14:01:05	926612
164	14:00:00	14:01:05	926611
164	14:01:15	14:02:00	926542
164	14:01:15	14:02:00	926541
165	14:41:13	14:43:46	926430
165	14:41:13	14:43:46	926428
215	18:11:20	18:13:25	917471
215	18:11:20	18:13:25	917472
215	18:19:00	18:22:00	917475
215	18:19:00	18:22:00	917476
215	18:22:00	18:24:00	917477
215	18:22:00	18:24:00	917478
215	18:16:30	18:19:00	917473

Day	START AND END TIMES (HH:MM:SS)		JSC Tape Numbers
215	18:16:30	18:19:00	917474
217	15:05:00	15:07:00	916519
217	15:05:00	15:07:00	916520
224	15:01:00	15:02:00	917745
224	15:01:00	15:02:00	917744
224	14:58:00	15:58:00	917743
224	14:58:00	15:02:00	917746
224	14:43:05	15:02:00	906528
244	15:29:16	15:31:13	916607
244	15:29:16	15:31:13	916608
247	15:00:00	15:01:00	927256
247	15:00:00	15:01:00	927257
247	14:56:40	15:00:00	927254
247	14:56:40	15:00:00	927255
247	14:53:40	14:56:40	907799
247	14:53:40	14:56:40	907798
252	19:08:50	19:13:00	919014
252	19:08:50	19:13:00	919013
252	19:11:50	19:13:00	919015
253	20:03:48	20:05:31	919018
254	13:10:40	13:13:40	917579
254	13:10:40	13:13:40	917580
258	16:40:50	16:43:50	917703
258	16:40:50	16:43:50	917704
258	18:21:05	18:22:00	917778
258	18:21:05	18:22:00	917777
258	16:43:50	16:46:10	917705
258	16:43:50	16:46:10	917585
255	17:04:40	17:06:50	916691
255	17:04:00	17:06:50	916714
260	15:05:00	15:06:30	918141
260	15:05:00	15:06:30	918140
260	15:05:00	15:06:30	916498
260	15:05:00	15:06:30	916497
335	17:26:43	17:27:37	924443
335	17:26:43	17:27:37	924444
336	16:42:57	16:44:32	921288
336	16:42:57	16:44:36	921341
335	17:26:43	17:27:37	926836

START AND END TIMES

Day	START (HH:MM:SS)	END (HH:MM:SS)	JSC Tape Numbers
001	13:25:54	13:28:33	921405
001	13:25:54	13:28:33	921404
004	19:25:48	19:27:48	921406
004	19:25:48	19:27:48	921407
004	19:27:48	19:29:48	921408
004	19:27:48	19:29:48	921409
007	17:19:20	17:22:10	921424
007	17:19:20	17:22:10	921423
009	15:53:31	15:55:47	924435
009	15:53:31	15:55:47	924436
024	18:00:46	18:02:48	922646
024	18:00:46	18:02:48	922647
025	17:17:00	17:20:25	922650
025	17:17:00	17:20:25	922651
026	20:06:57	20:09:25	922722
026	20:06:57	20:09:25	922715
026	19:45:01	19:45:44	922721
026	19:45:01	19:45:44	922716
027	12:50:00	12:53:00	922749
027	12:50:00	12:53:00	922748
028	18:27:12	18:30:33	922761
028	18:27:12	18:30:33	922758
031	16:21:11	16:22:58	923022
031	16:21:11	16:22:58	923021
031	16:12:29	16:13:09	924449
031	16:12:29	16:13:09	924450
031	14:53:00	14:55:00	922893
031	14:53:00	14:55:00	922765
031	14:55:00	14:57:00	922894
031	14:55:00	14:57:00	922766
032	17:09:18	17:12:00	922921
032	17:09:18	17:12:00	922919
032	17:12:00	17:14:40	923131
032	17:12:00	17:14:40	923130
032	16:55:00	16:57:00	923111
032	16:55:00	16:57:00	923110
032	16:53:00	16:55:00	923028
032	16:53:00	16:55:00	923025

APPENDIX 4

S-192 DATA TAPES
(line straightened, all 13 channels included — note duplication)

Day	START AND END TIMES		JSC Tape Numbers
	HH:MM:SS:QSEC $\times 10^{-4}$		
244	15:29:26:3055	15:29:39:9989	933414
244	15:29:26:3055	15:29:39:9989	933415
244	15:29:26:3055	15:29:39:9989	933416
244	15:29:39:3768	15:29:55:9916	933417
244	15:29:39:3768	15:29:55:9916	933418
244	15:29:52:38	15:29:55:9916	933419
244	15:29:55:3798	15:30:11:9950	933420
244	15:29:55:3798	15:30:11:9950	933421
244	15:29:55:3798	15:30:11:9950	933422
244	15:30:11:3834	15:30:21:8903	933423
244	15:30:11:3834	15:30:21:8903	933424
244	15:30:23:3726	15:30:43:9908	933425
244	15:30:23:3726	15:30:43:9908	933426
244	15:30:23:3726	15:30:43:9908	933427
244	15:30:23:3776	15:30:43:9908	933428
244	15:30:43:3685	15:30:59:9944	933429
244	15:30:43:3685	15:30:59:9944	933430
244	15:30:43:3685	15:30:59:9944	933431
244	15:30:59:3719	15:31:15:9979	933432
244	15:30:59:3717	15:31:15:9979	933433
244	15:30:59:3717	15:31:15:9979	933434
244	15:31:15:6705	15:31:20:8925	933435
255	17:05:05:5619	17:05:15:9949	933858
255	17:05:05:5619	17:05:15:9949	933859
255	17:05:15:3410	17:05:31:9982	933860
255	17:05:15:34110	17:05:31:9982	933861
255	17:05:15:3410	17:05:31:9982	933862
255	17:05:31:3129	17:05:45:5334	933863
255	17:05:31:3129	17:05:45:5334	933864
255	17:05:31:3129	17:05:45:5334	933865

START AND END TIMES

Day	HH:MM:SS:QSEC $\times 10^{-4}$		JSC Tape Numbers
335	17:27:07.9	17:27:28.9	928794
335	17:27:07.7	17:27:28.9	928795
335	17:27:07.7	17:27:28.9	928796
335	17:27:23.6	17:27:39.9	928797
335	17:27:23.6	17:27:39.9	928798
335	17:27:23.6	17:27:39.9	928799
335	17:27:39.0	17:27:45.7	928800
335	17:27:39.6	17:27:45.7	928801
336	16:43:04.80	16:43:21.98	934156
336	16:43:04.80	16:43:21.98	934157
336	16:43:04.80	16:43:21.98	934158
336	16:43:21.07	16:43:39.99	934159
336	16:43:21.07	16:43:39.99	934160
336	16:43:21.07	16:43:39.99	934161
336	16:43:21.07	16:43:39.99	934162
*			
021	20:17:05:1507	20:17:15.	
021	20:17:05:1507	20:17:15.	
021	20:17:05:14.8776	20:17:31.9993	
021	20:17:05:14.8776	20:17:31.9993	
021	BAD	20:17:31.9993	
021	20:17:30:8709	20:17:41.9996	
021	20:17:30:8709	20:17:41.9996	
*			
024	18:01:24:2502	18:01:34:9999	927268
024	18:01:24:2502	18:01:34:9999	927269
024	18:01:34:396	18:01:51:9948	927270
024	18:01:34:396	18:01:51:9948	927271
024	18:01:34:396	18:01:51:9998	927272
024	18:01:51:0353	18:02:08:9904	927273
024	18:01:51:0353	18:02:08:9904	927274
024	18:01:51:0353	18:02:08:9904	927275
024	18:02:08:0798	18:02:27:9894	927276
024	18:02:08:0298	18:02:27:9894	927277
024	18:02:08:0298	18:02:27:9894	927278

*Julian Day of second year – add 365 to this value to compare with S-190 dates.

START AND END TIMES

Day	HH:MM:SS:QSEC $\times 10^{-4}$		JSC Tape Numbers
*			
025	17:17:03:10	17:17:19.99	933206
025	17:17:19:10	17:17:35.99	933207
025	17:17:19:10	17:35:35.99	933208
025	17:17:35:08	17:17:55.99	933209
025	17:17:35:08	17:17:55.99	933210
025	17:17:35:08	17:17:55.99	933211
025	17:17:56:66	17:18:08.99	933212
025	17:17:56:66	17:18:08.99	933213
025	17:18:24:64	17:18:36.99	933214
025	17:18:08:71	17:18:24.99	933215
025	17:18:08:71	17:18:24.99	933216
025	17:18:24:64	17:18:36.99	933217
*			
031	16:11:58:11	16:12:05.99	934208
031	16:12:05:02	16:12:22:00	934209
031	16:12:05:02	16:12:22:00	934210
031	16:12:05:02	16:12:22:00	934211
031	16:12:21:01	16:12:31.99	934212
031	16:12:21:01 (BAD)	16:12:31.99	934213

*Julian Date of second year — add 365 to this value to compare with S-190 dates.

APPENDIX 5

S-190 DATA WHICH HAS BEEN STEREOGRAPHICALLY CONTOURED

Roll	Frames	FIRST FRAME		Longitude (DDD/MM)
		DDD/HH/MM	Latitude	
A2	87/88	393/18/30	01 51N	076 53W
2	237/238	165/14/42	39 01N	115 20W
8	157/158	160/15/11	31 45N	081 01W
8	267/268	161/14/39	02 46N	050 10W
14	139/140	163/12/57	45 14N	091 18W
14	146/147	163/12/58	43 37N	086 60W
14	157/158	163/13/00	40 47N	080 46W
14	200/201	163/13/14	02 50N	040 47W
14	239/240	164/13/52	36 35N	092 24W
14	256/257	164/13/54	30 58N	084 50W
24	40/41/42	215/18/13	10 42N	079 08W
25	242/243	224/14/58	00 29S	074 57W
30	252/253/254	224/15/00	05 27S	071 13W
42	81/82			
62	412/413/414/415/416	386/20/17	12 40N	070 51W

APPENDIX 6

Combined S-191, S192, and Stereographically Contoured S-190 data. The S-192 data has been formed into reflectance maps, phase maps, and brightness temperature maps. All S-192 data and contoured cloud altitude data are to the same horizontal scale. The grid on the contoured data is 10 km.

Reflectance and brightness temperature spectra were chosen to sample the same scene as given in the S-192 maps.

S192 TEMPERATURE-COLOR CHART

TEMPERATURE INTERVAL (°K)

190 - 196

197 - 204

205 - 211

212 - 218

219 - 225

226 - 232

233 - 239

240 - 246

247 - 253

254 - 260

261 - 267

268 - 274

275 - 281

282 - 288

289 - 295

296 - 302

S192 TEMPERATURE-COLOR CHART

TEMPERATURE INTERVAL (°K)

190 - 196

197 - 204

205 - 211

212 - 218

219 - 225

226 - 232

233 - 239

240 - 246

247 - 253

254 - 260

261 - 267

268 - 274

275 - 281

282 - 288

289 - 295

296 - 302

A62 a

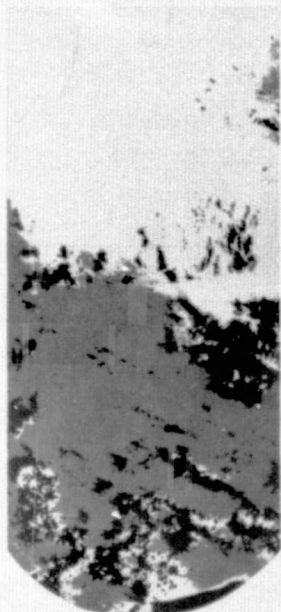
DAY 163

1973

REFLECTANCE
(S-192 CHANNEL 11)



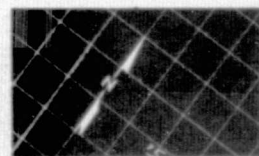
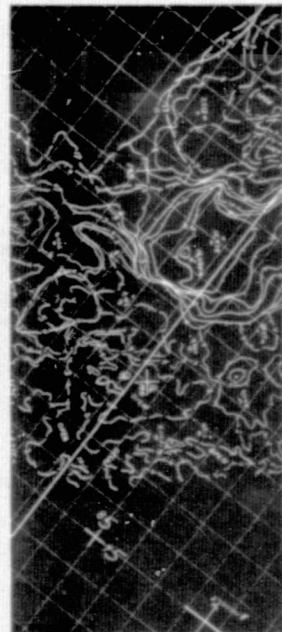
PHASE
MAP



BRIGHTNESS
TEMPERATURE
(S-192 CHANNEL 21)



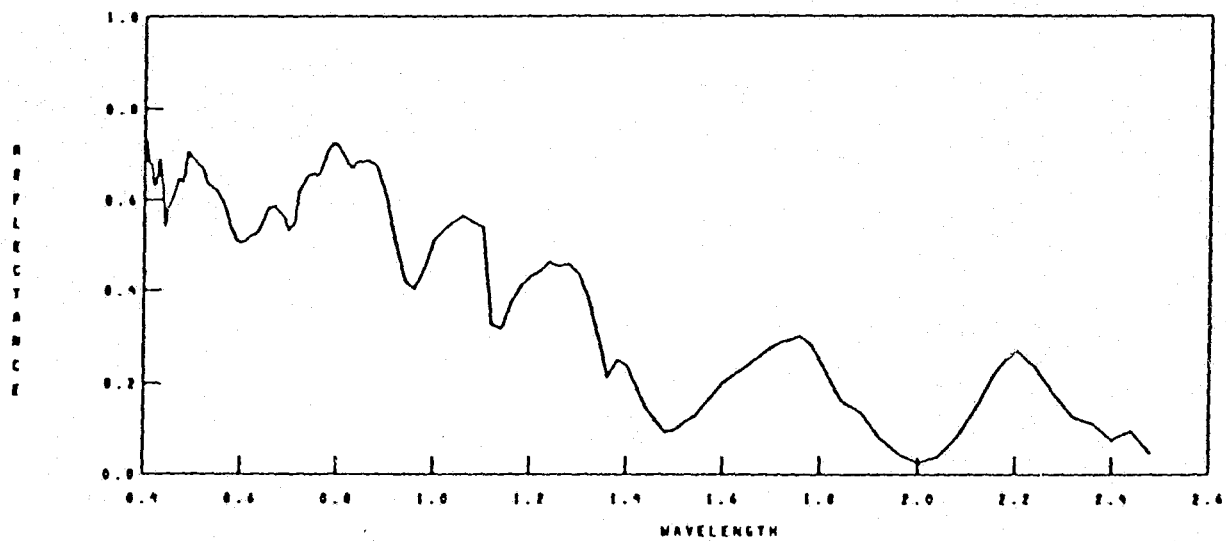
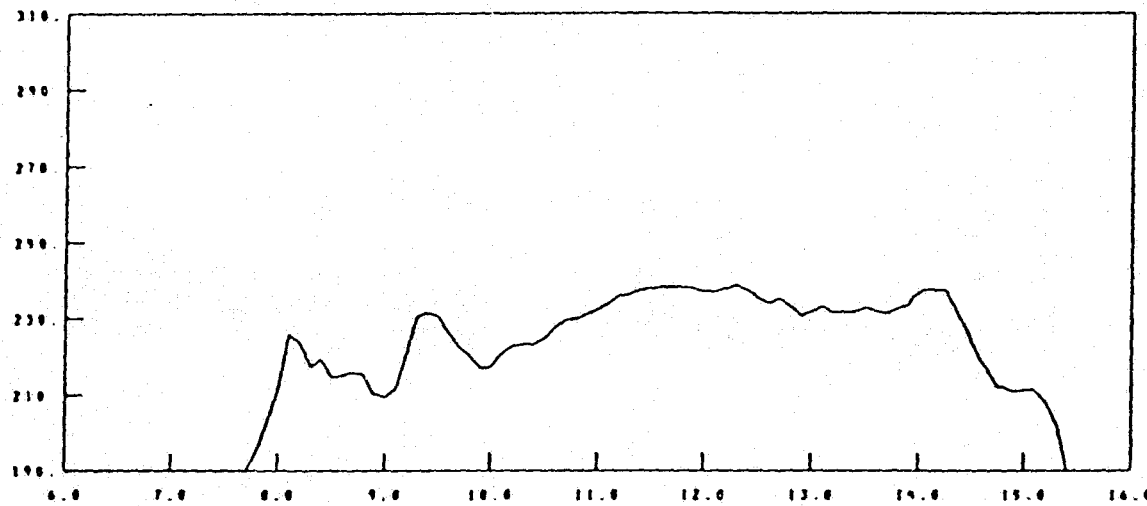
STEREOGRAPHIC
CLOUD HEIGHT
CONTOURS



S191 DATA - 96

MM DD YY MM MM SS SUN ZENITH ANGLE LATITUDE LONGITUDE

6 12 93 13 13 31 0.0 8.98 92.38



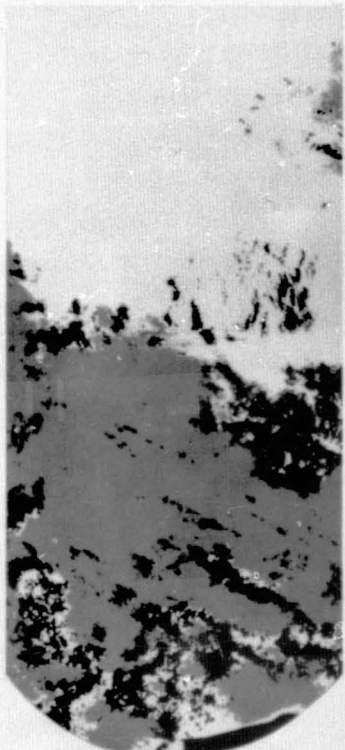
DAY 163

1973

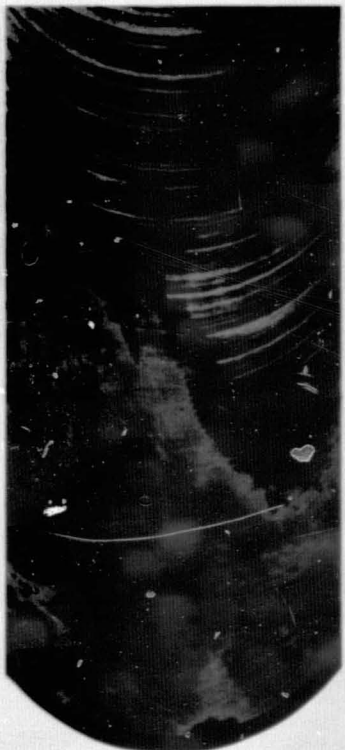
REFLECTANCE
(S-192 CHANNEL 11)



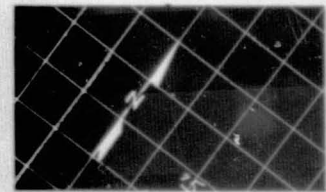
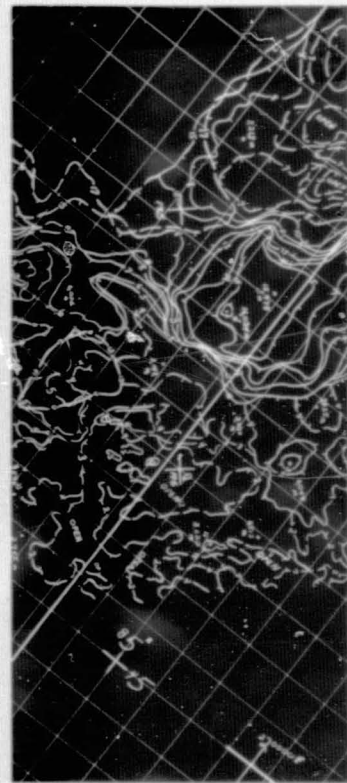
PHASE
MAP



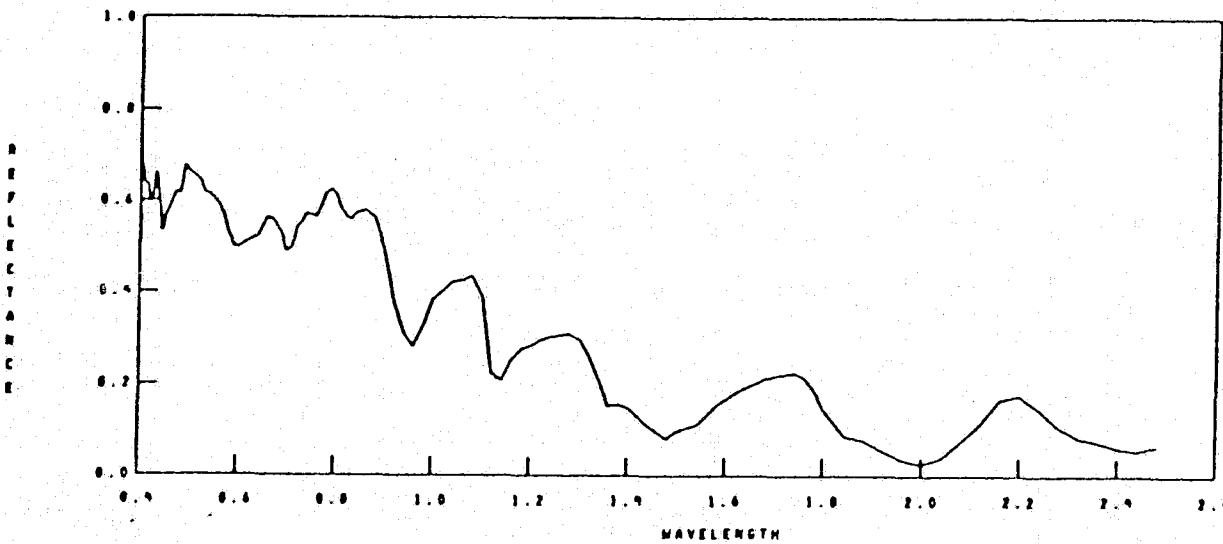
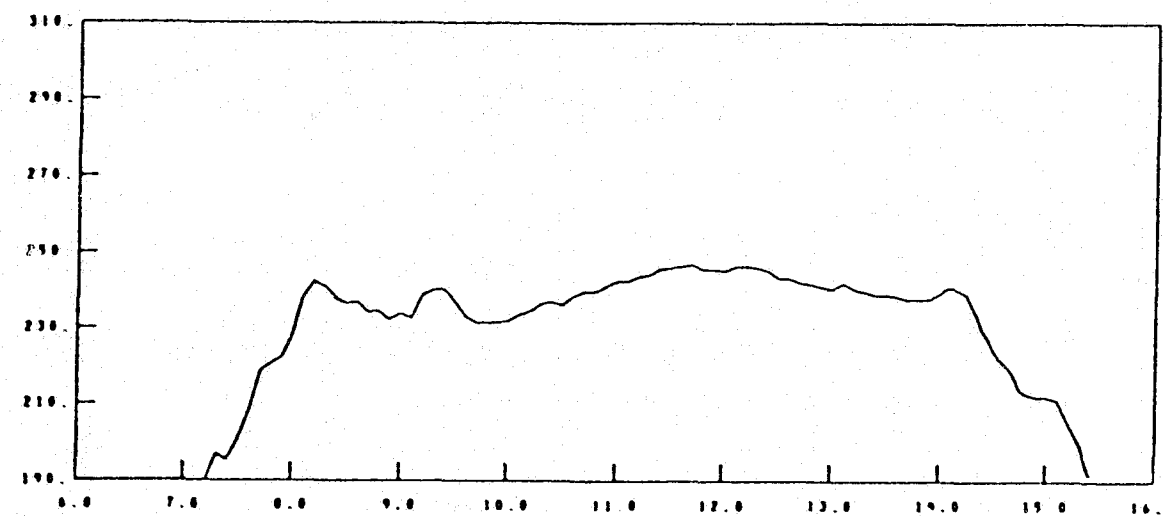
BRIGHTNESS
TEMPERATURE
(S-192 CHANNEL 21)



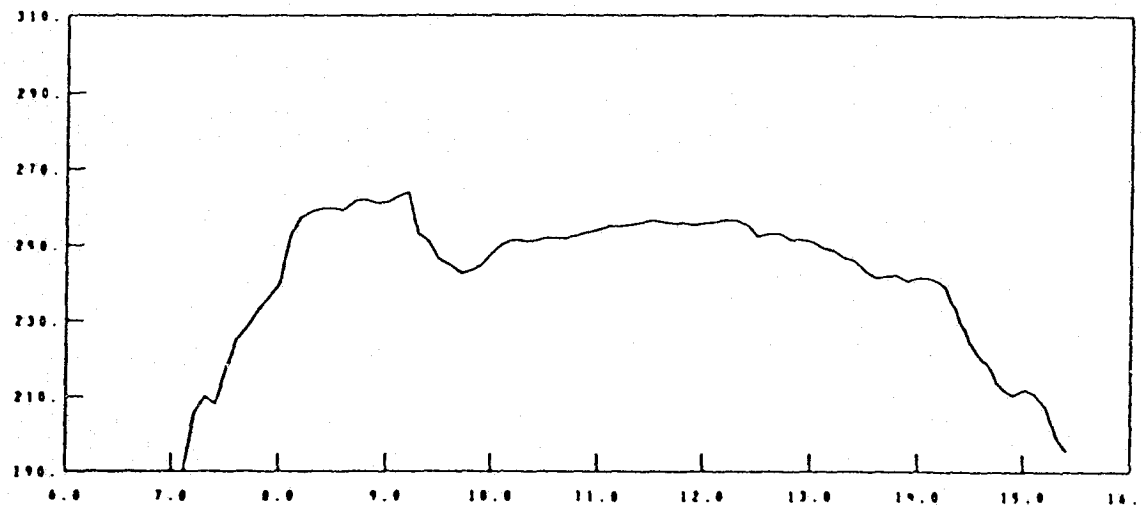
STEREOGRAPHIC
CLOUD HEIGHT
CONTOURS



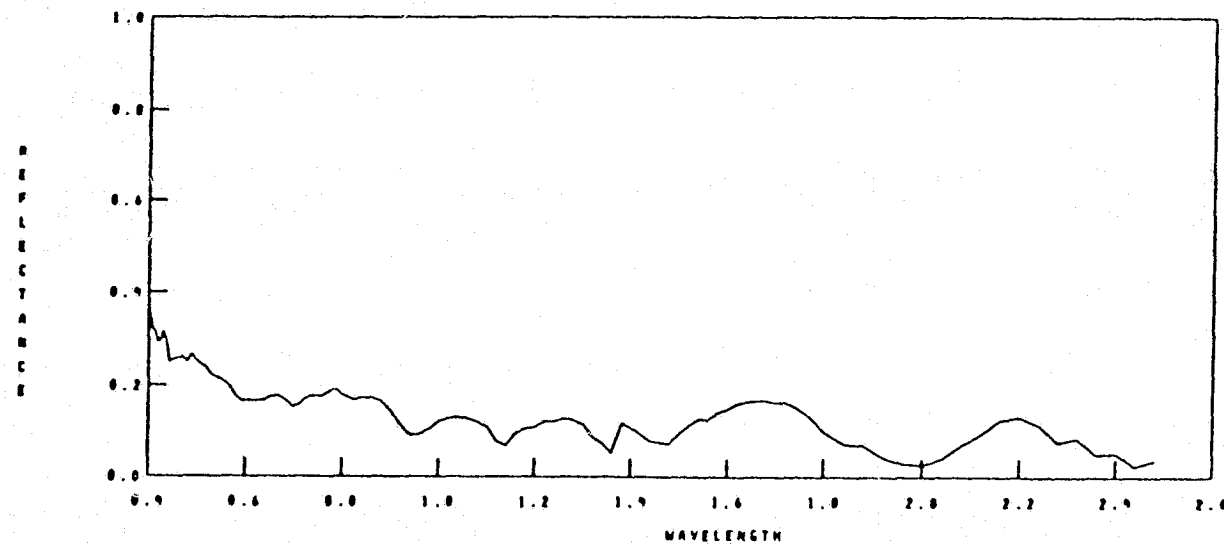
S191 DATA 50

RR 00 Y2
6 12 73RR RR SS
13 13 35SUN ZENITH ANGLE
0.0LATITUDE
9.80
LONGITUDE
92.29

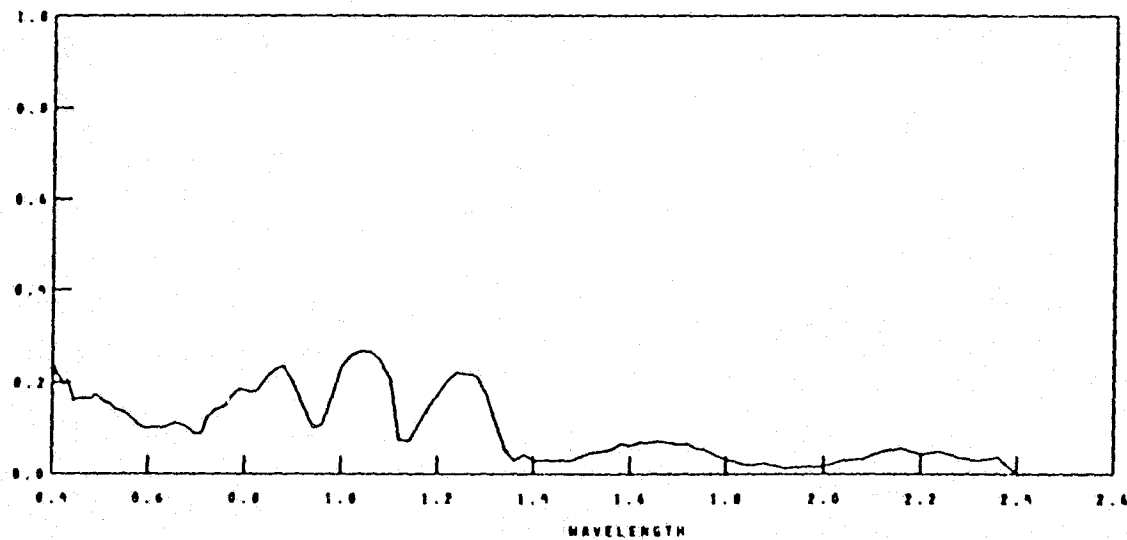
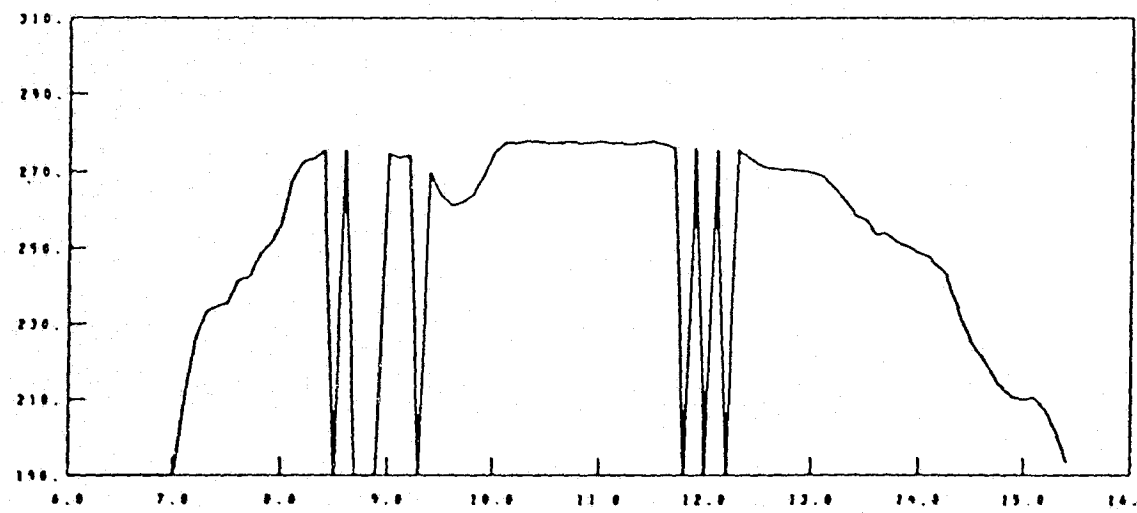
SITE DATA - 59

HH DD YY
06 12 73HH MM SS
13 13 39SUN ZENITH ANGLE
6.0LATITUDE
49.61
LONGITUDE
42.11

A6-6

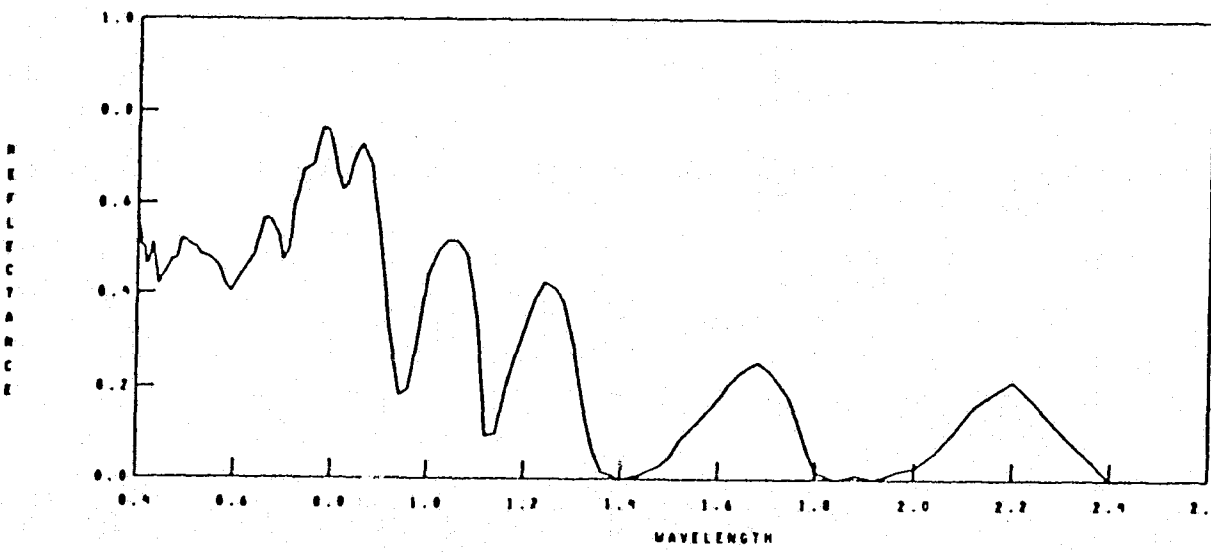
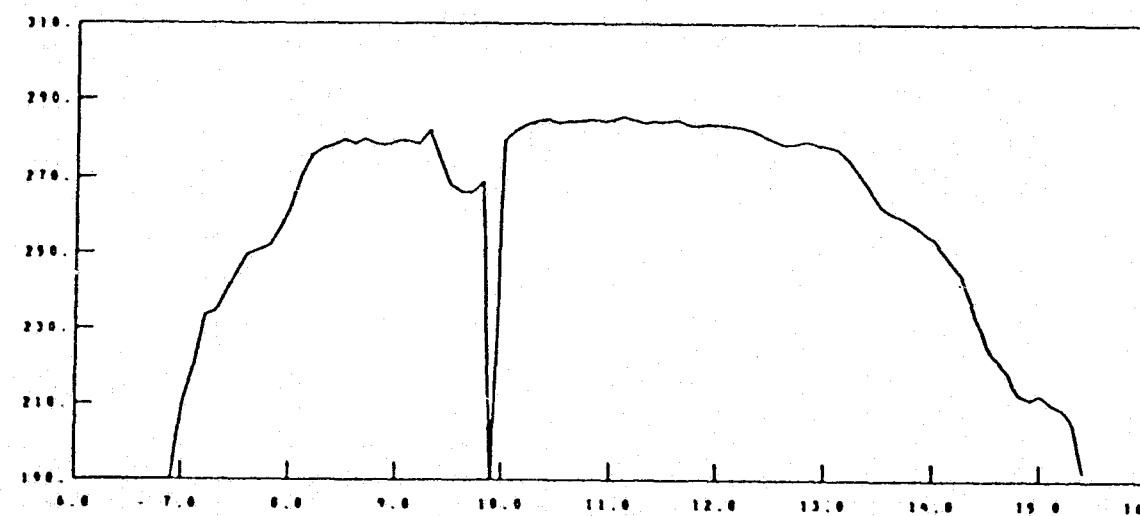


S191 DATA 50

MM DD YY
6 12 73HH MM SS
13 13 43SUN ZENITH ANGLE
0 0LATITUDE
4.43
LONGITUDE
91.97

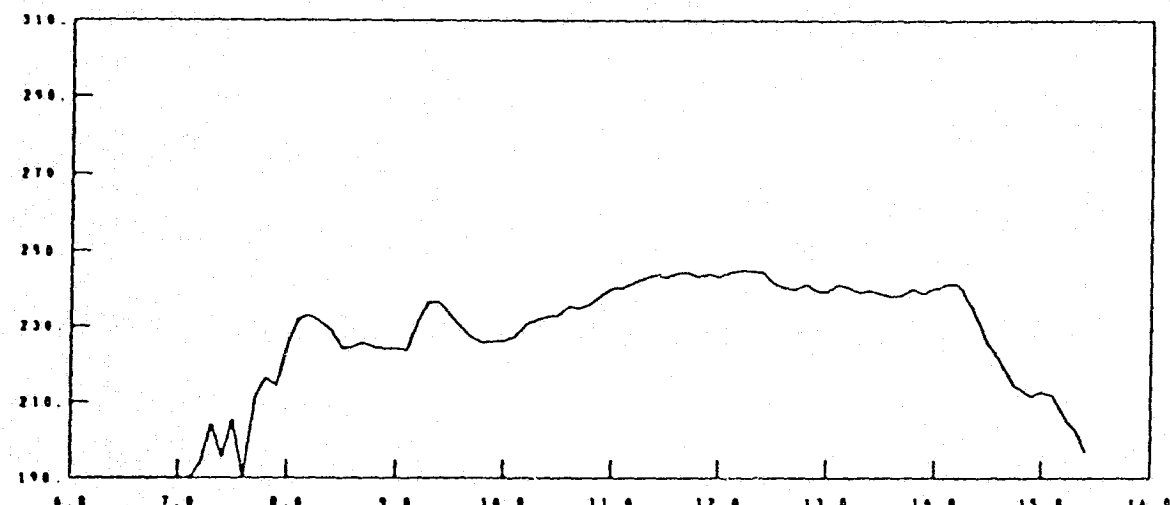
A6-7

S191 DATA 62

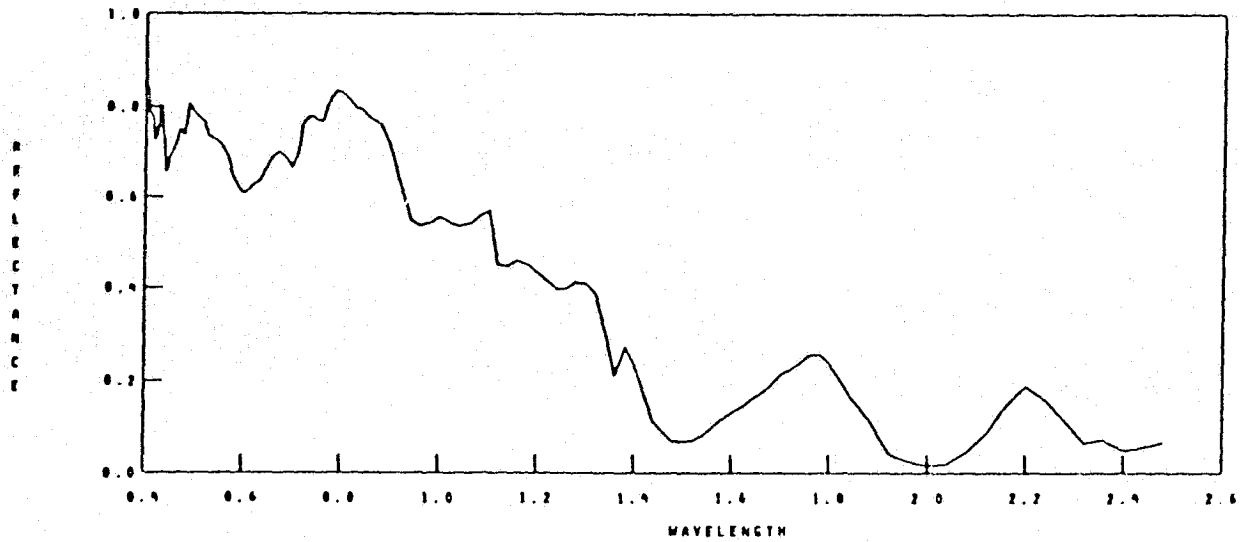
MM DD YY
6 12 73HH MM SS
13 13 46SUN ZENITH ANGLE
0.0LATITUDE
9.29LONGITUDE
91.02

A6-8

S191 DATA 68

RR DD YY
6 12 73HH MM SS
13 13 52SUN ZENITH ANGLE
0.0LATITUDE
3.96
LONGITUDE
-91.61

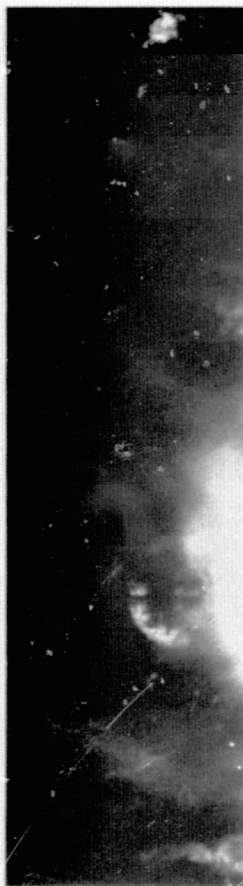
A6-9



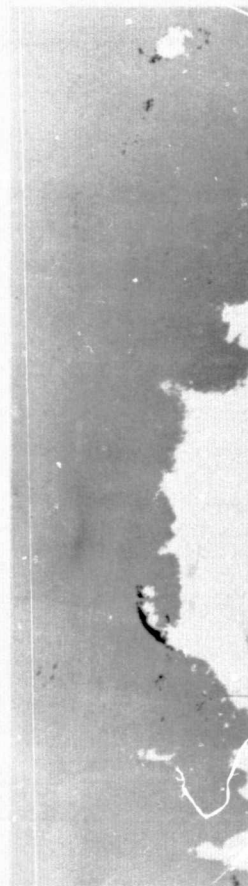
ORIGINAL PAGE IS
OF POOR QUALITY

DAY 255
1973

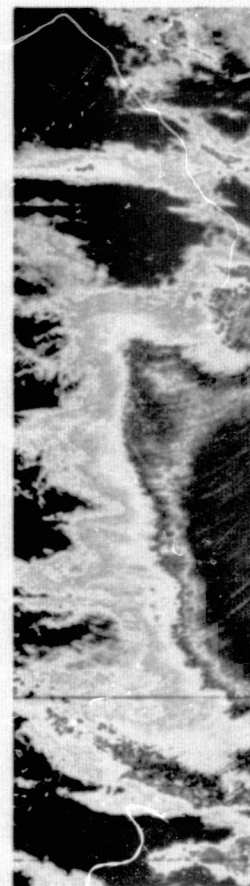
REFLECTANCE
(S-192 CHANNEL 11)



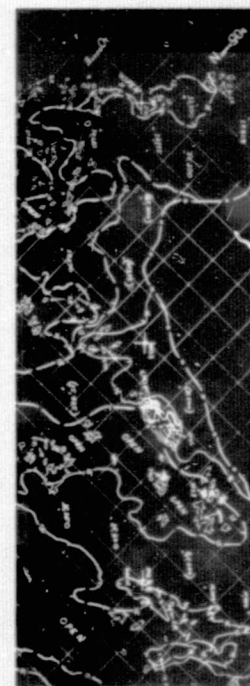
PHASE
MAP



BRIGHTNESS
TEMPERATURE
(S-192 CHANNEL 21)



STEREOGRAPHIC
CLOUD HEIGHT
CONTOURS



A6-10

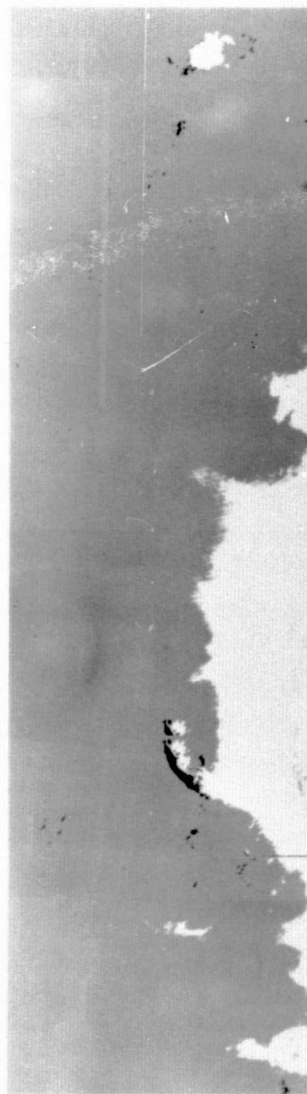
DAY 255

1973

REFLECTANCE
(S-192 CHANNEL II)



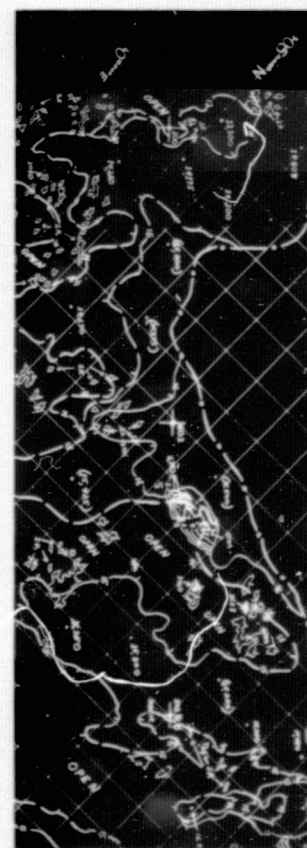
PHASE
MAP



BRIGHTNESS
TEMPERATURE
(S-192 CHANNEL 2I)

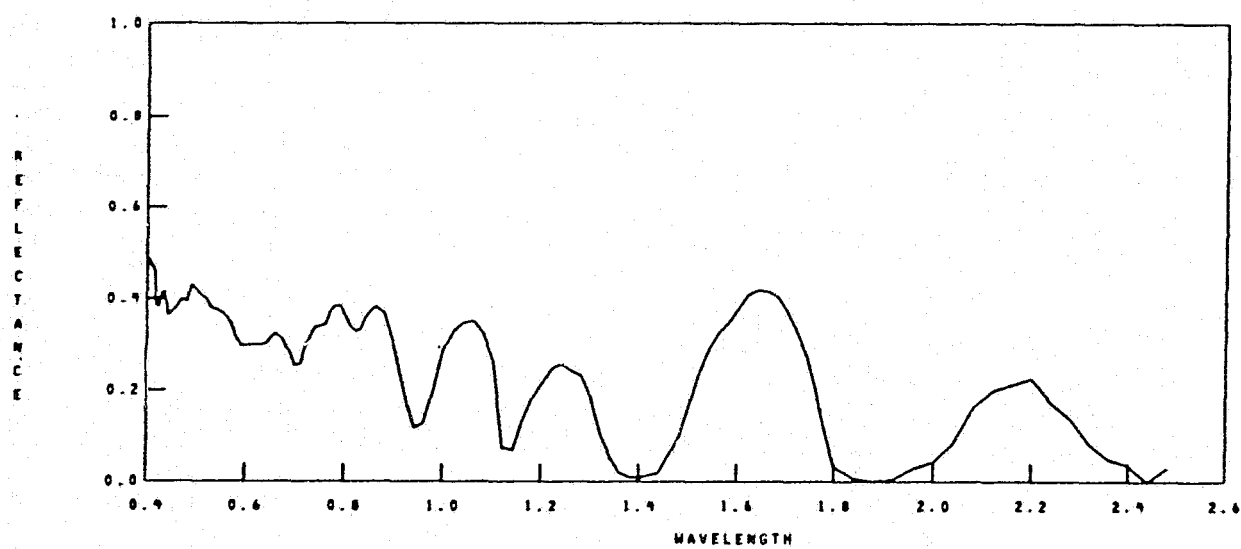
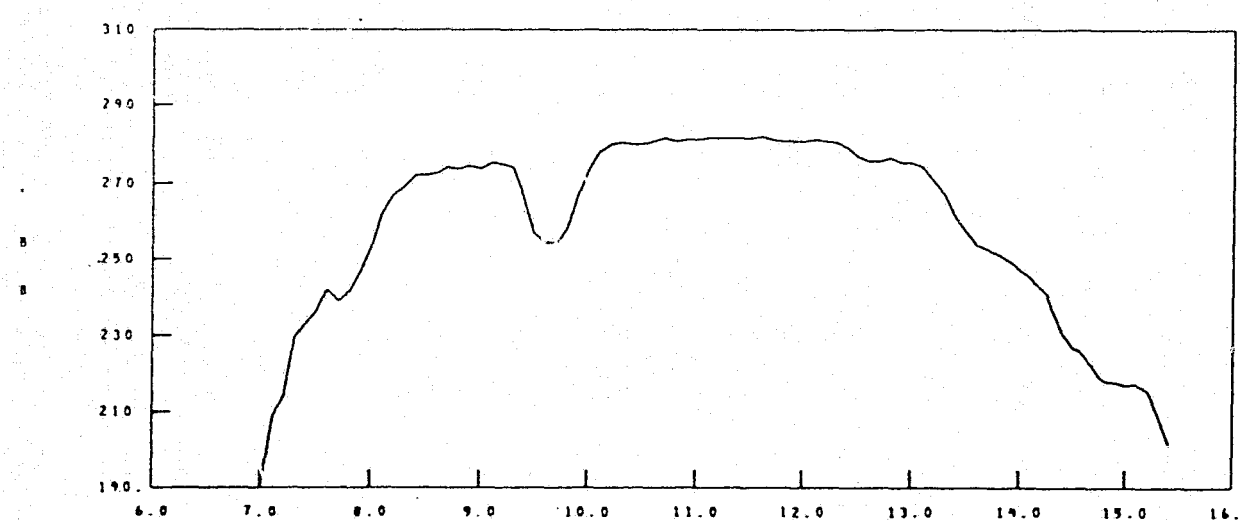


STEREOPHOTOGRAPHIC
CLOUD HEIGHT
CONTOURS



A6-102

5191 DATA -10

MM DD YY
9-12-73HH MM SS
17 4 49SUN ZENITH ANGLE
0.0LATITUDE
26 02LONGITUDE
91.59

A6-11

SI DATA 16

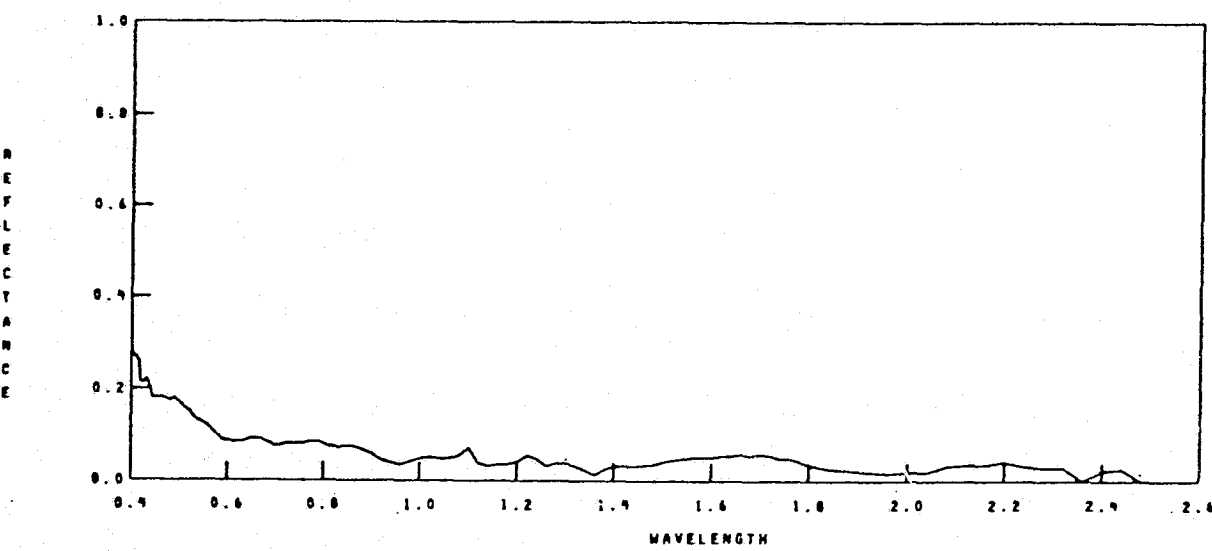
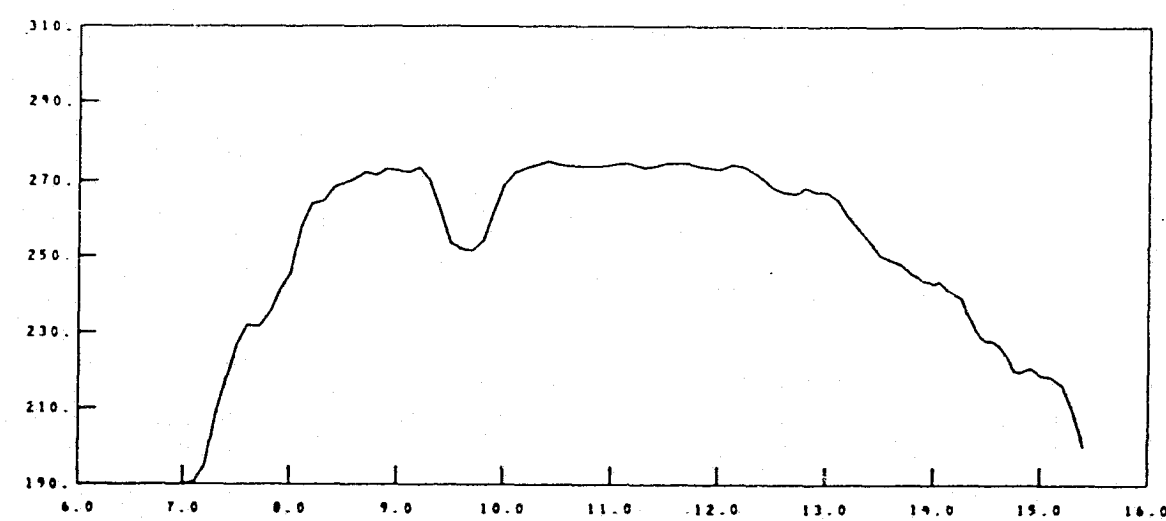
MM DD YY
9 12 73

HH MM SS
17. 4 54

SUN ZENITH ANGLE
0 0

LATITUDE
26 27

LONGITUDE
91.34



A6-12

S191 DATA 10

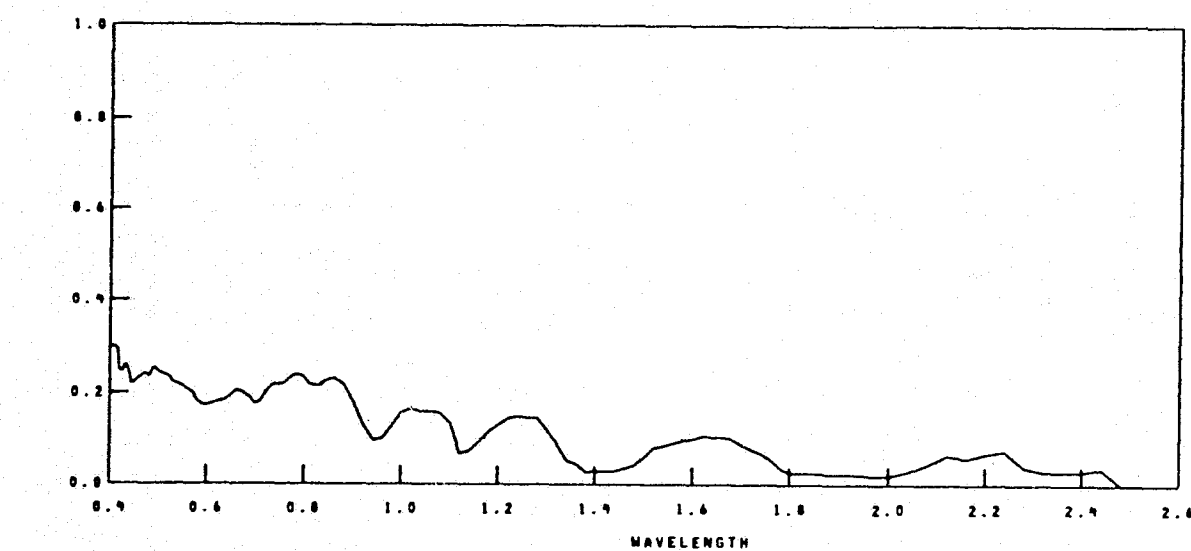
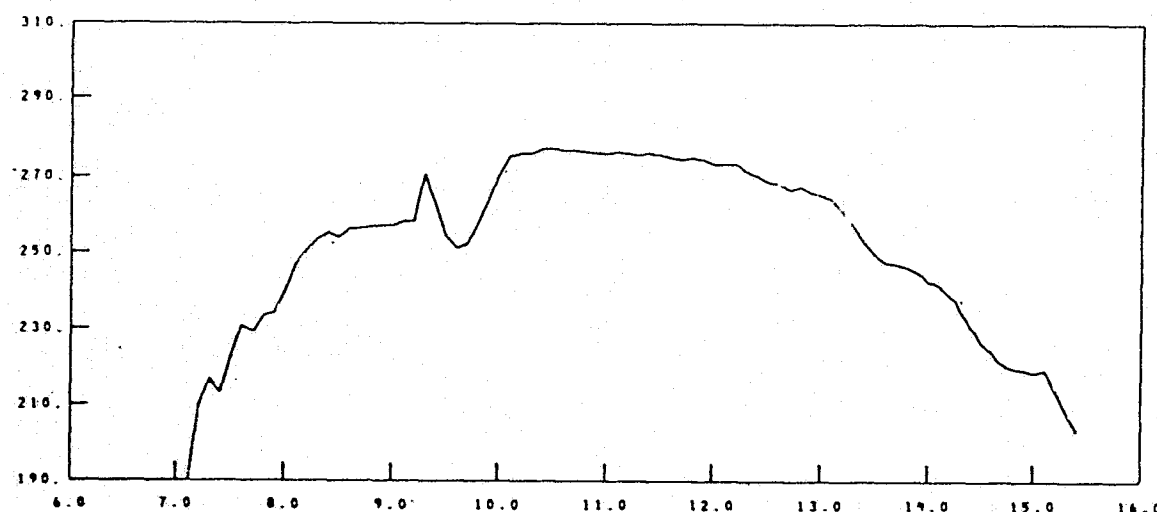
MM DD YY
9 12 73

HH MM SS
17 4 58

SUN ZENITH ANGLE
0.0

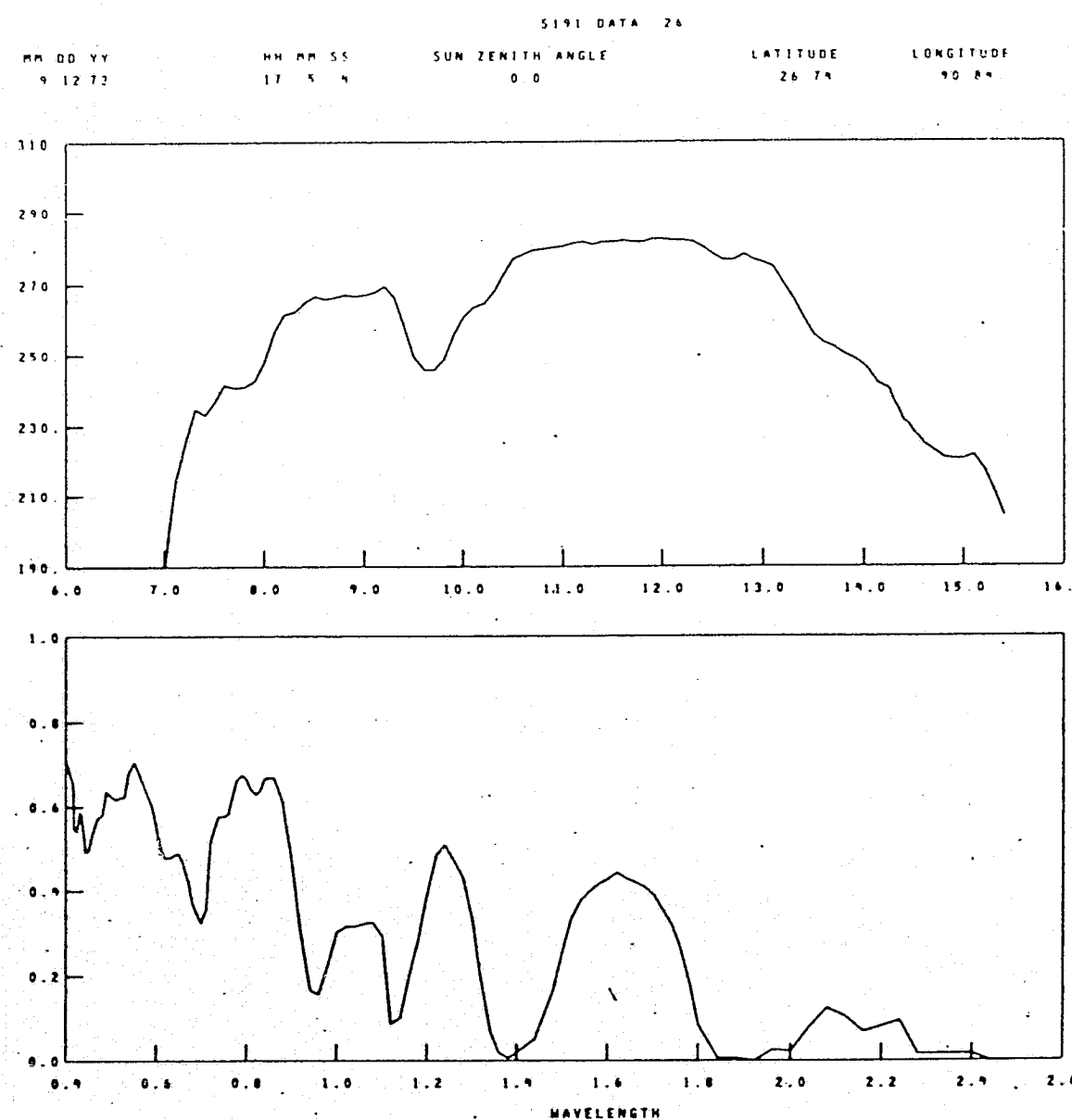
LATITUDE
26.44

LONGITUDE
-91.15

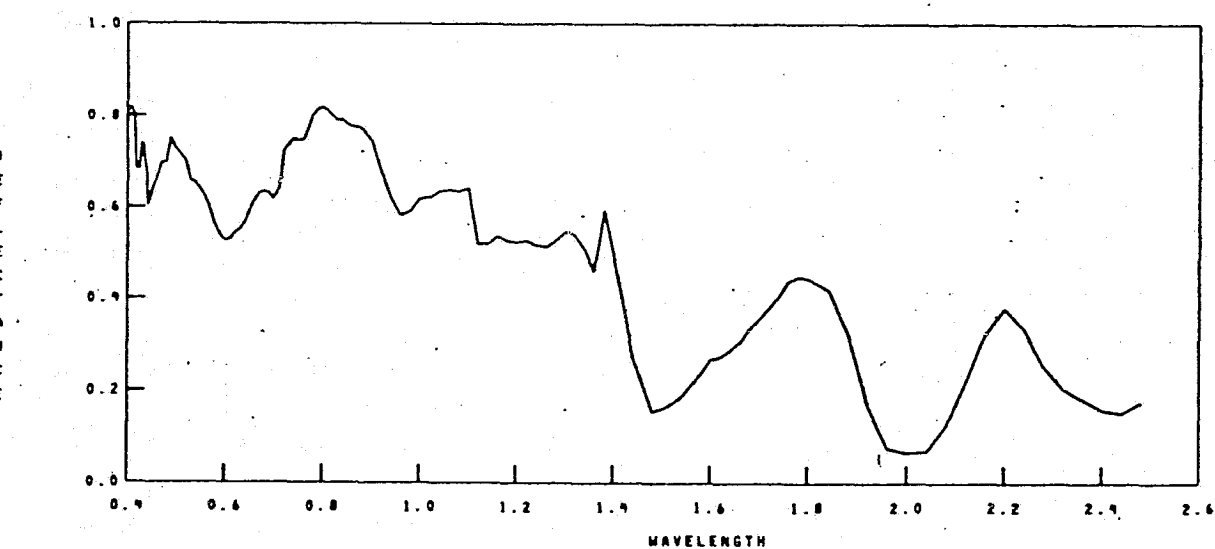
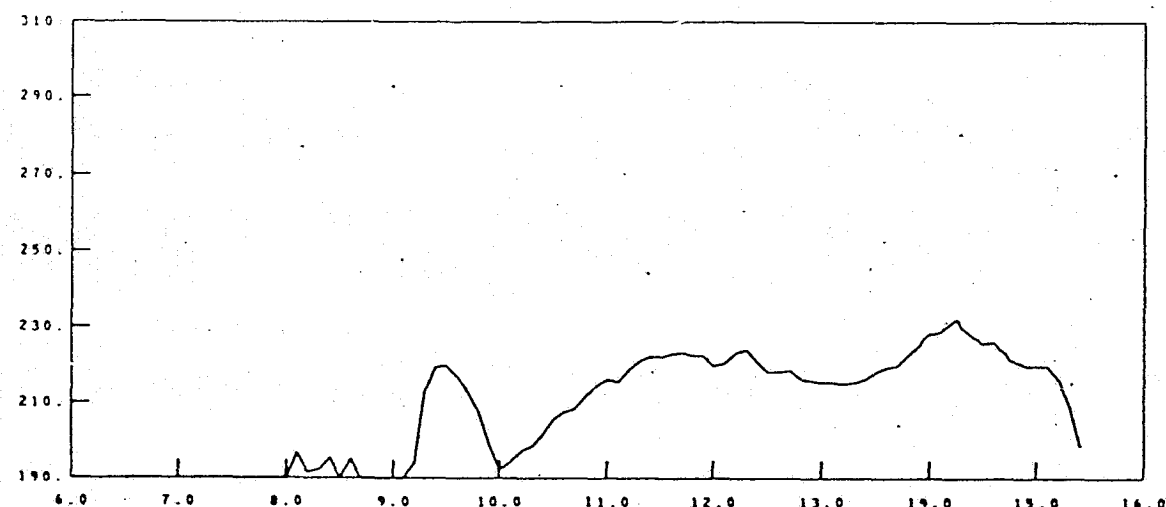


A6-13

A6-14



S191 DATA 32

MM DD YY
9 12 73HH MM SS
17 5 10SUN ZENITH ANGLE
0.0LATITUDE
26.99LONGITUDE
90.58

A6-15

S191 DATA 38

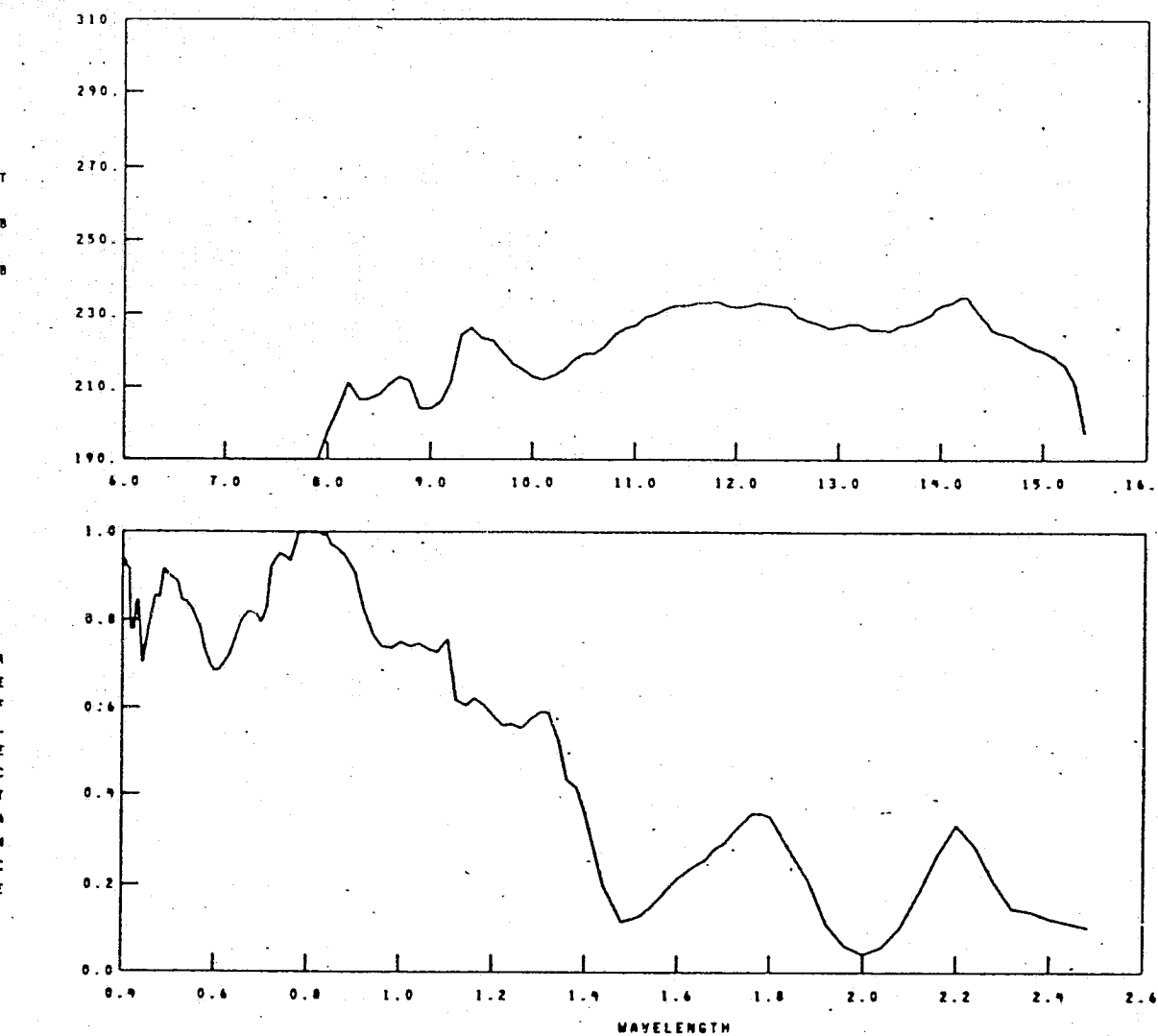
MM DD YY
9 12 73

HH MM SS
17 5 16

SUN ZENITH ANGLE
0.0

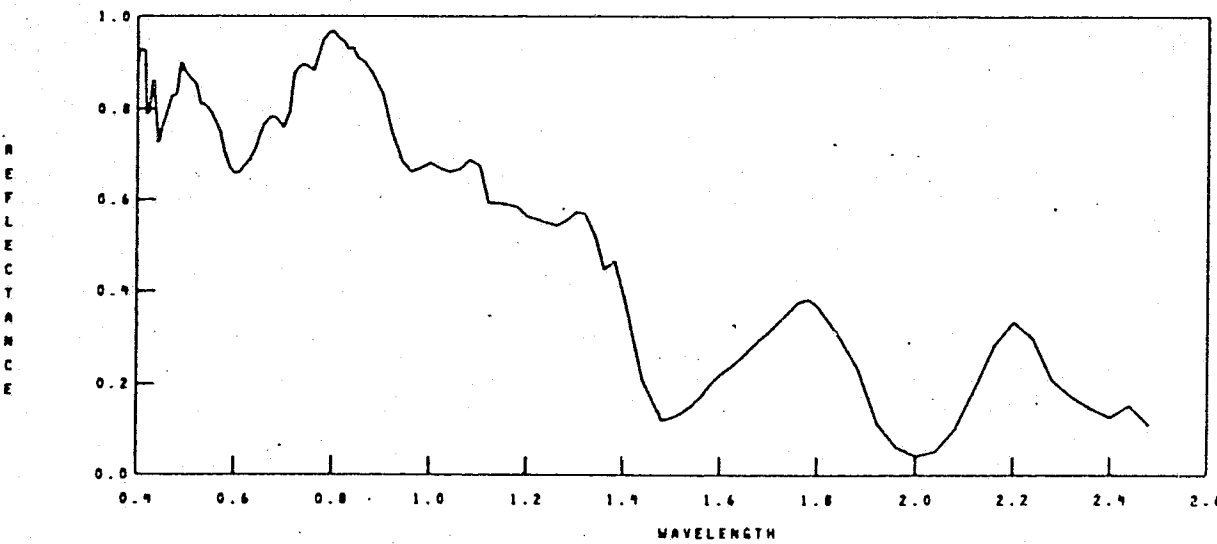
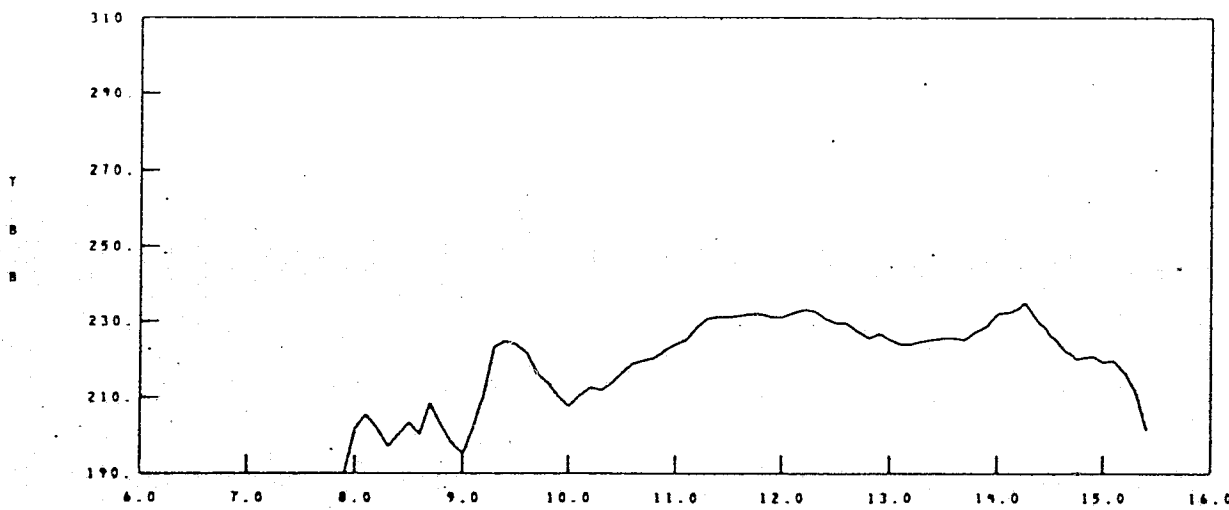
LATITUDE
27.24

LONGITUDE
90.32



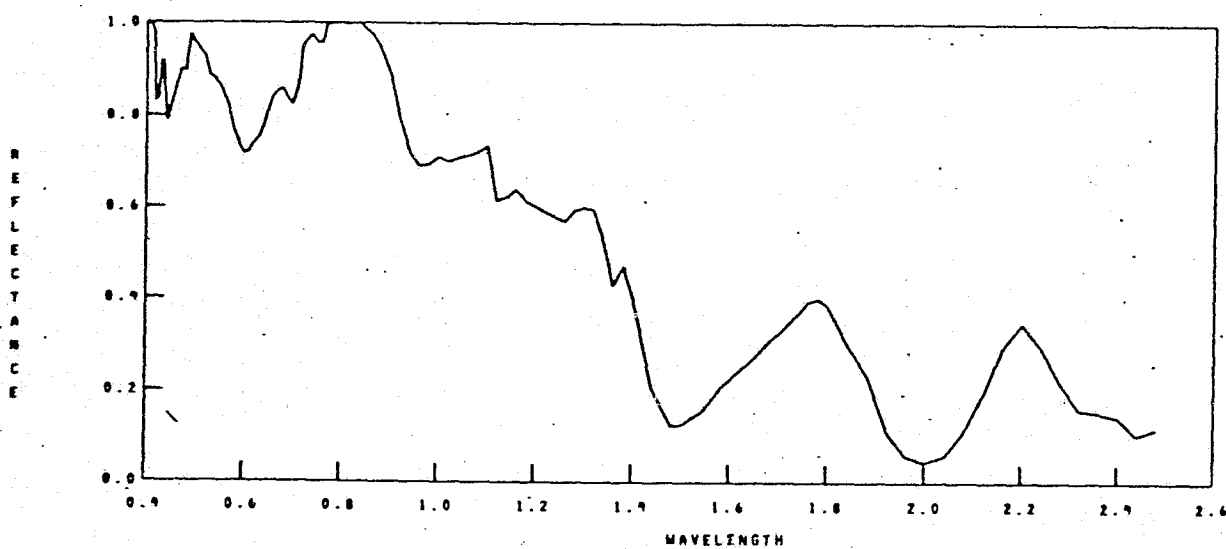
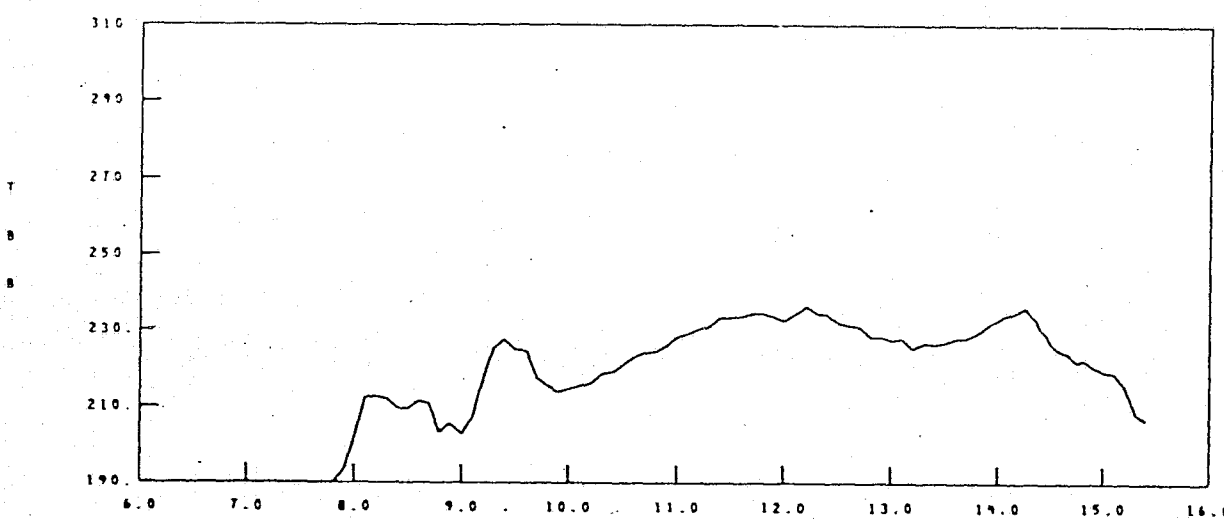
A6-16

S191 DATA 44

MM DD YY
9 12 73HH MM SS
17 5 21SUN ZENITH ANGLE
0 0LATITUDE
27.99LONGITUDE
90.04

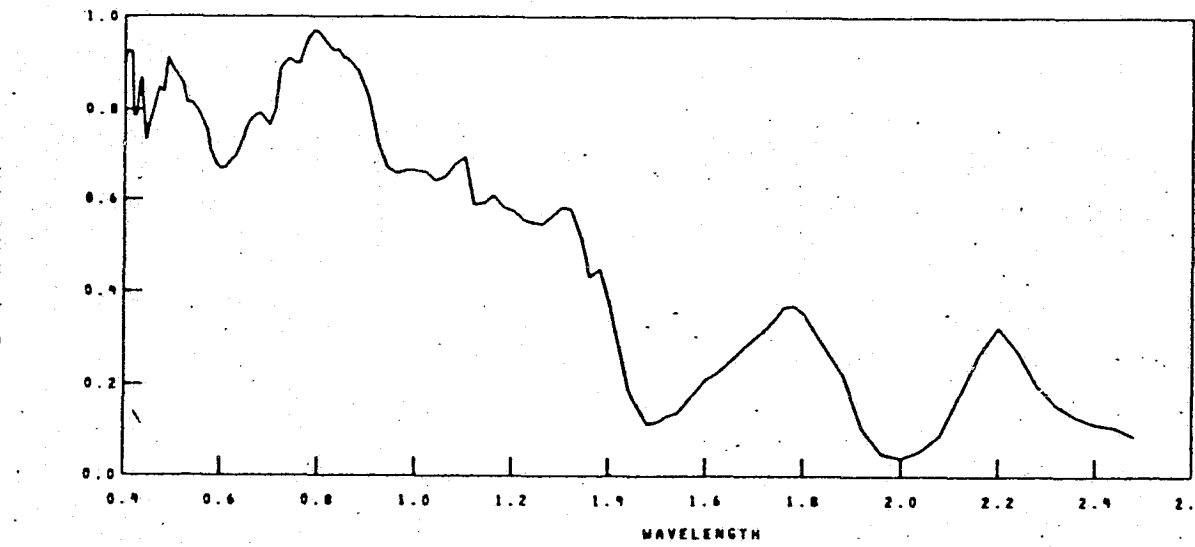
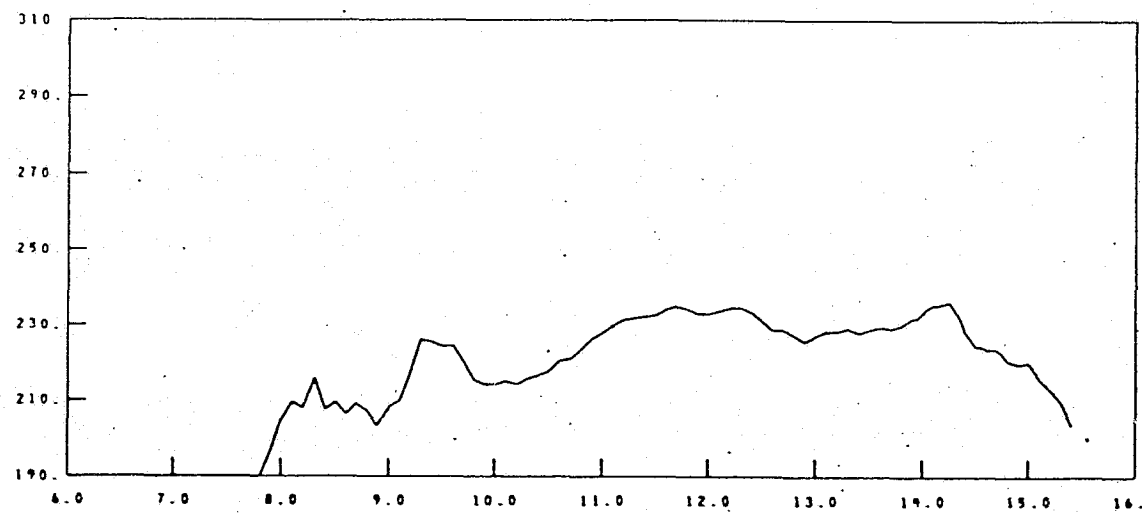
A6-17

S191 DATA -50

MM DD YY
9 12 73HH MM SS
17 3 27SUN ZENITH ANGLE
0.0LATITUDE
27.74LONGITUDE
87.78

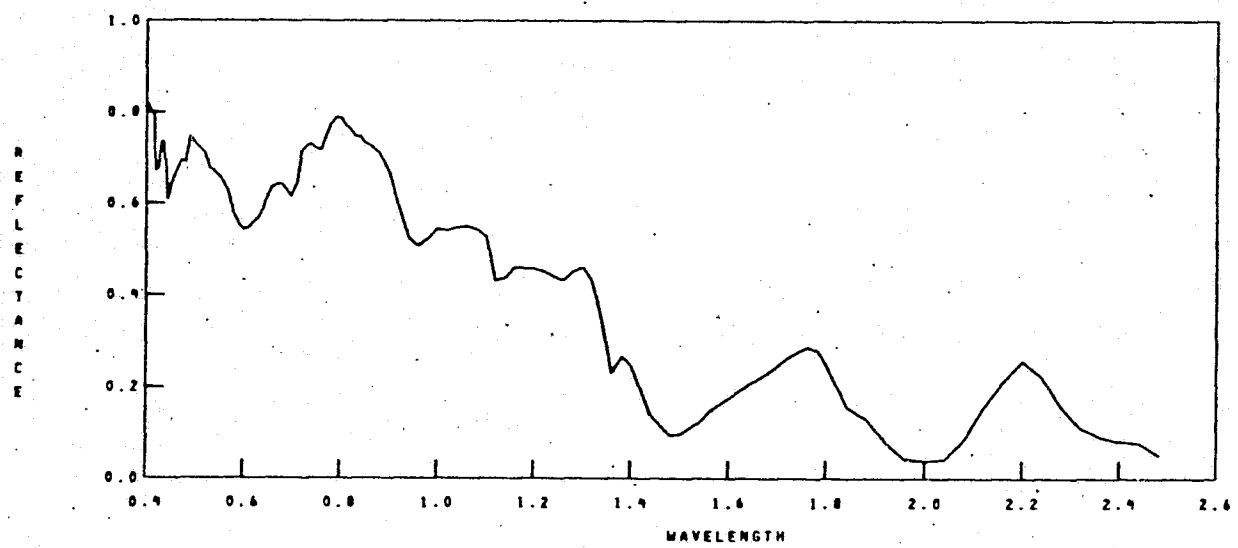
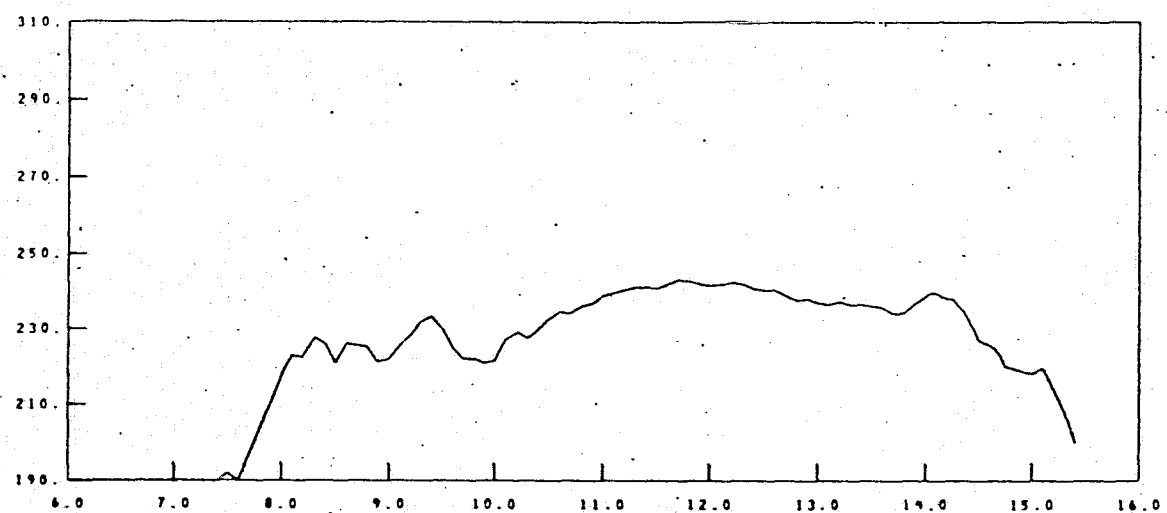
A6-18

S191 DATA 56

MM DD YY
9 12 73HH MM SS
17 5 32SUN ZENITH ANGLE
0.0LATITUDE
27.99LONGITUDE
89.50

A6-19

S191 DATA 62

MM DD YY
9 12 73HH MM SS
17 5 38SUN ZENITH ANGLE
0.0LATITUDE
28.29LONGITUDE
89.23

S191 DATA 68

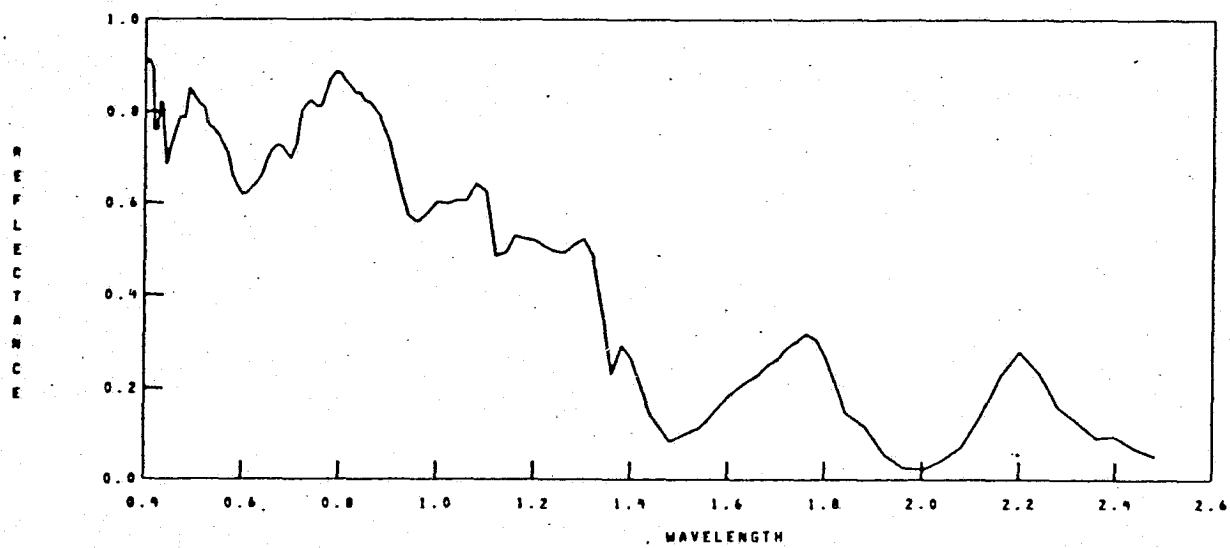
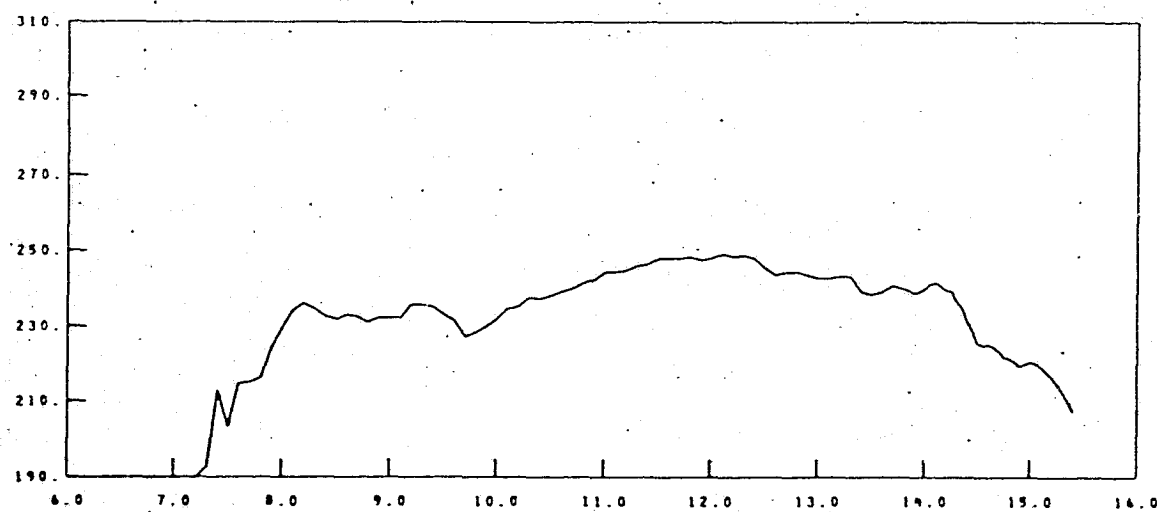
MM DD YY
9 12 73

HH MM SS
17 5 43

SUN ZENITH ANGLE
0.0

LATITUDE
28.98

LONGITUDE
88.95



A6-21

S191 DATA 74

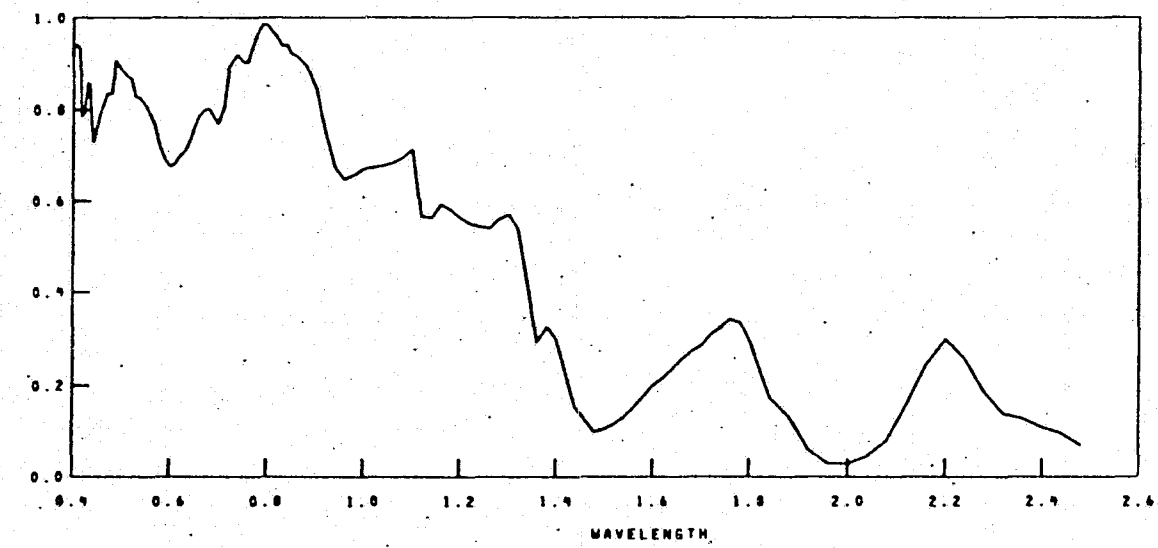
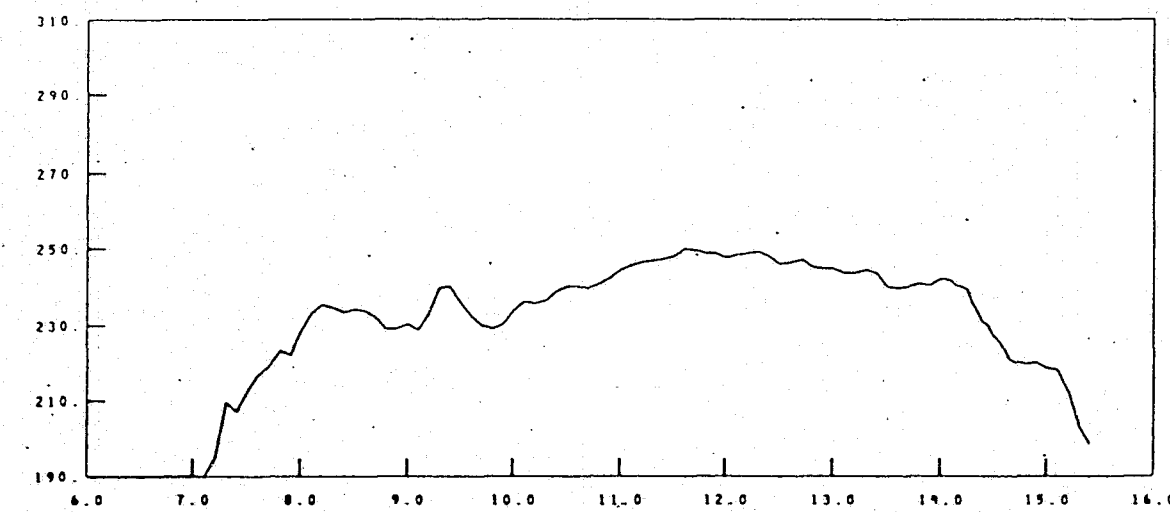
MM DD YY
9 12 73

HH MM SS
17 5 51

SUN ZENITH ANGLE
0 0

LATITUDE
28.81

LONGITUDE
68.58



A6-22

S191 DATA 80

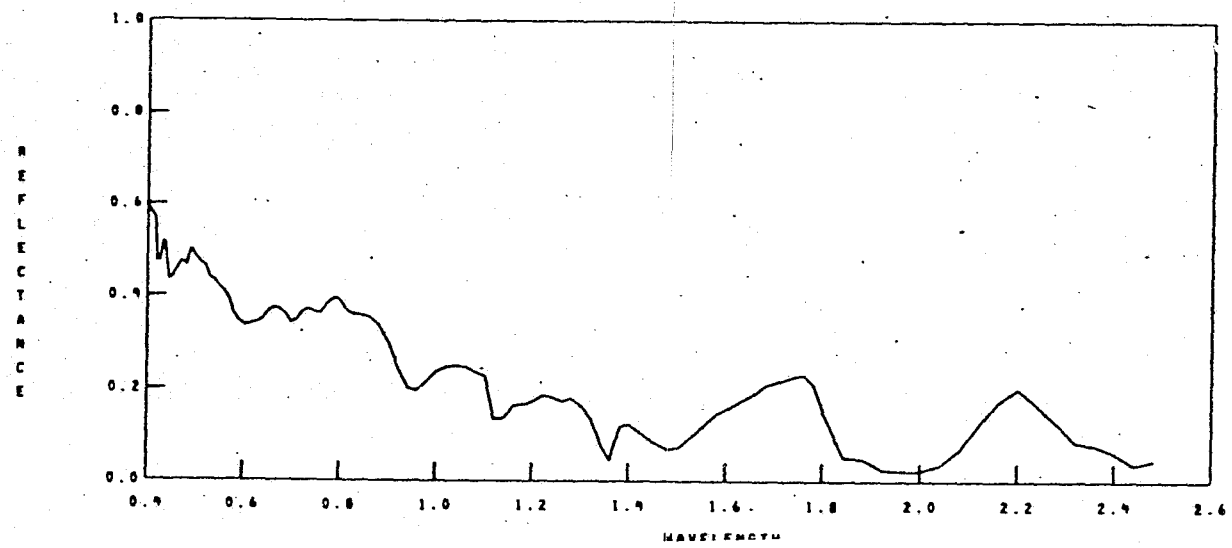
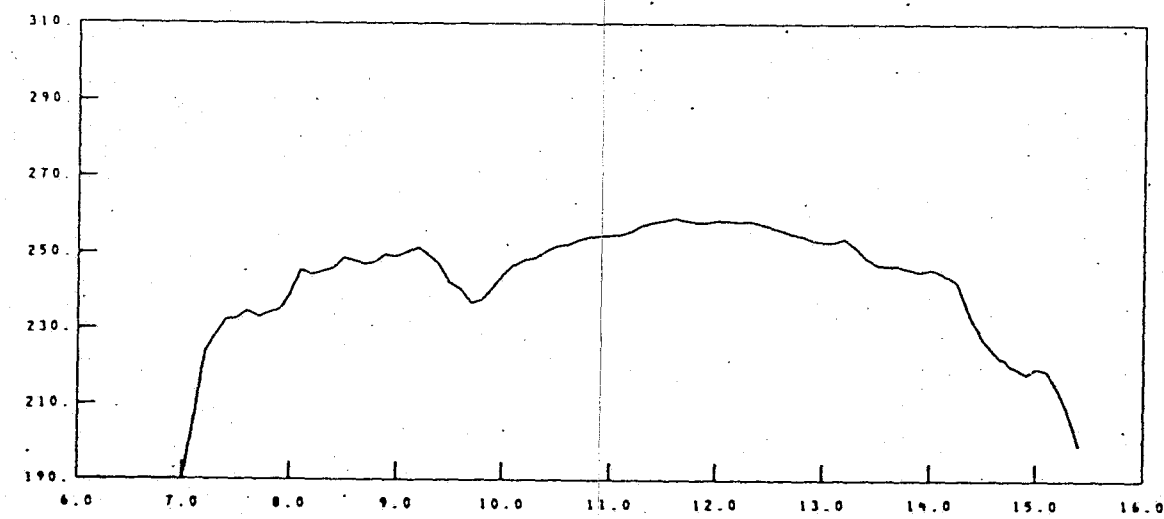
MM DD YY
9 12 73

HH MM SS
17 5 57

SUN ZENITH ANGLE
0.0

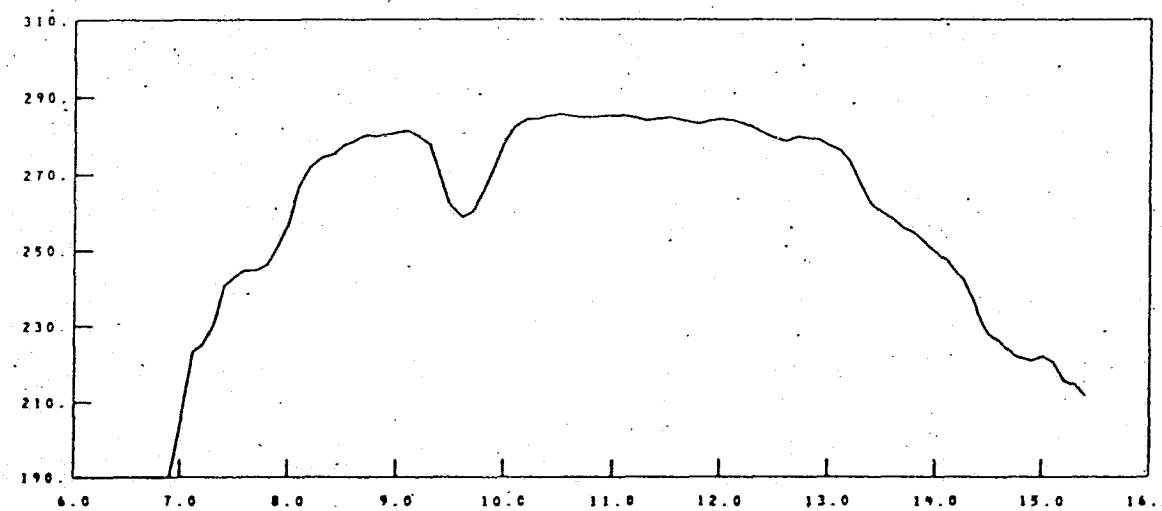
LATITUDE
29.06

LONGITUDE
88.31

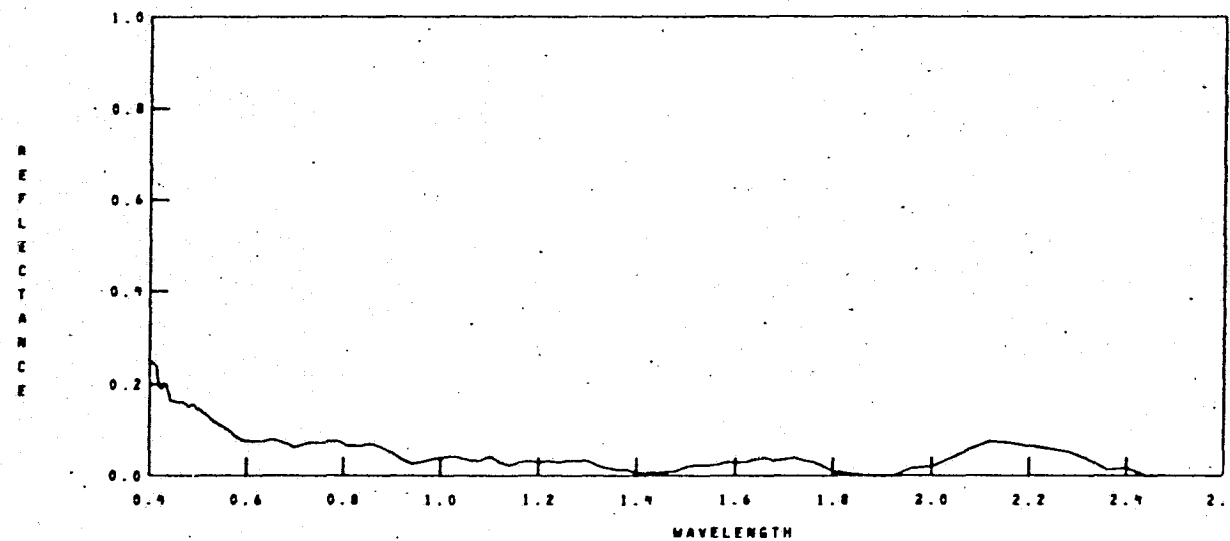


A6-23

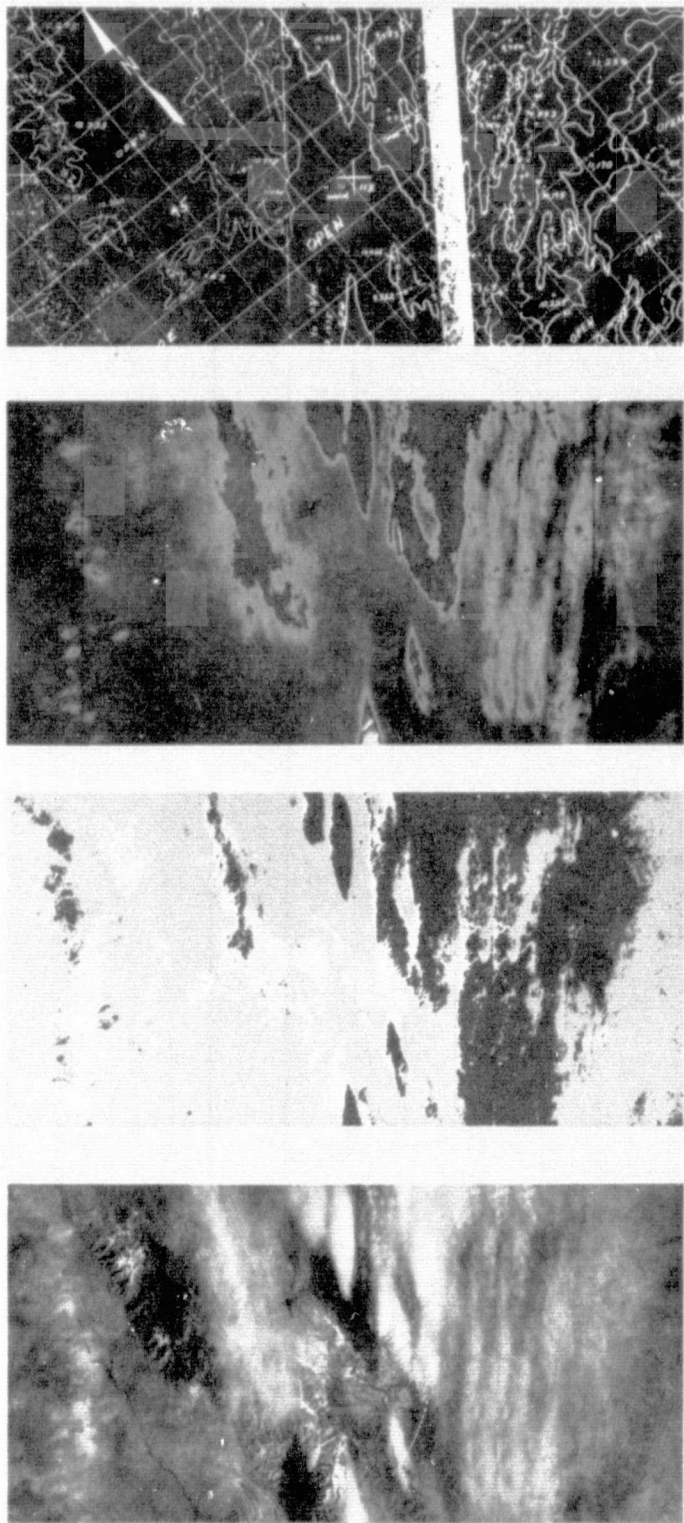
S191 DATA 84

MM DD YY
9 12 73HH MM SS
17 6 0SUN ZENITH ANGLE
0 0LATITUDE
29.22LONGITUDE
86.12

A6-24



DAY 335
1973



ORIGINAL PAGE IS
OF POOR QUALITY

A6-25

S191 DATA 24

MM DD YY

12 17 77

HH MM SS

17 27 48

SUN ZENITH ANGLE

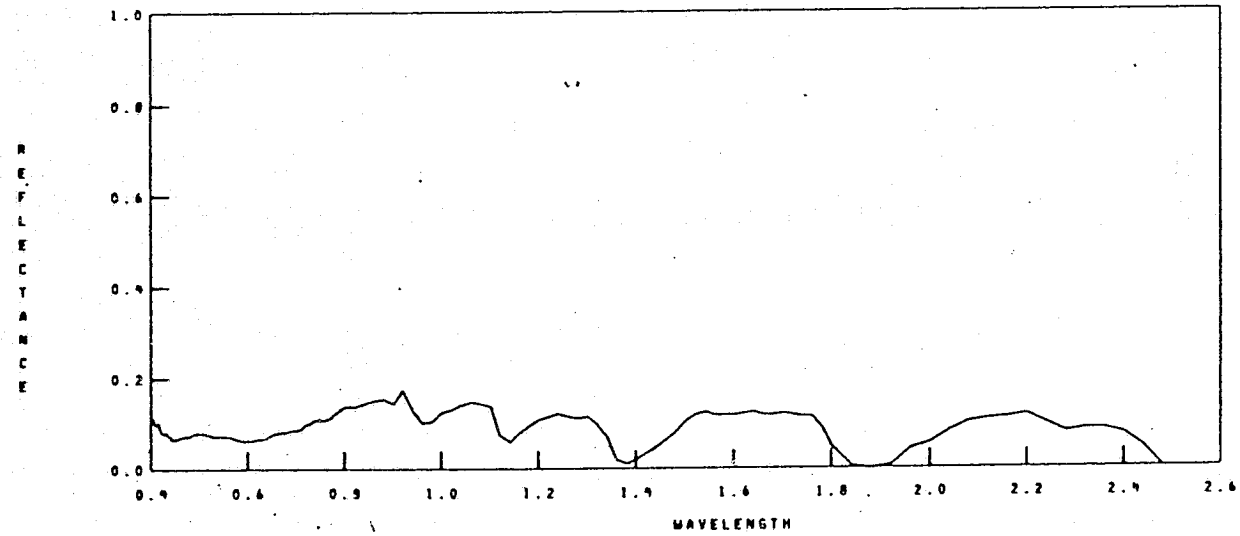
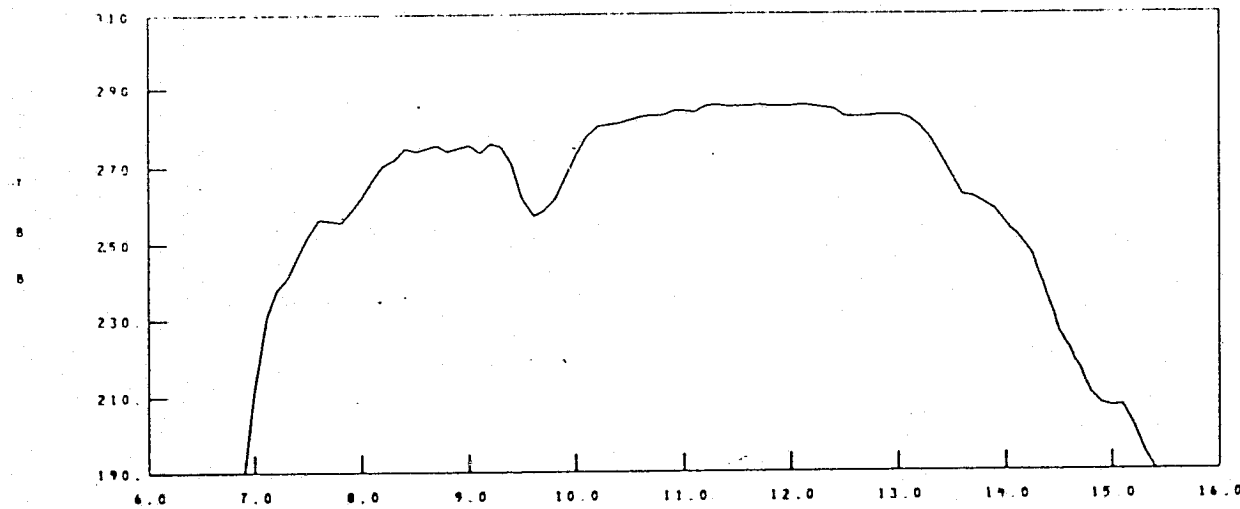
0 0

LATITUDE

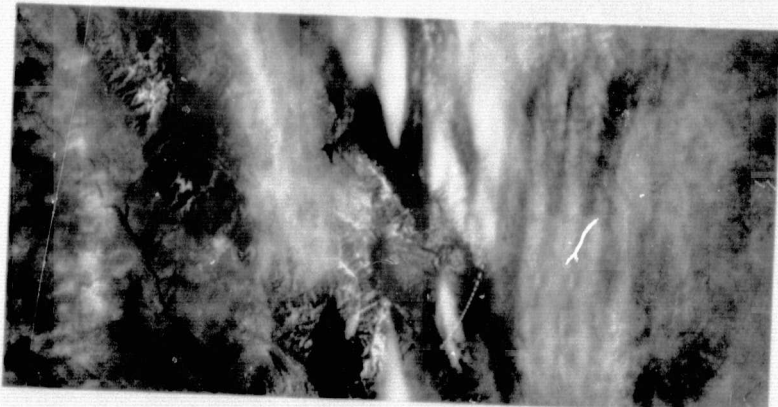
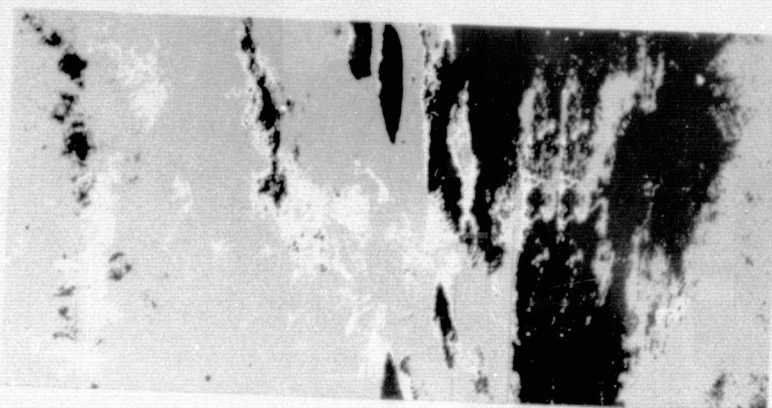
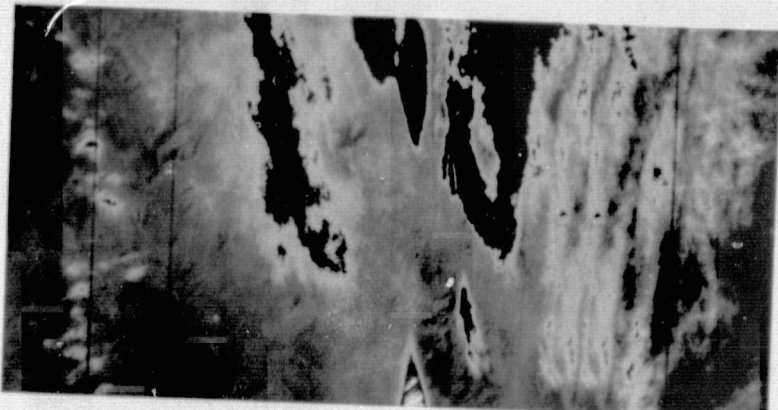
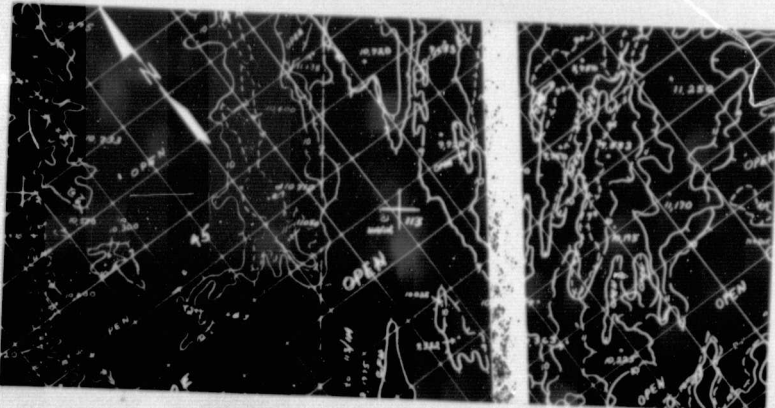
36.98

LONGITUDE

616

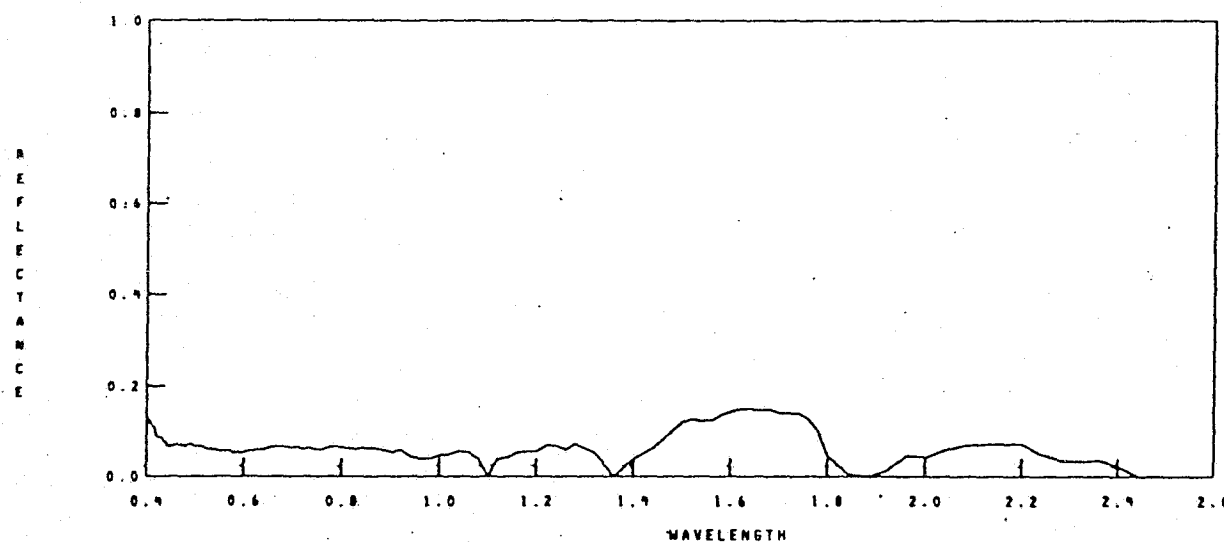
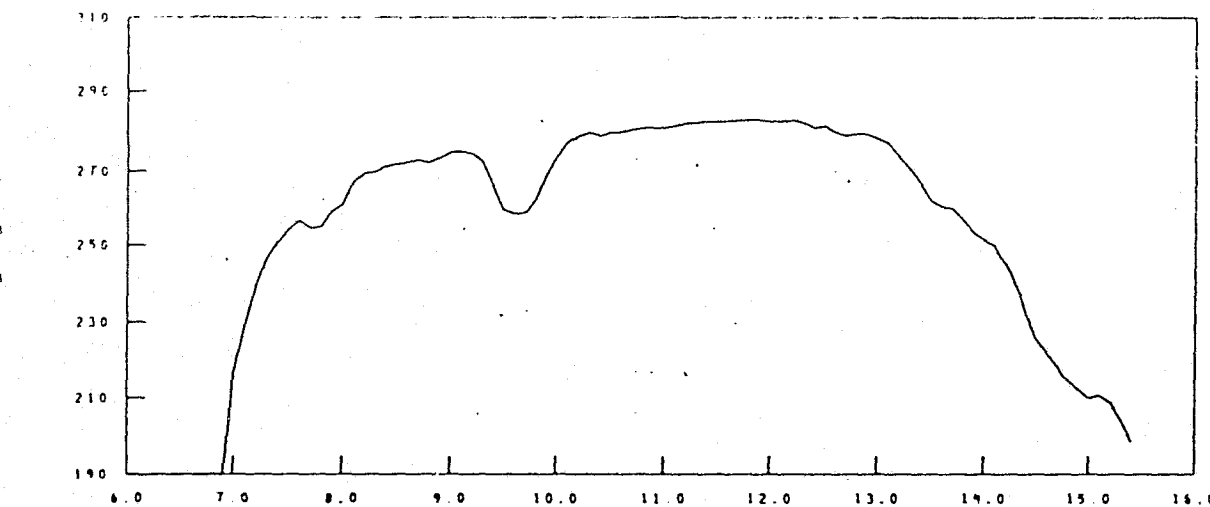


DAY 335
1973



A6-26a

S191 DATA 28

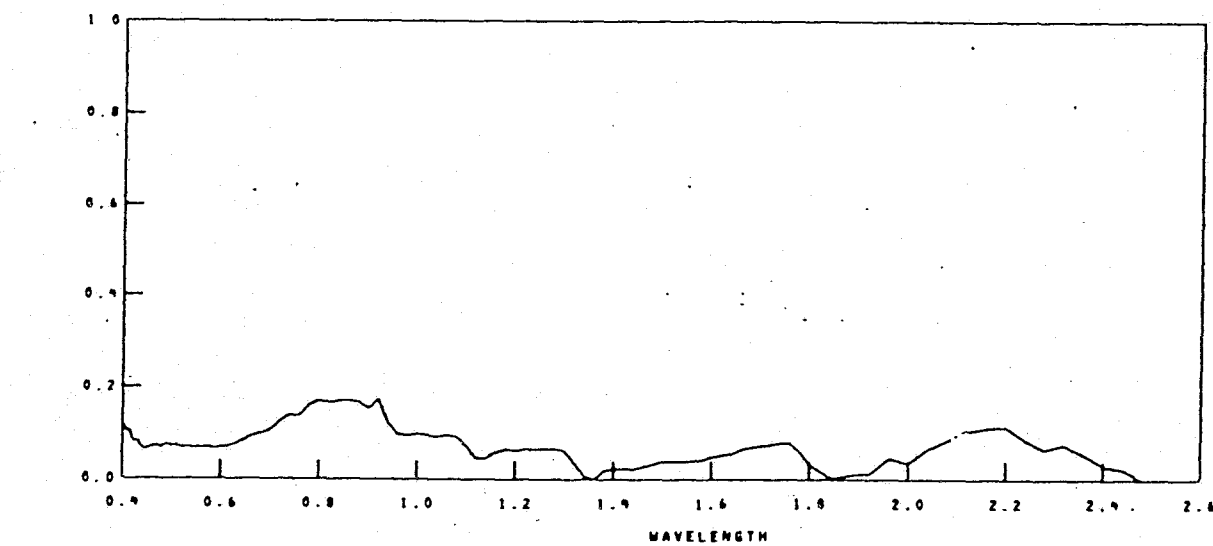
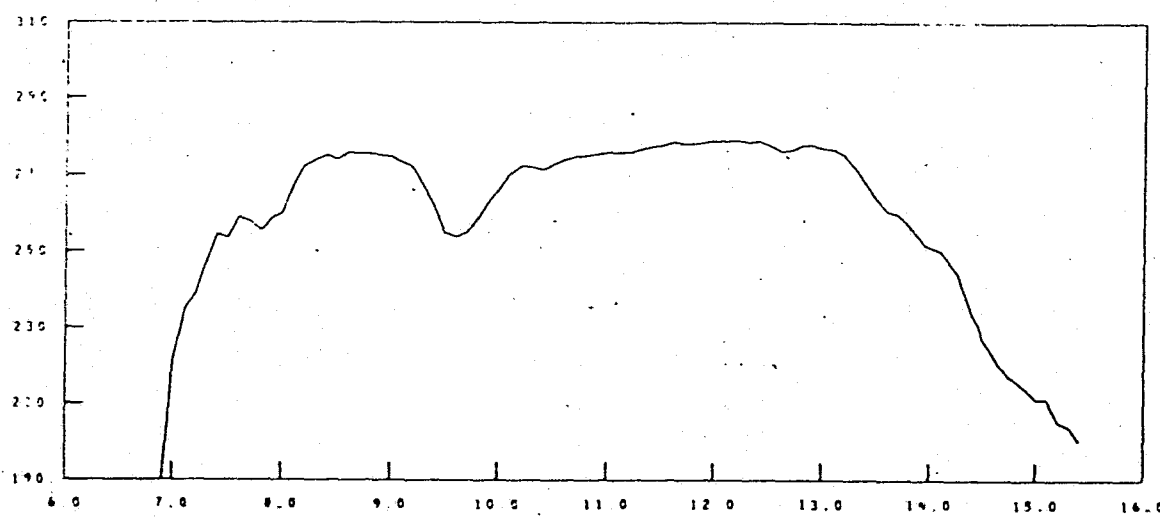
MM DD YY
12 17 73HH MM SS
17 27 11SUN ZENITH ANGLE
0 0LATITUDE
36 84
LONGITUDE
5 93

A6-27

S191 DATA 32

PP DD YY HH MM SS SUN ZENITH ANGLE LATITUDE LONGITUDE

12 17 72 17 27 15 0.0 36 69 5 71



A6-28

S191 DATA 76

MM DD YY

HH MM SS

SUN ZENITH ANGLE

LATITUDE

LONGITUDE

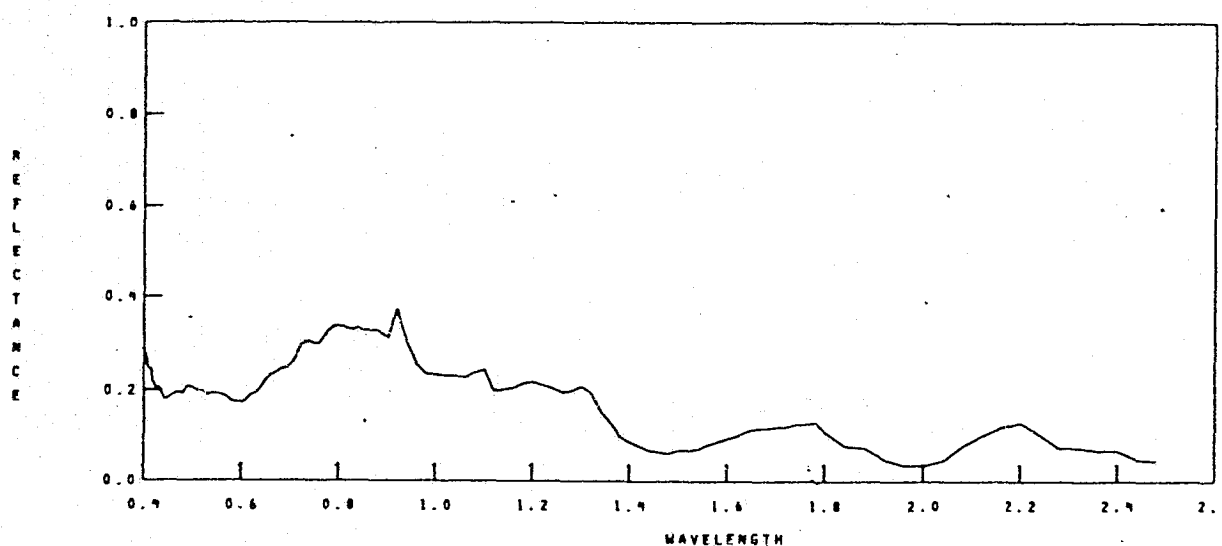
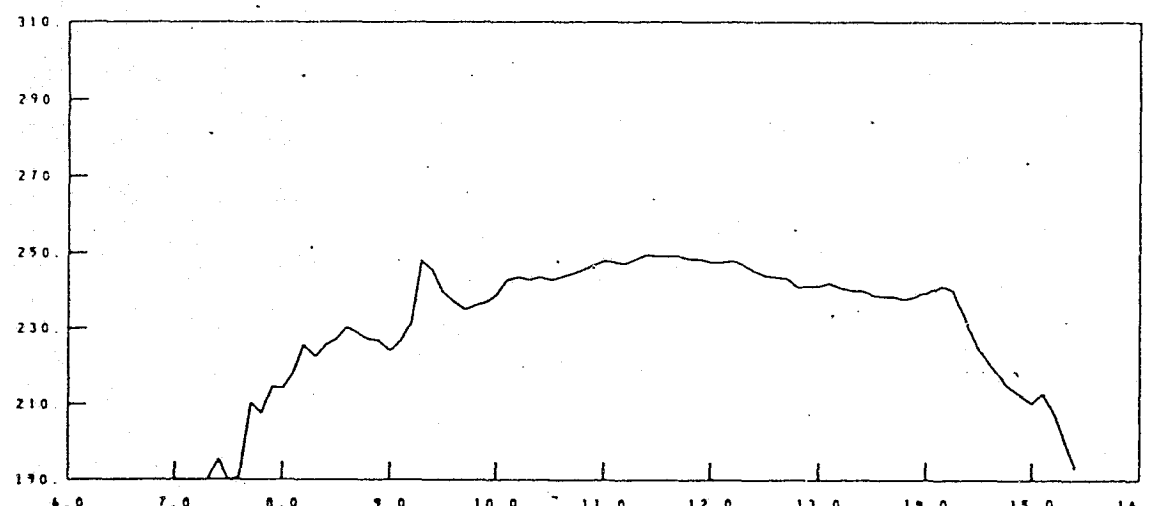
12 173

17 27 19

0.0

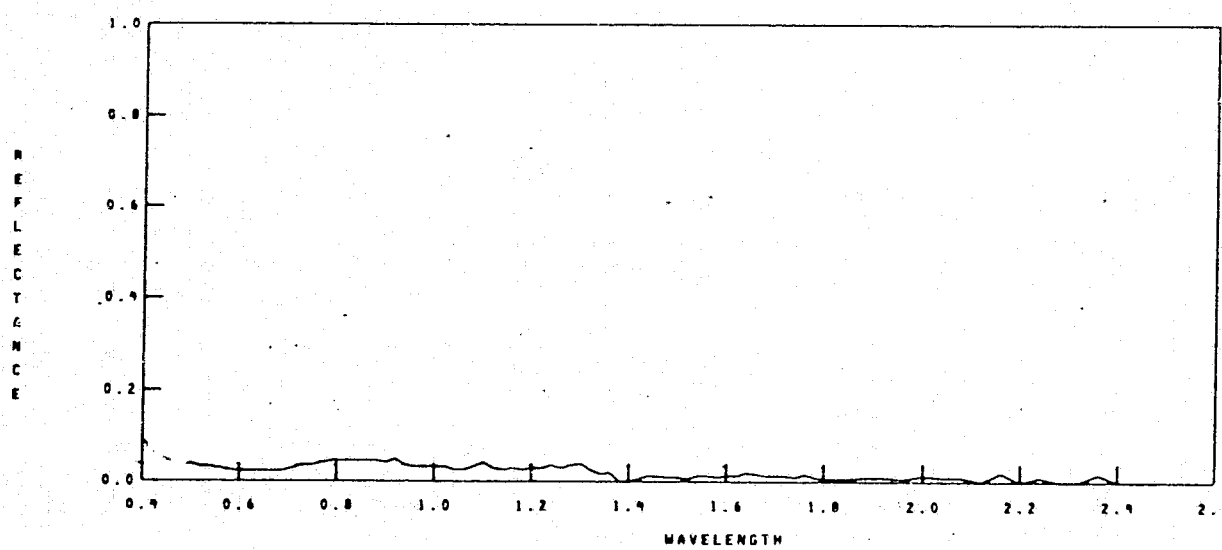
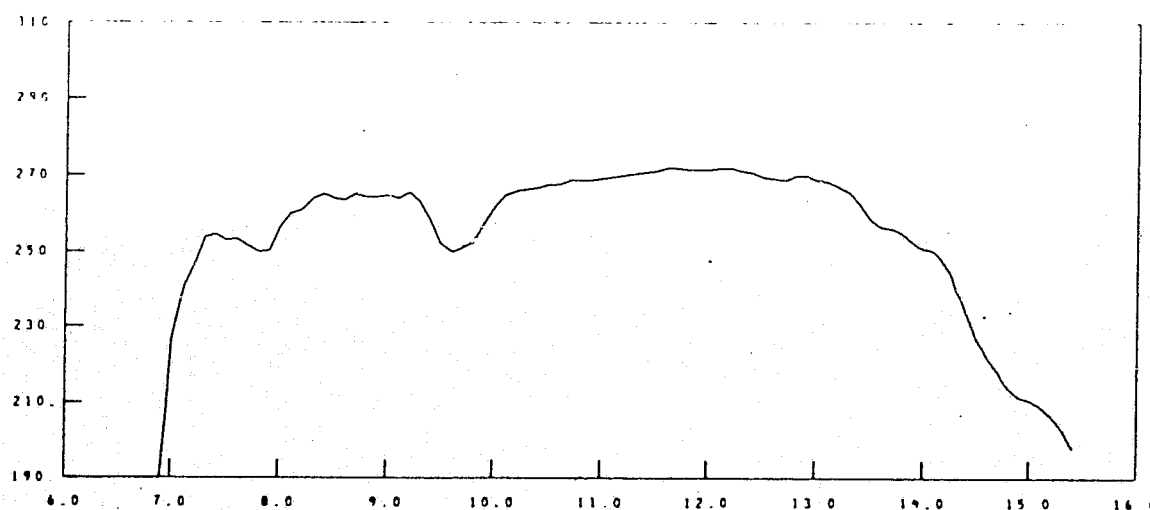
36.55

5 49



A6-29

S191 DATA NO

MM DD YY
12 17 73HH MM SS
17 27 21SUN ZENITH ANGLE
0 0LATITUDE
36 46LONGITUDE
5 27

A6-30

C191 DATA 24

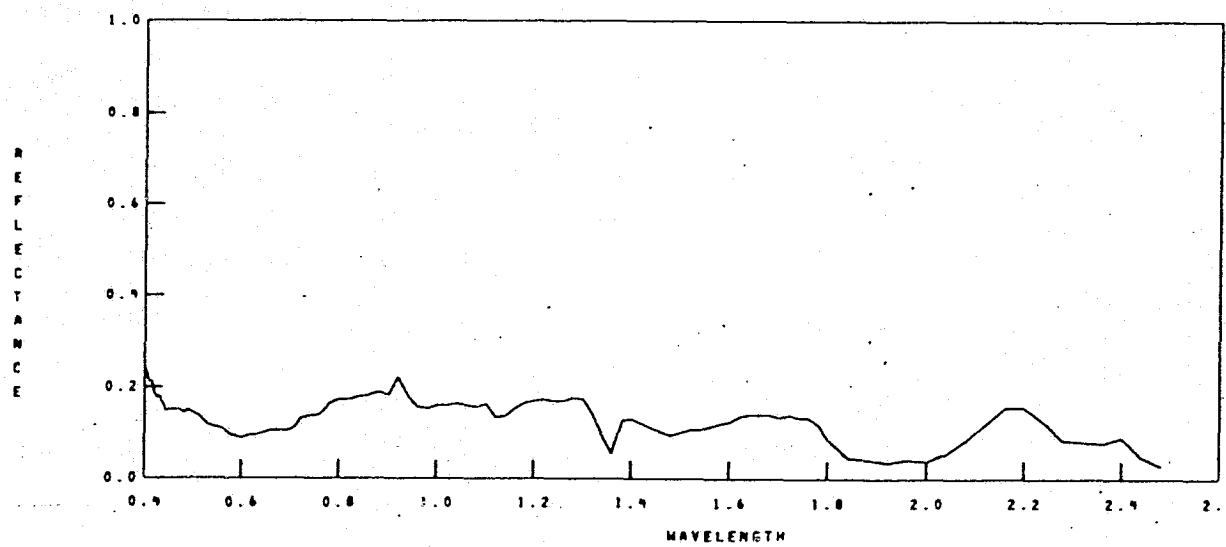
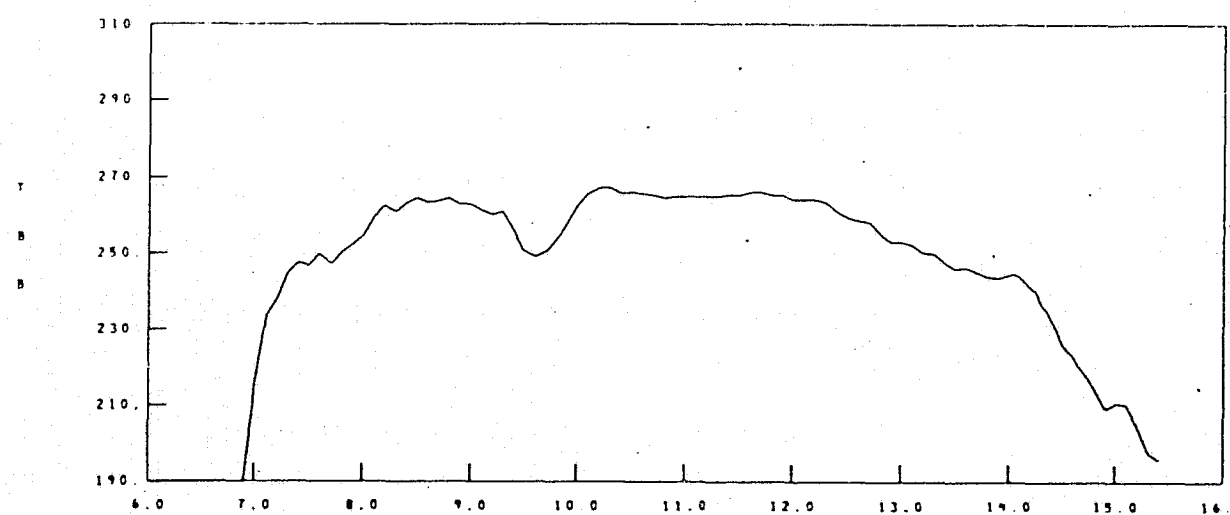
MM DD YY
12 17 73

HH MM SS
17 27 26

SUN ZENITH ANGLE
0.0

LATITUDE
36 26

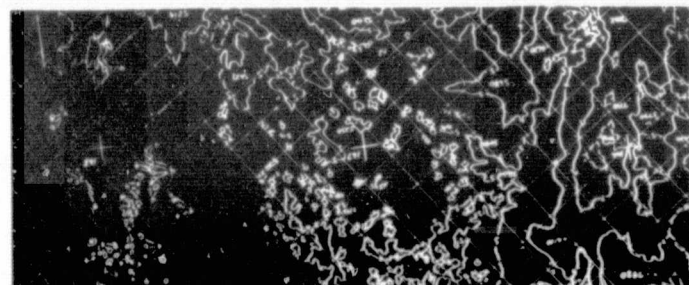
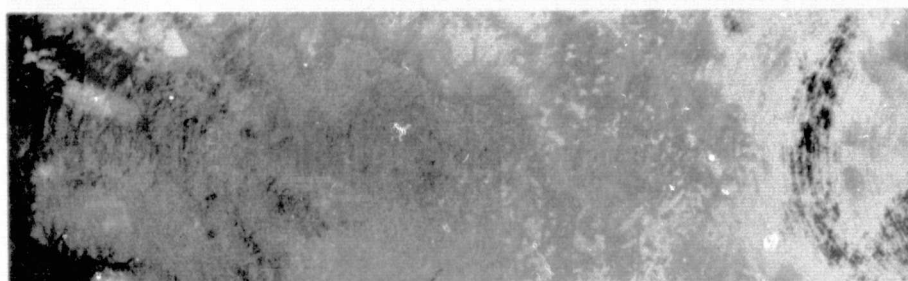
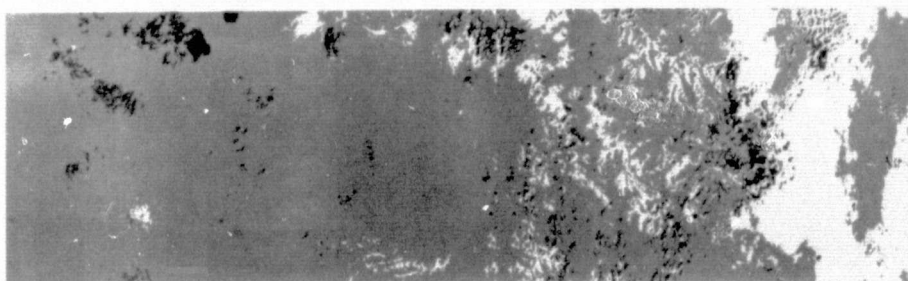
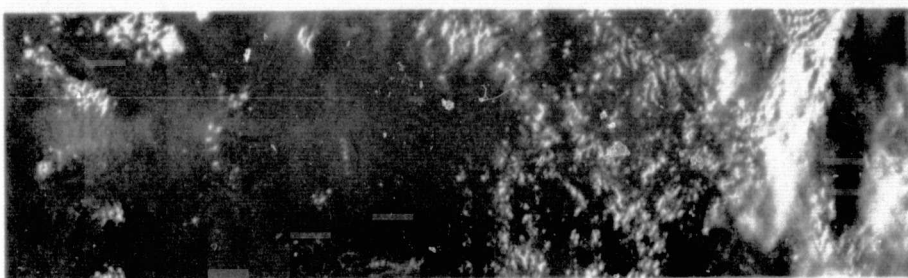
LONGITUDE
5 05



A6-31

DAY 336

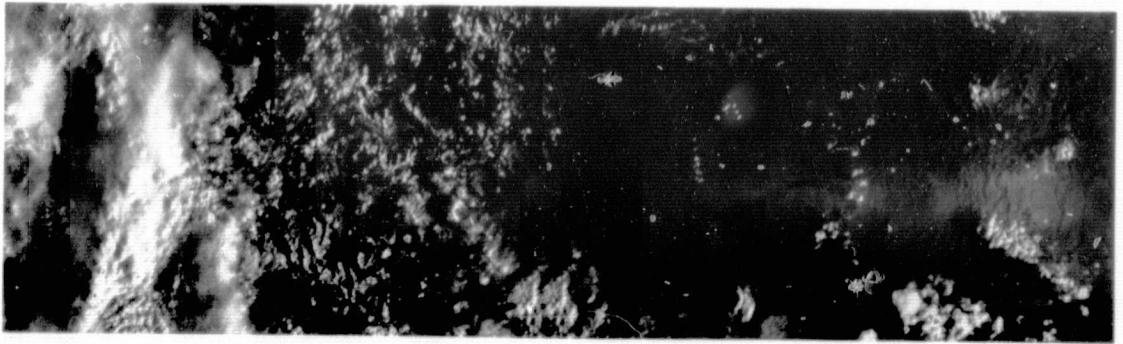
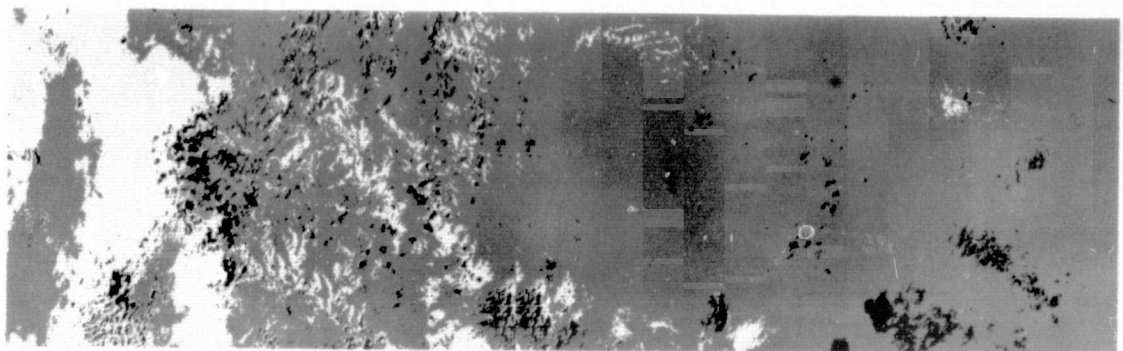
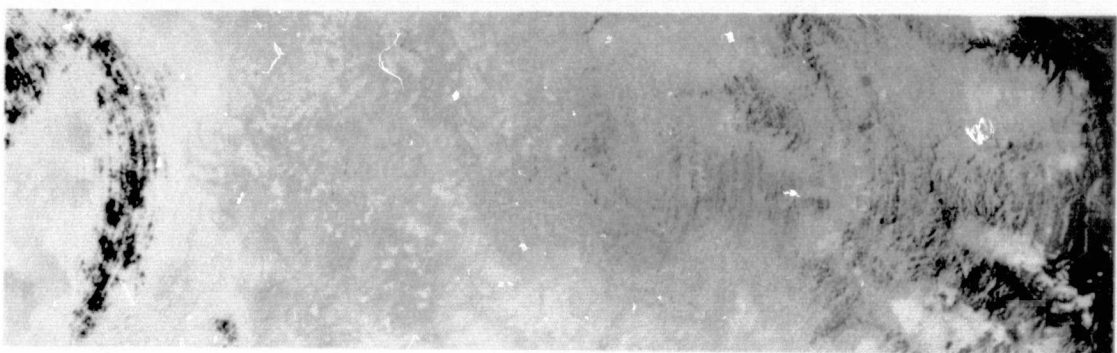
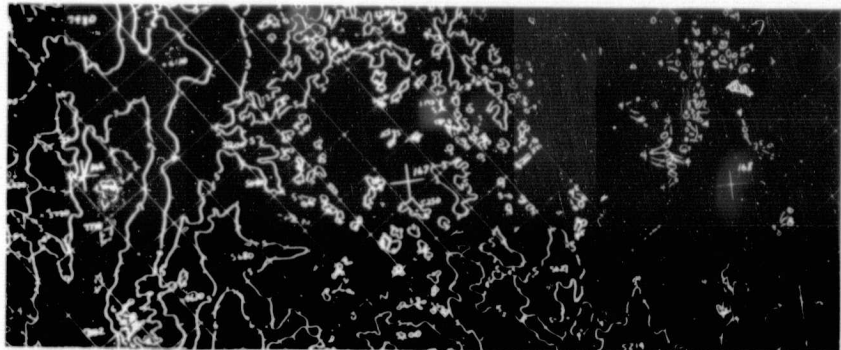
1973



ORIGINAL PAGE IS
OF POOR QUALITY

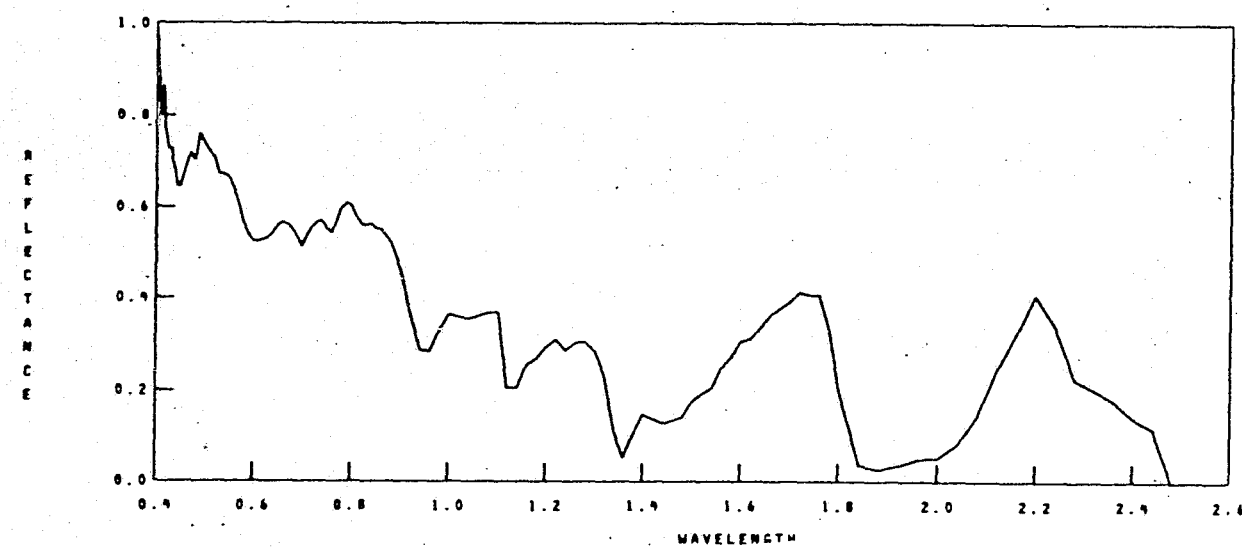
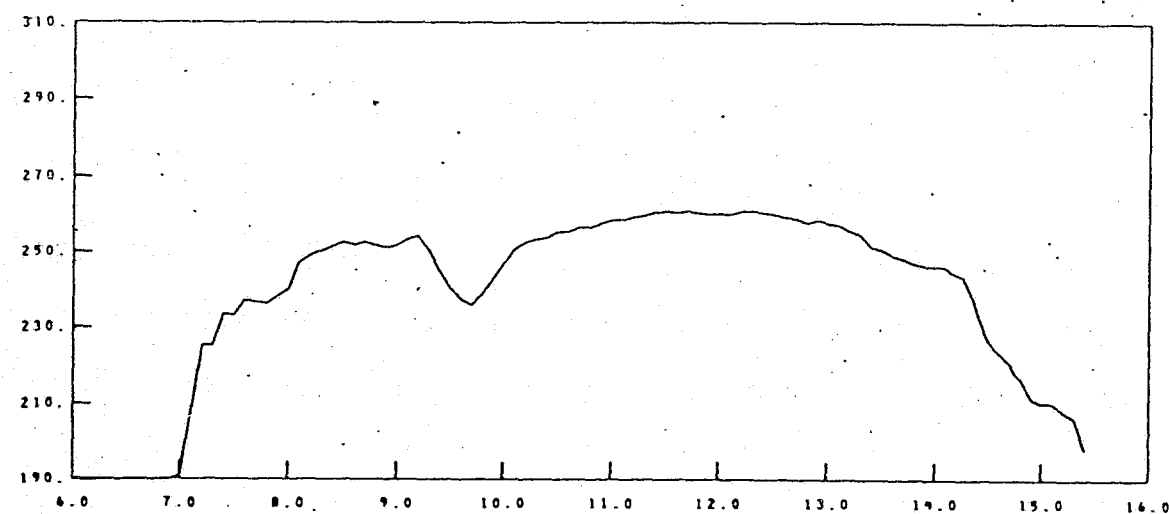
A6-32

DAY 336
1973



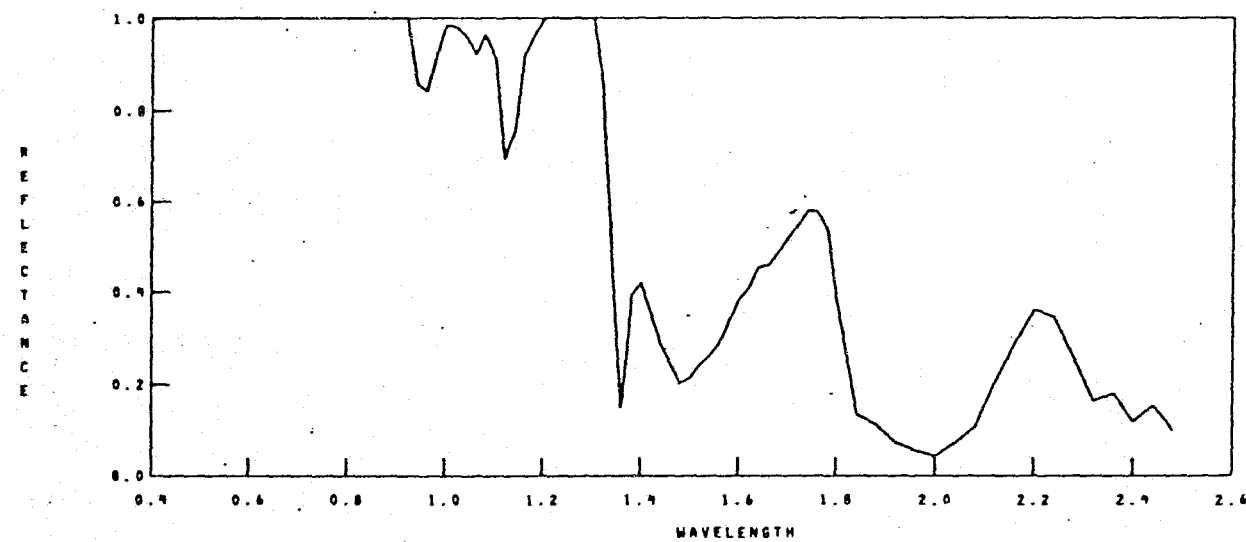
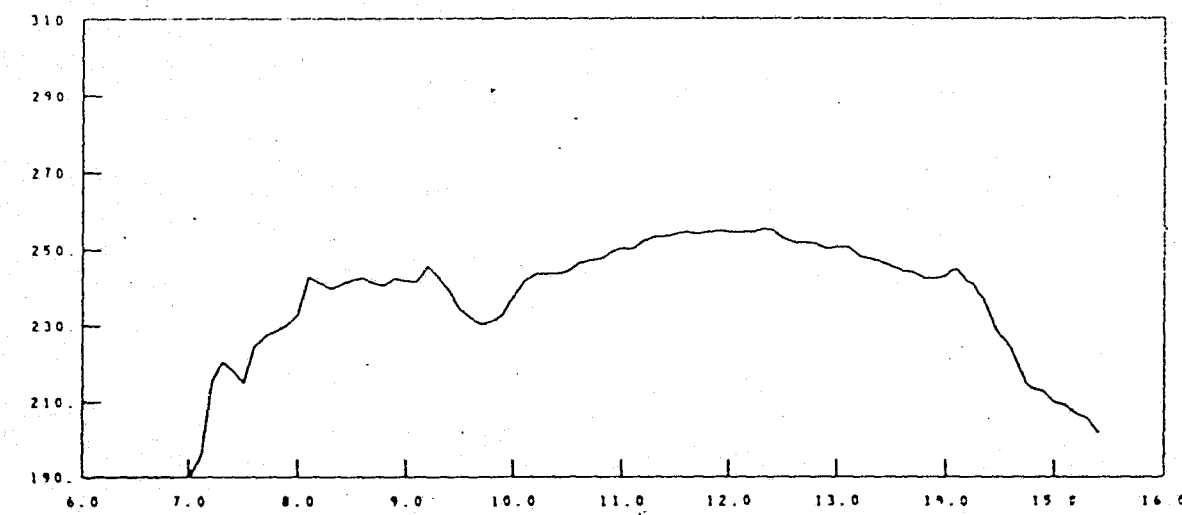
A6-32a

S191 DATA 12

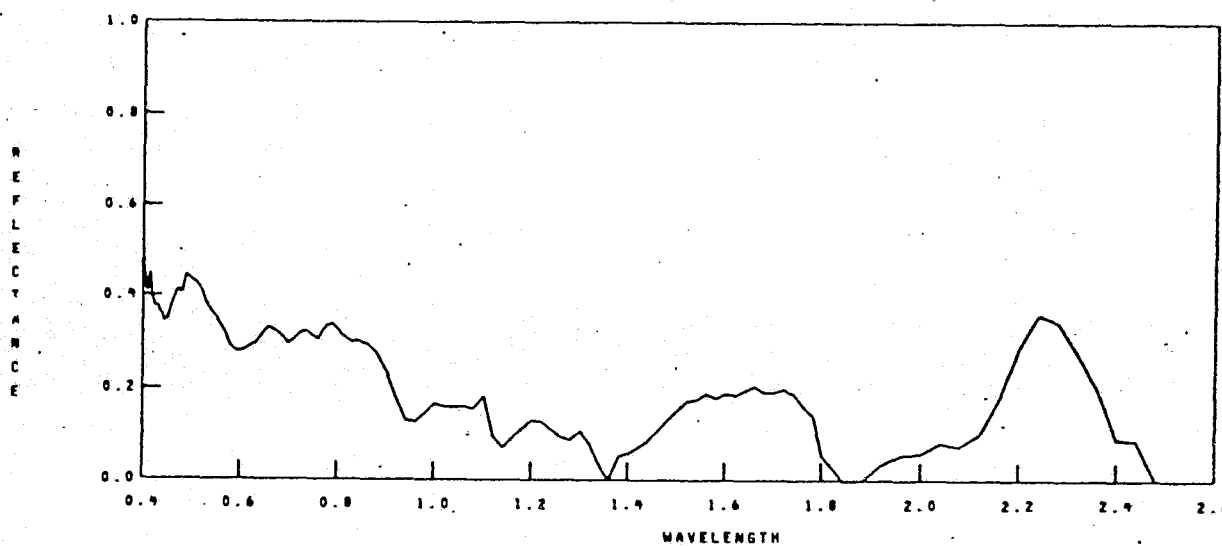
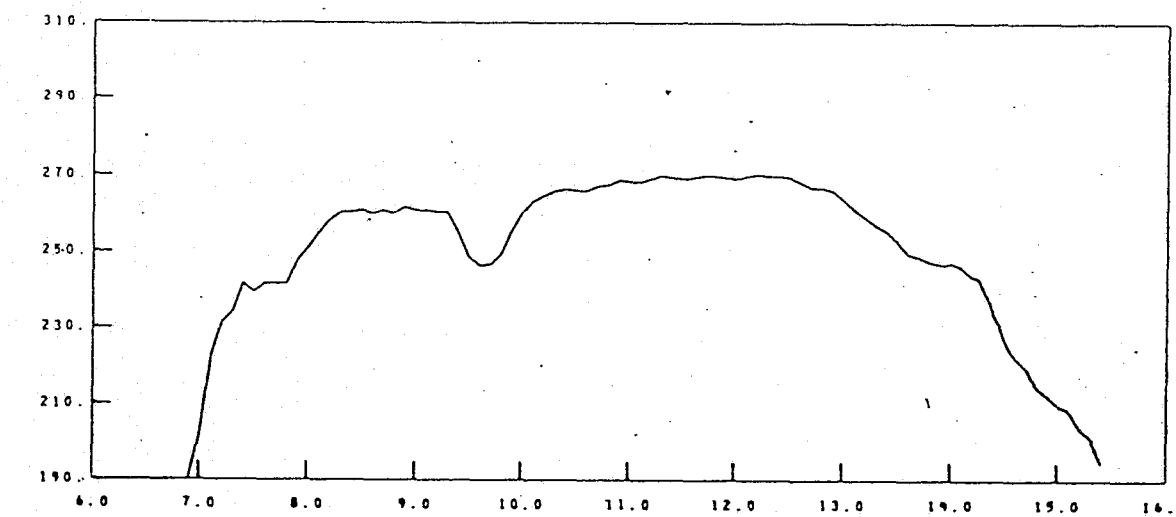
MM DD YY
12 273HH MM SS
16 43 9SUN ZENITH ANGLE
69.5LATITUDE
90.18LONGITUDE
6.89

A6-33

S191 DATA 16

MM DD YY
12 273HH MM SS
16 43 12SUN ZENITH ANGLE
69.3LATITUDE
40.04LONGITUDE
6.69

SIRI DATA 20

MM DD YY
12 273HH MM SS
16 43 16SUN ZENITH ANGLE
69.1LATITUDE
39 91LONGITUDE
6 40

A6-35

S191 DATA 24

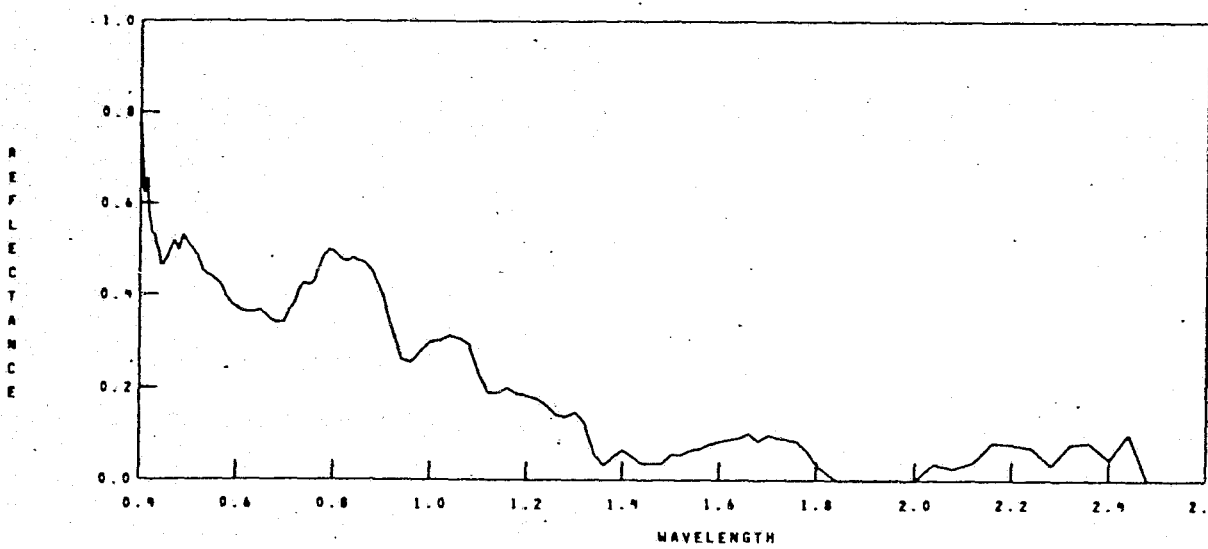
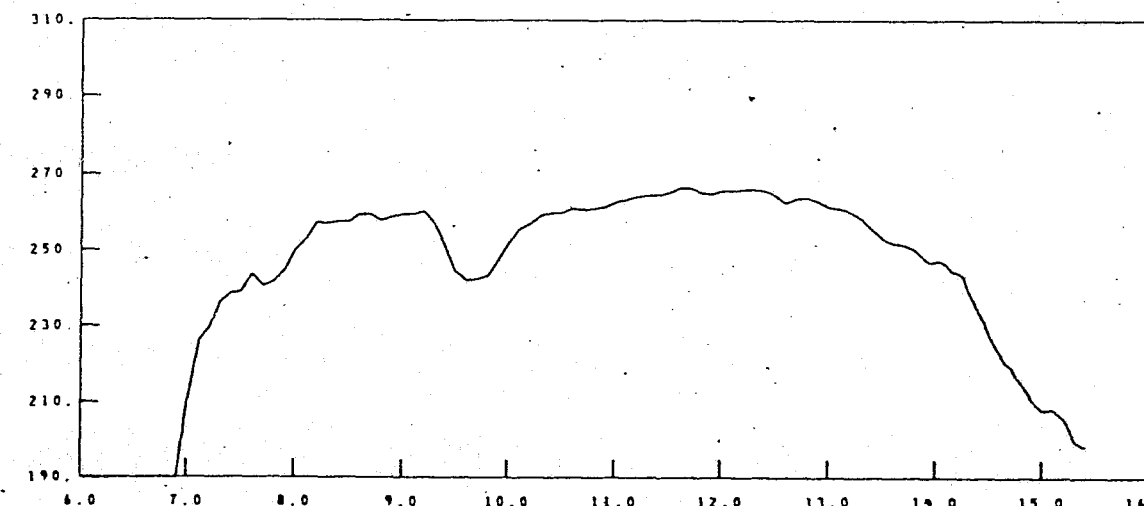
MM DD YY
12 273

HH MM SS
16 43 20

SUN ZENITH ANGLE
68.9

LATITUDE
39.78

LONGITUDE
6.16



A6-36

S191 DATA 20

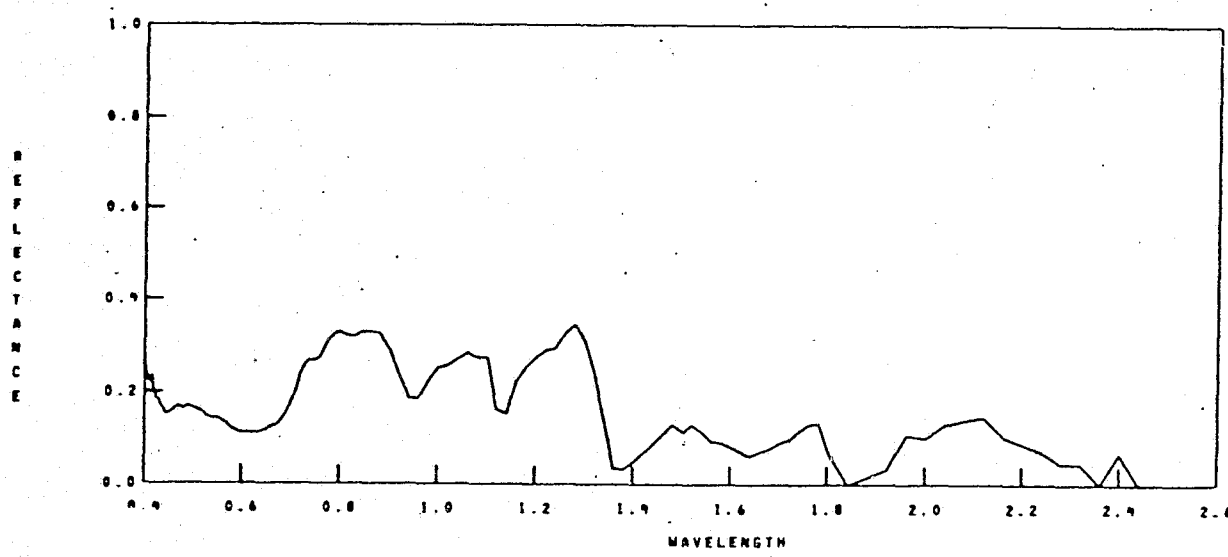
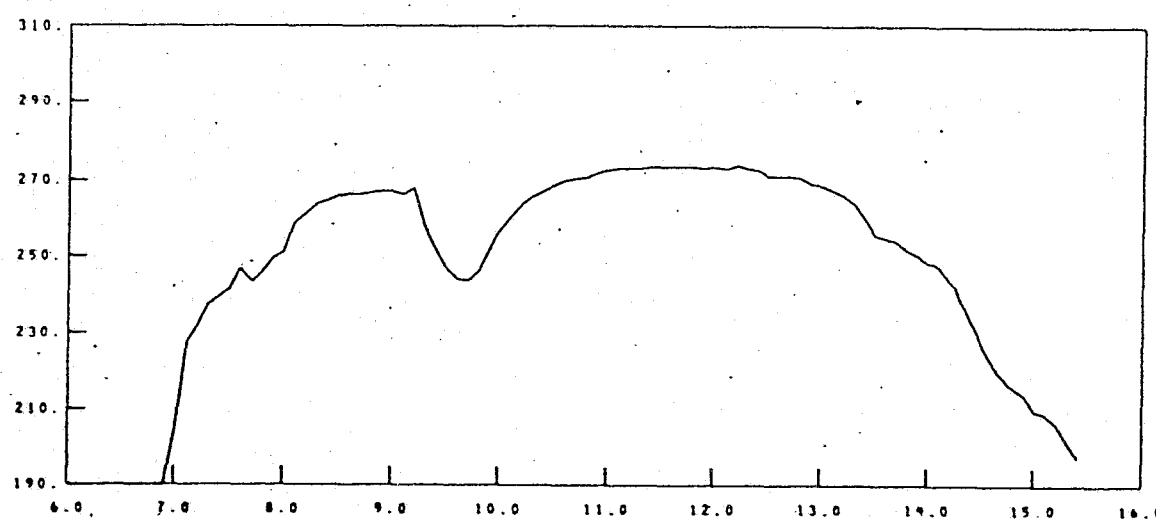
MM DD YY
12 27 73

HH MM SS
16 43 23

SUN ZENITH ANGLE
68.7

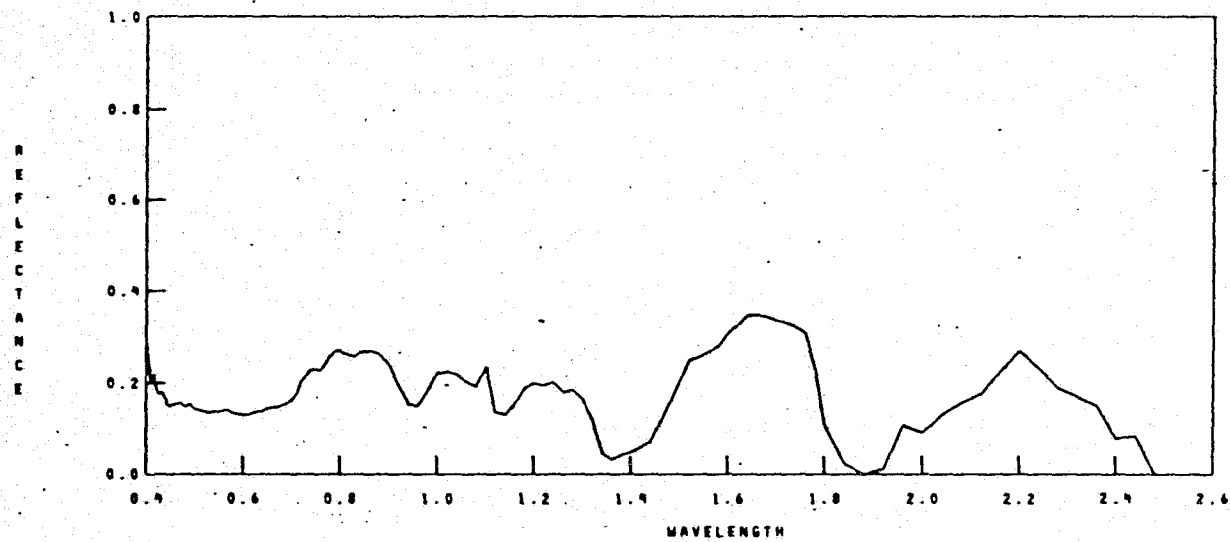
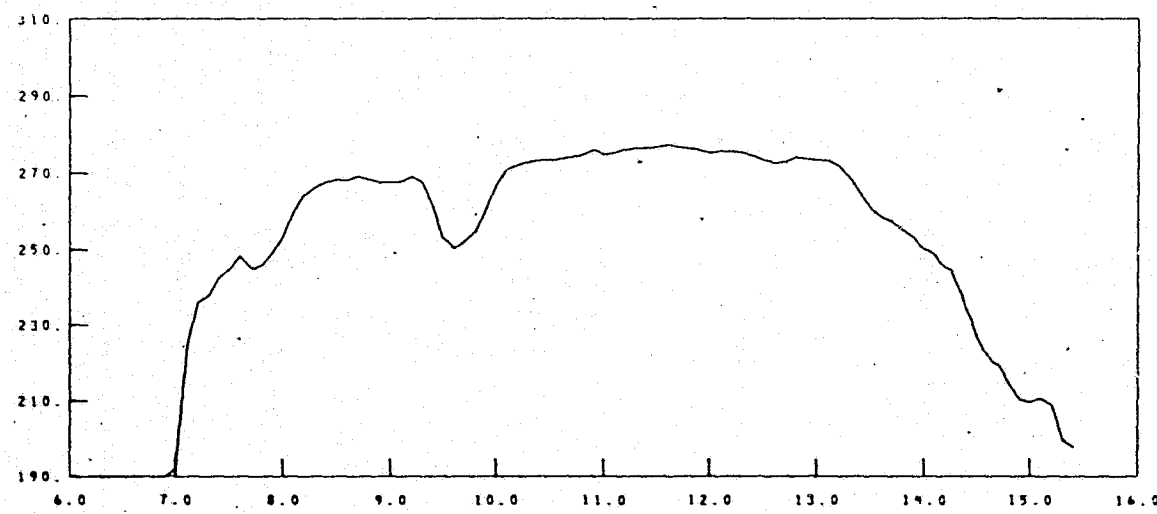
LATITUDE
39.65

LONGITUDE
5.92



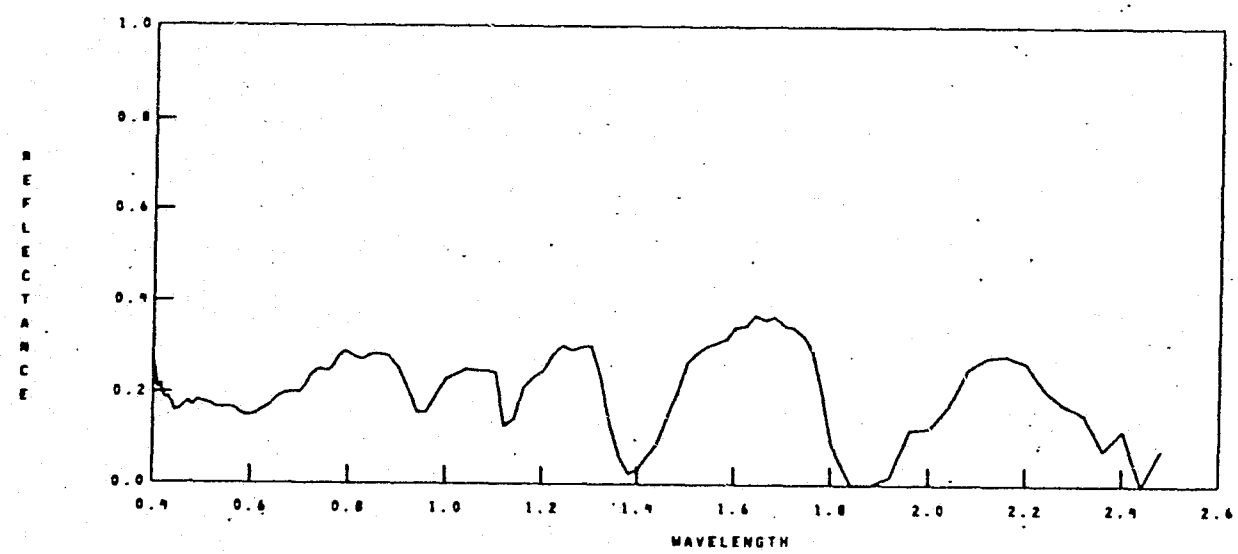
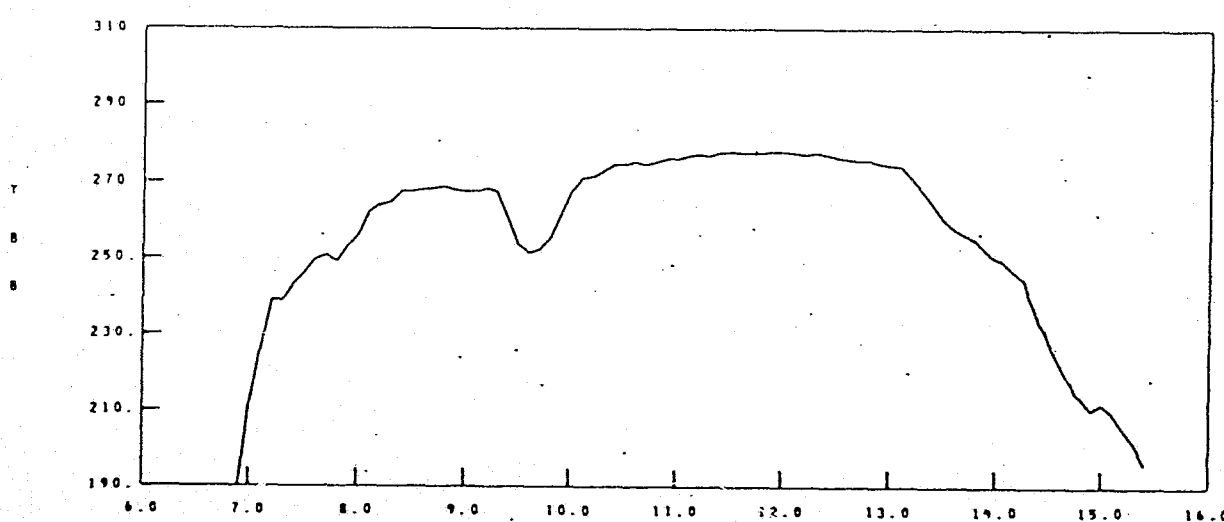
A6-37

S191 DATA 32

MM DD YY
12 273HH MM SS
16 43 27SUN ZENITH ANGLE
68.4LATITUDE
39.52LONGITUDE
5.67

A3-38

S191 DATA 36

MM DD YY
12 273HH MM SS
16 43 31SUN ZENITH ANGLE
68.2LATITUDE
39.38LONGITUDE
5.43

A6-39

S191 DATA 40

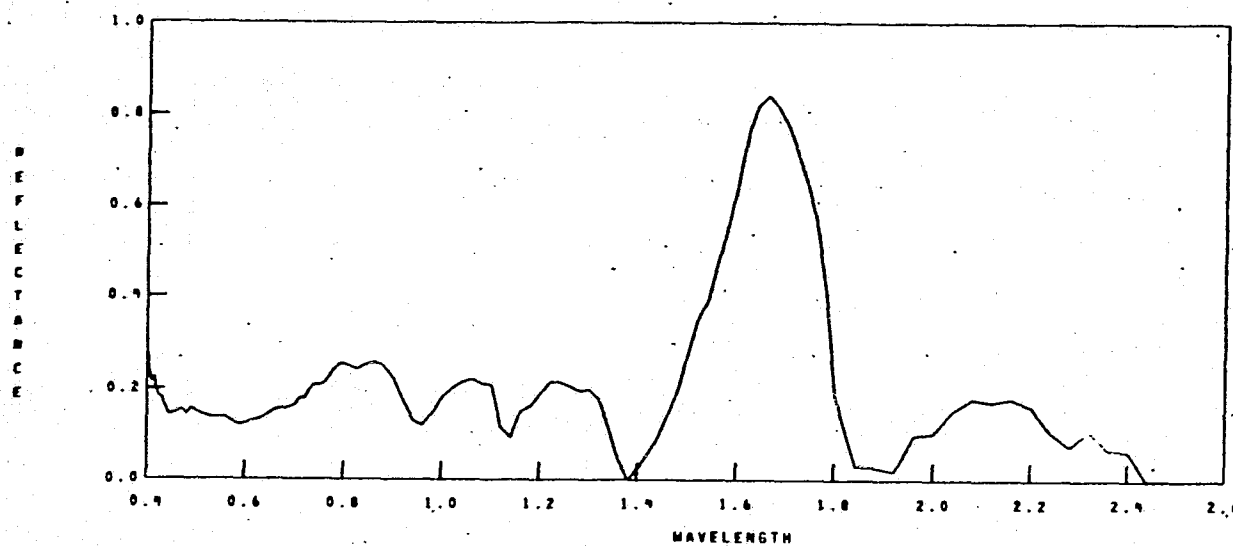
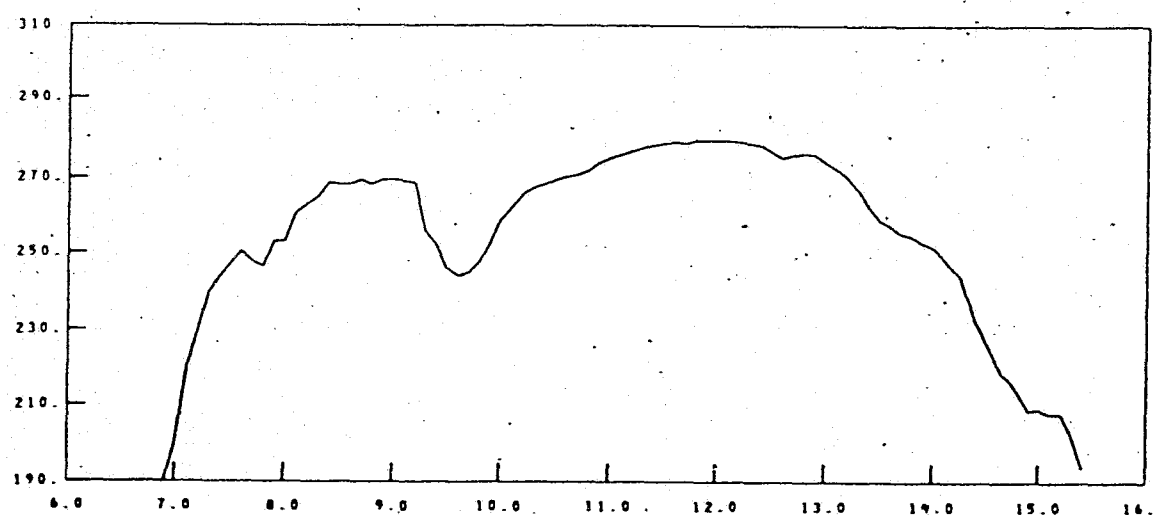
MM DD YY
12 273

HH MM SS
16 43 35

SUN ZENITH ANGLE
68.0

LATITUDE
39.25

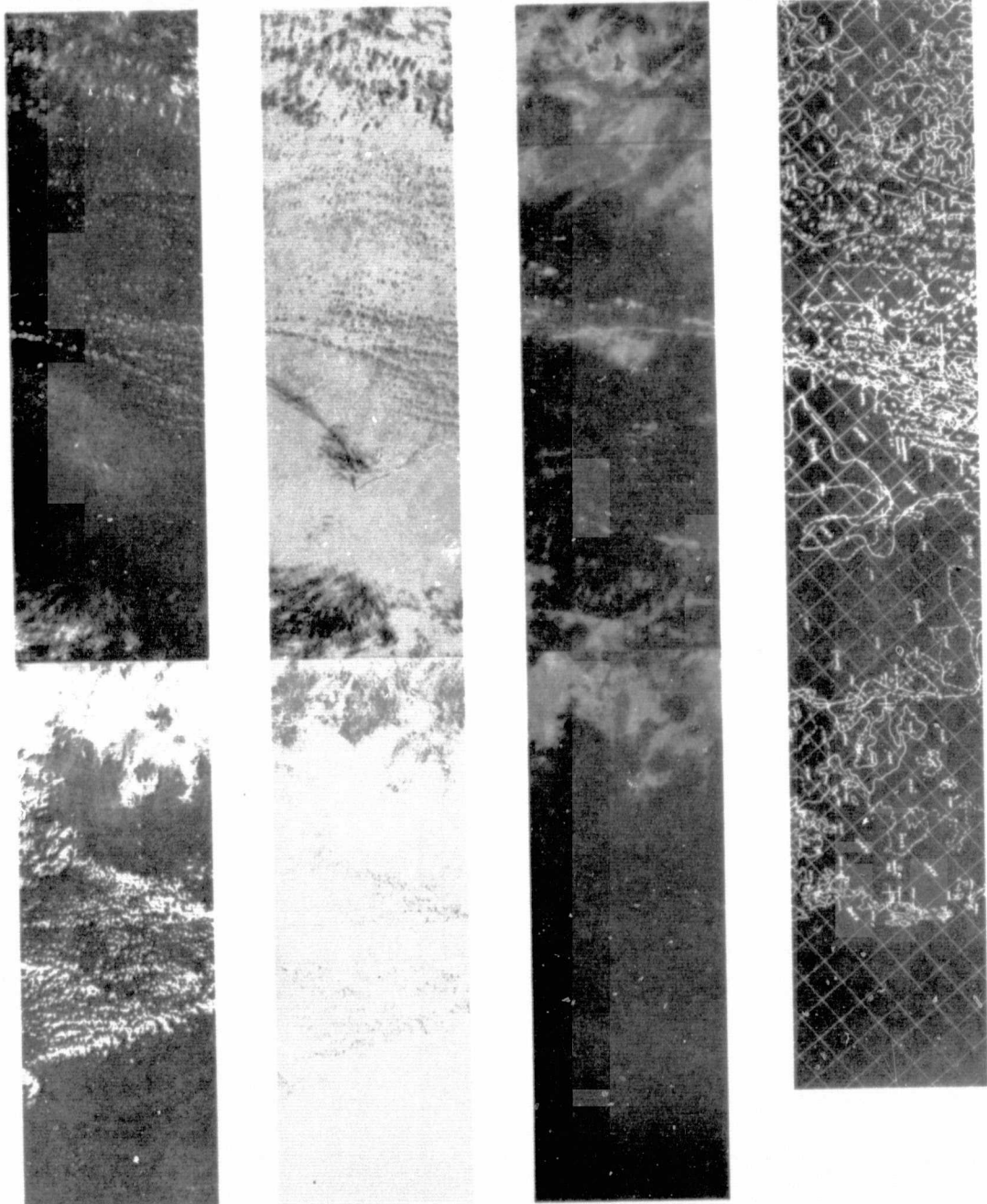
LONGITUDE
5.19



A6-40

DAY 024

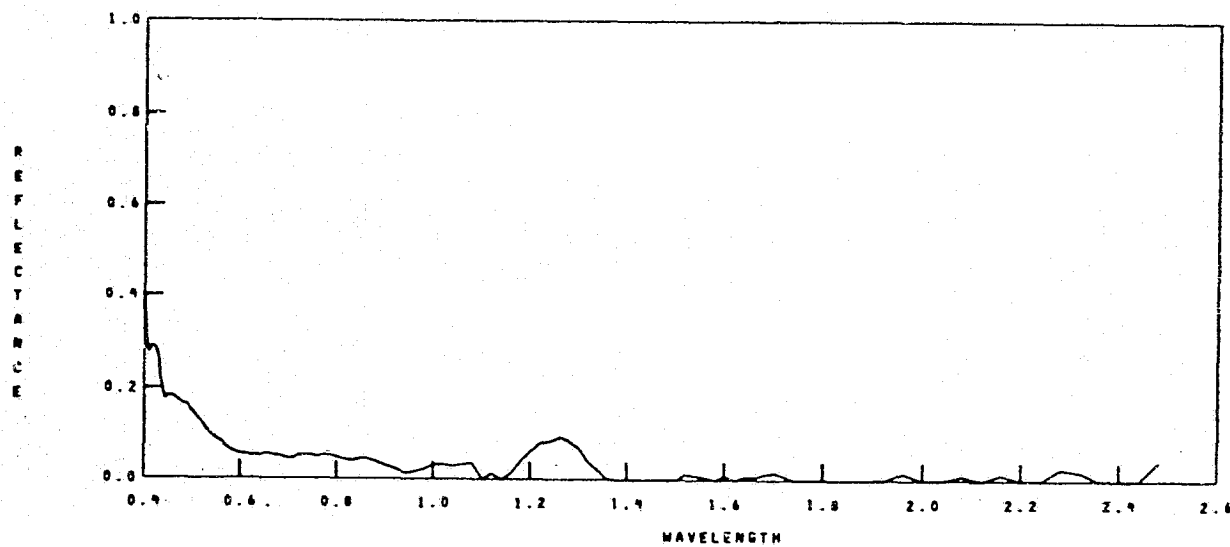
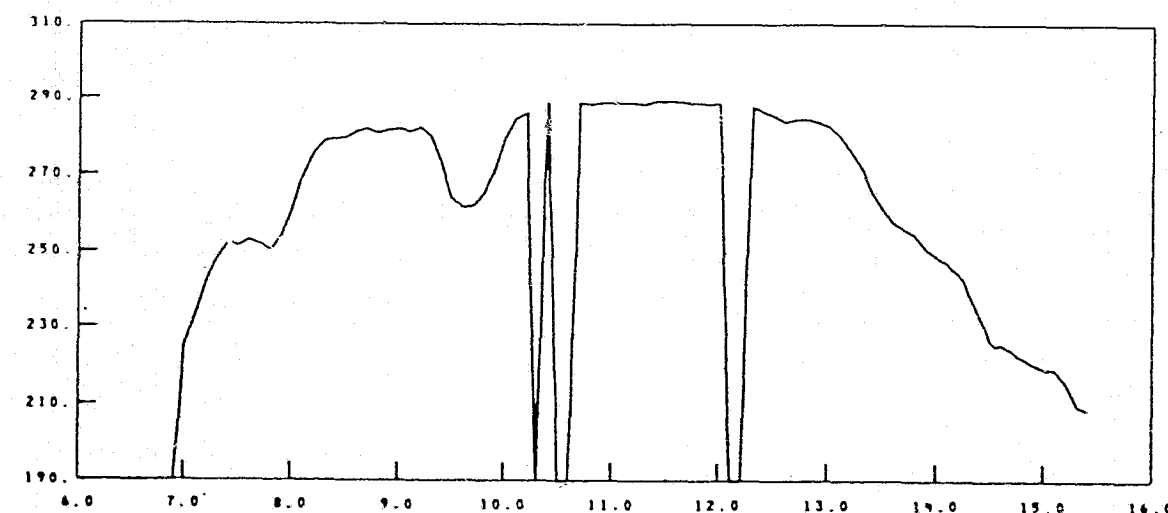
1974



ORIGINAL PAGE IS
OF POOR QUALITY

A6-41

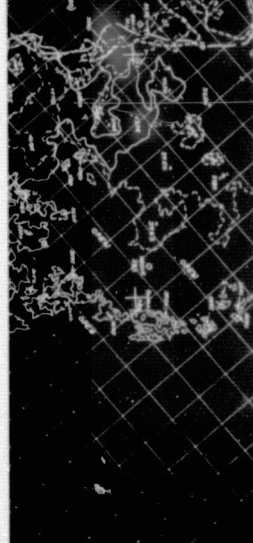
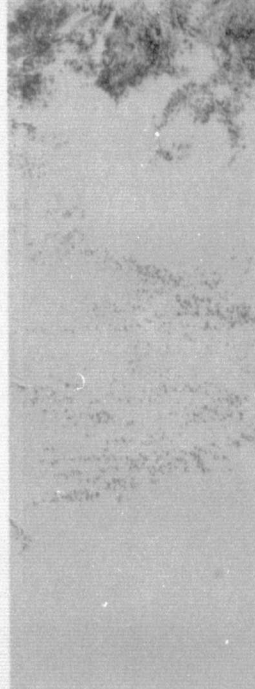
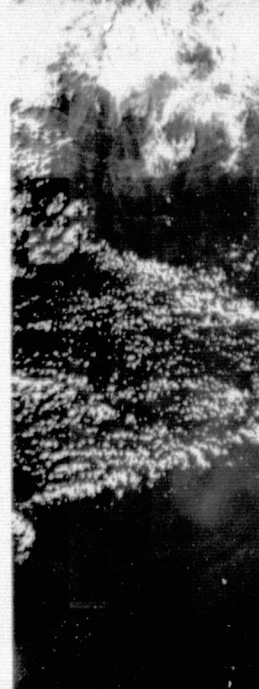
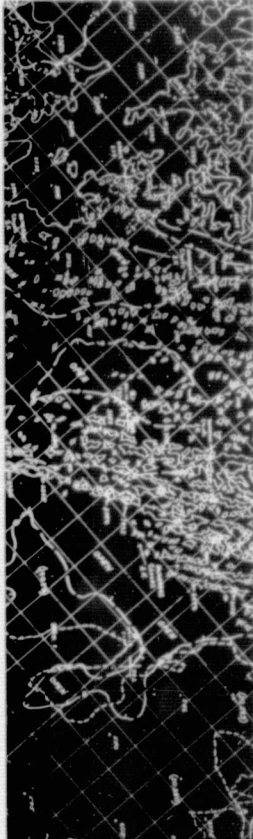
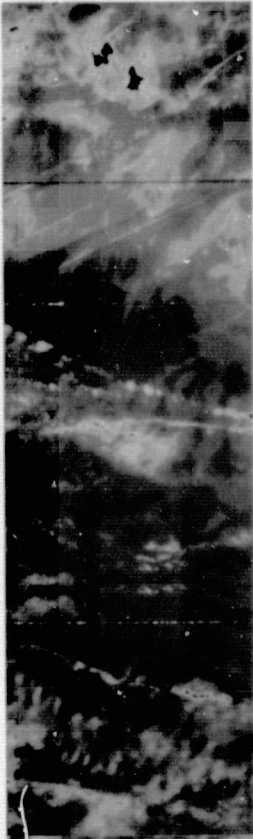
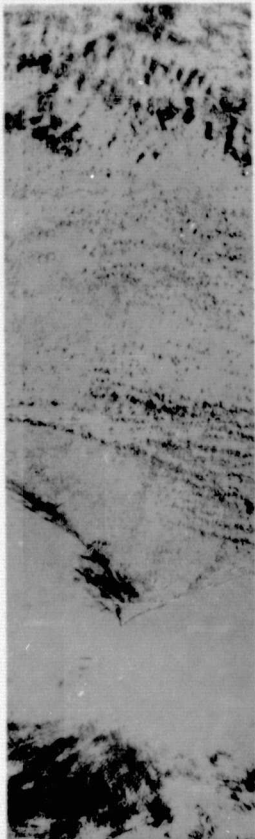
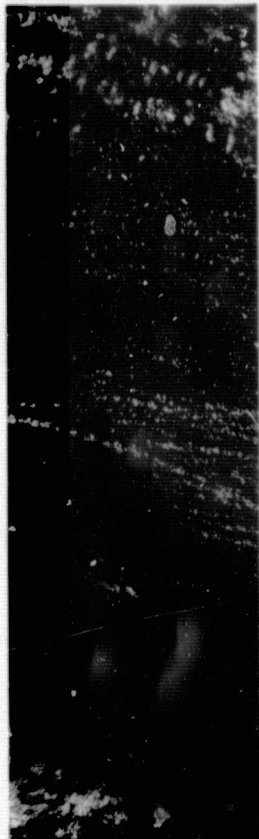
S191 DATA 38

MM DD YY
1 24 74HH MM SS
18 1 25SUN ZENITH ANGLE
54.7LATITUDE
35.02LONGITUDE
74.54

A6-42

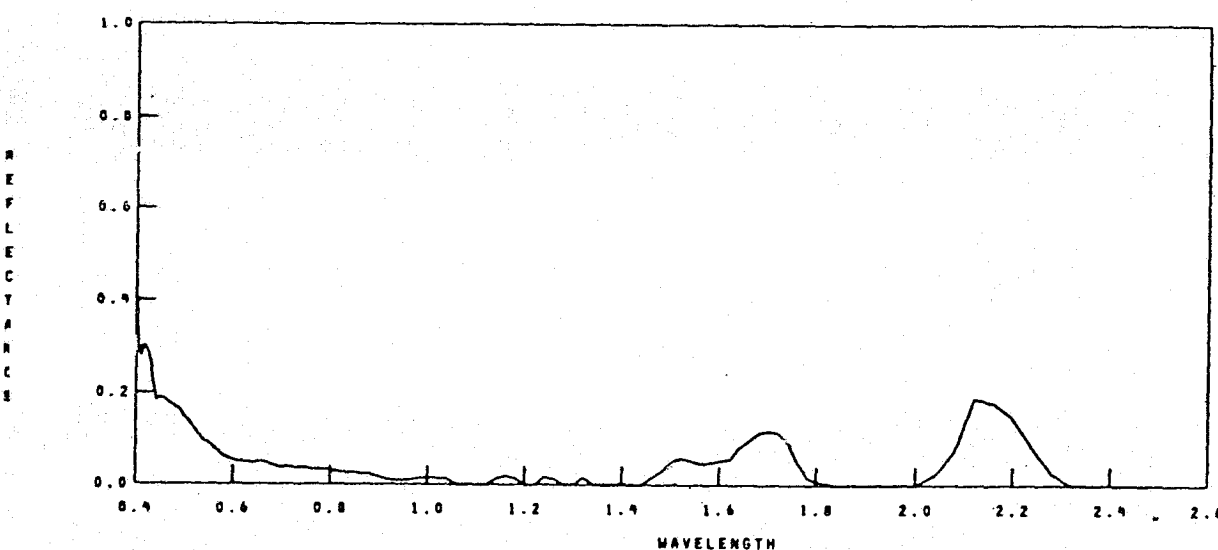
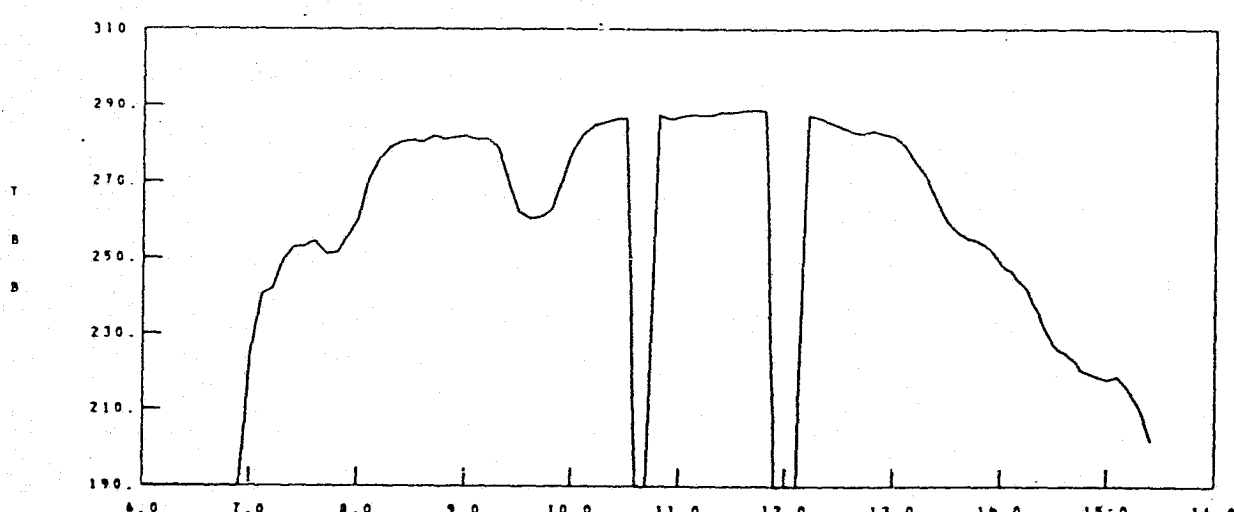
DAY 024

1974



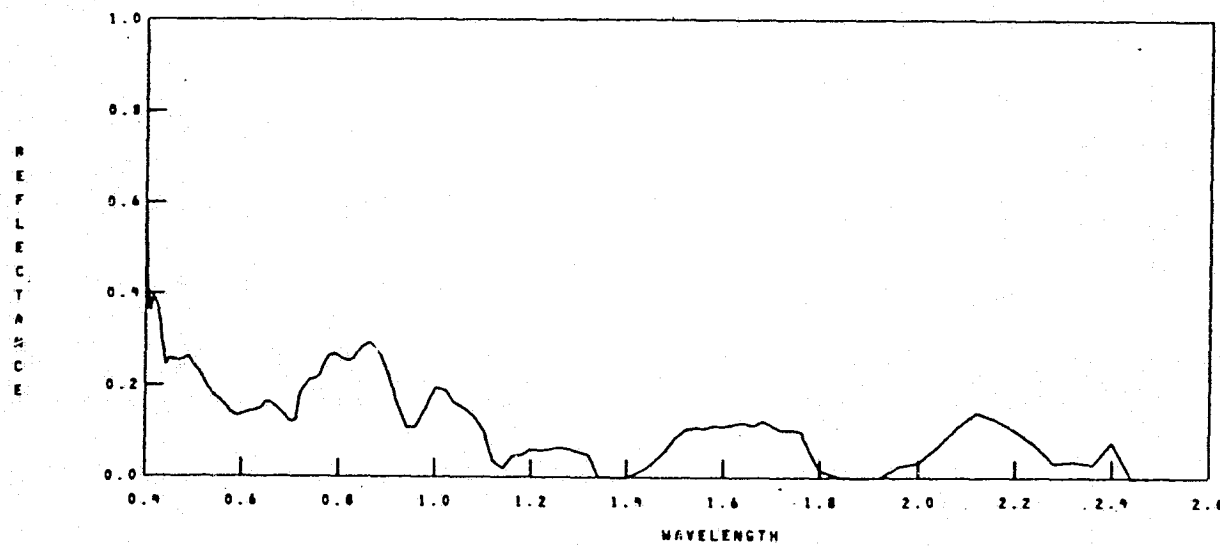
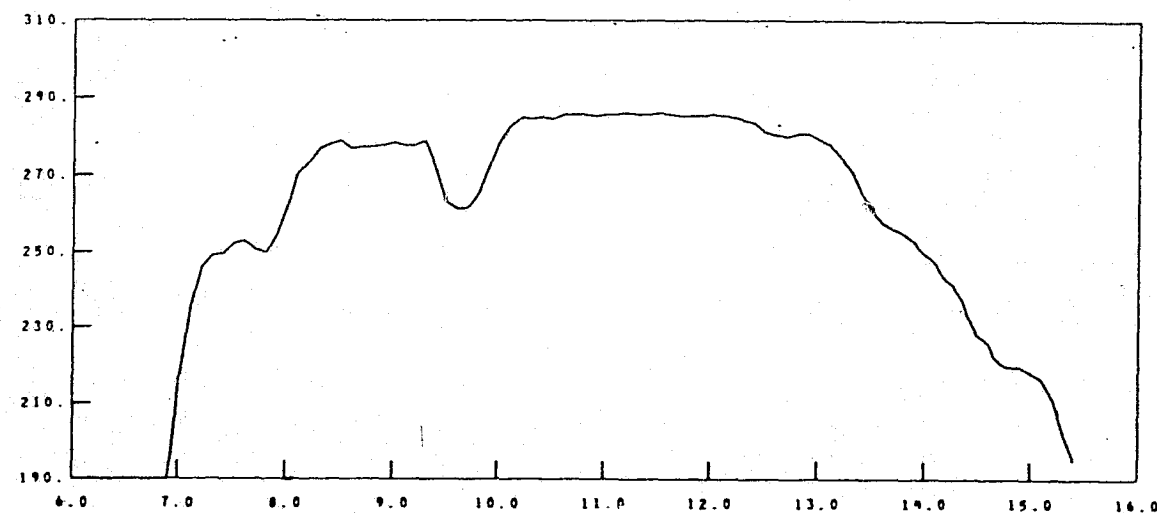
AG42a

S191 DATA 40

MM DD YY
1 29 79HH MM SS
18 1 26SUN ZENITH ANGLE
54.7LATITUDE
34.98LONGITUDE
79.48

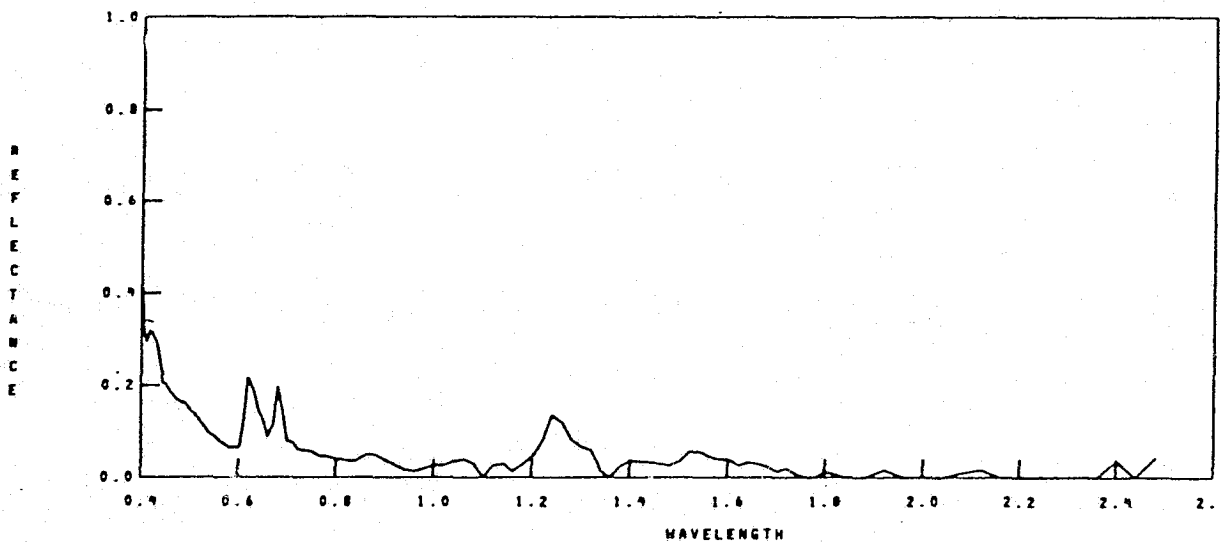
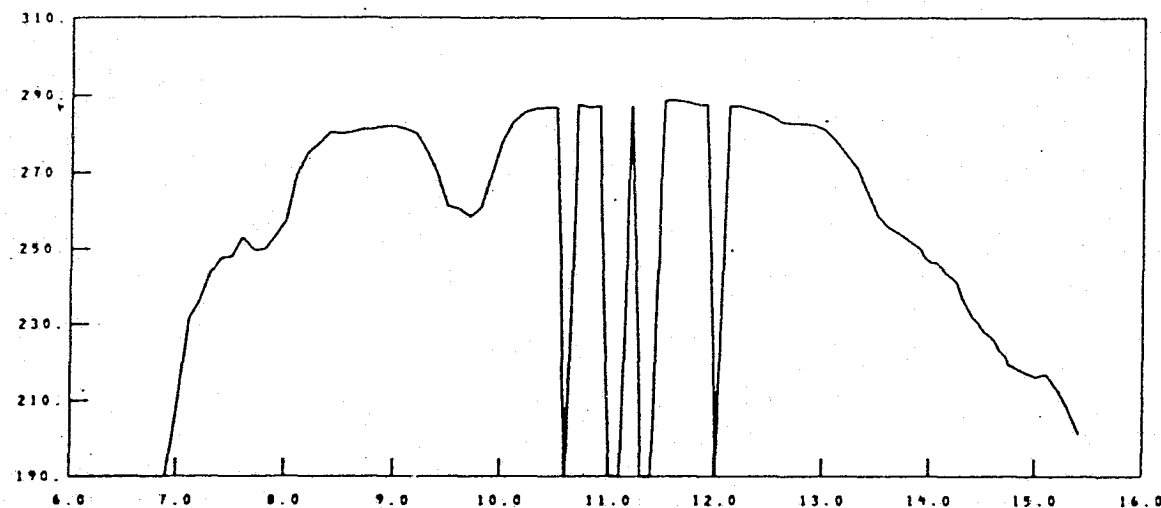
A6-49

S191 DATA 44

MM DD YY
1 24 74HH MM SS
18. 1 30SUN ZENITH ANGLE
54.6LATITUDE
39.83LONGITUDE
79.27

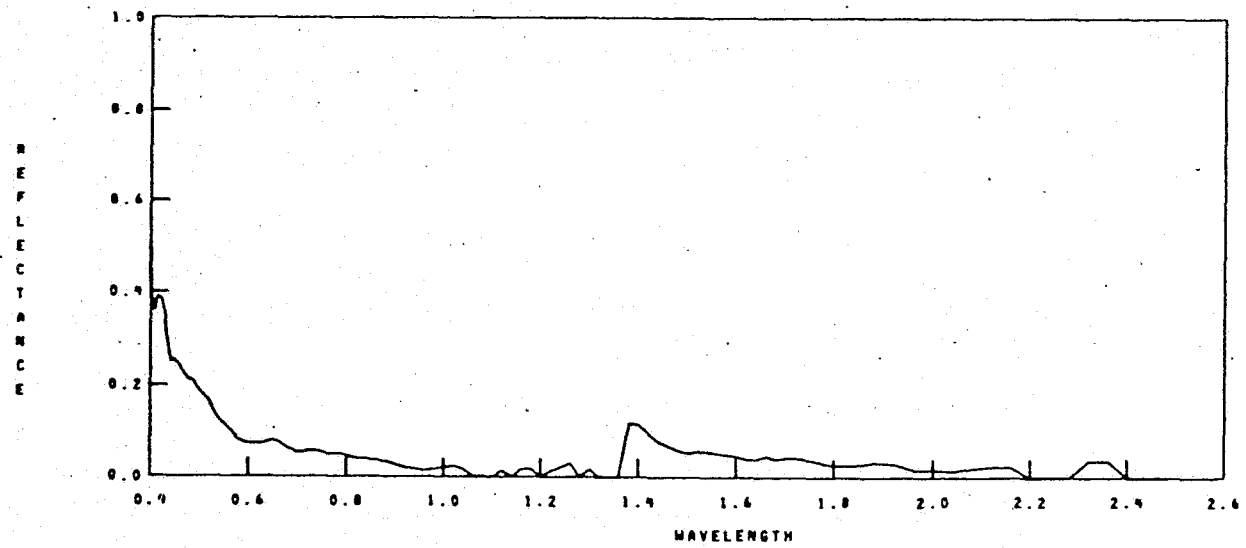
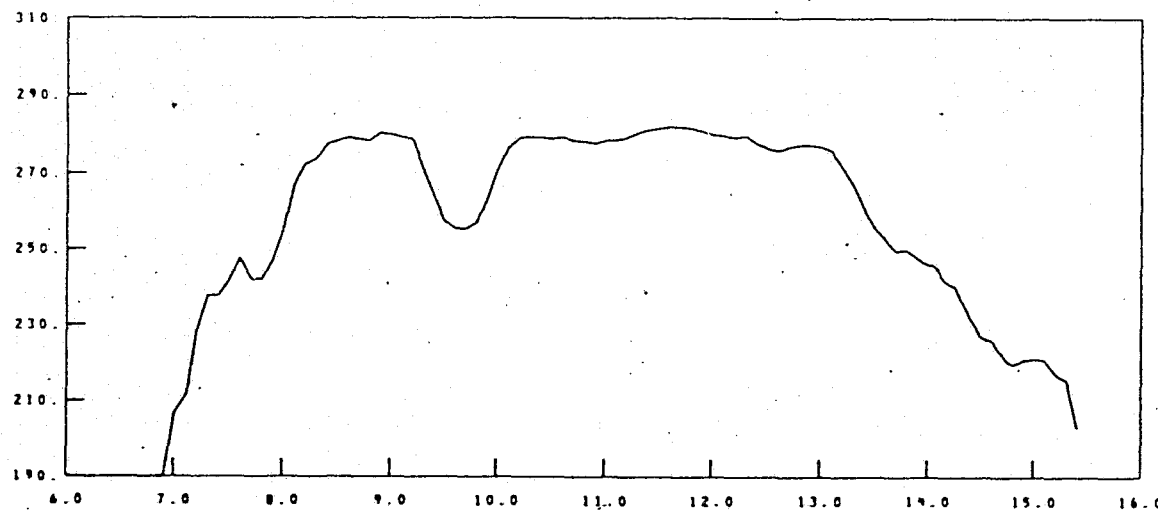
A6-44

S191 DATA 46

HH DD YY
1 24 74HH MM SS
18 13 39SUN ZENITH ANGLE
54.9LATITUDE
34.65LONGITUDE
79.01

A6-45

S191 DATA 52

MM DD YY
12 24 74HH MM SS
16 1 38SUN ZENITH ANGLE
59.3LATITUDE
34.50LONGITUDE
78.80

A6-46

5191 DATA 56

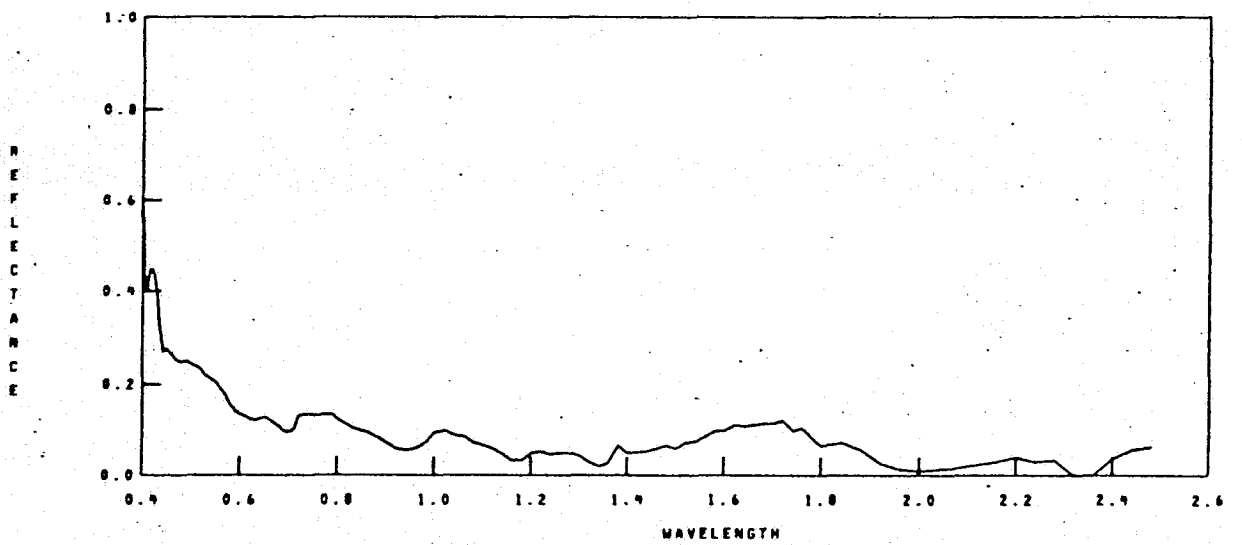
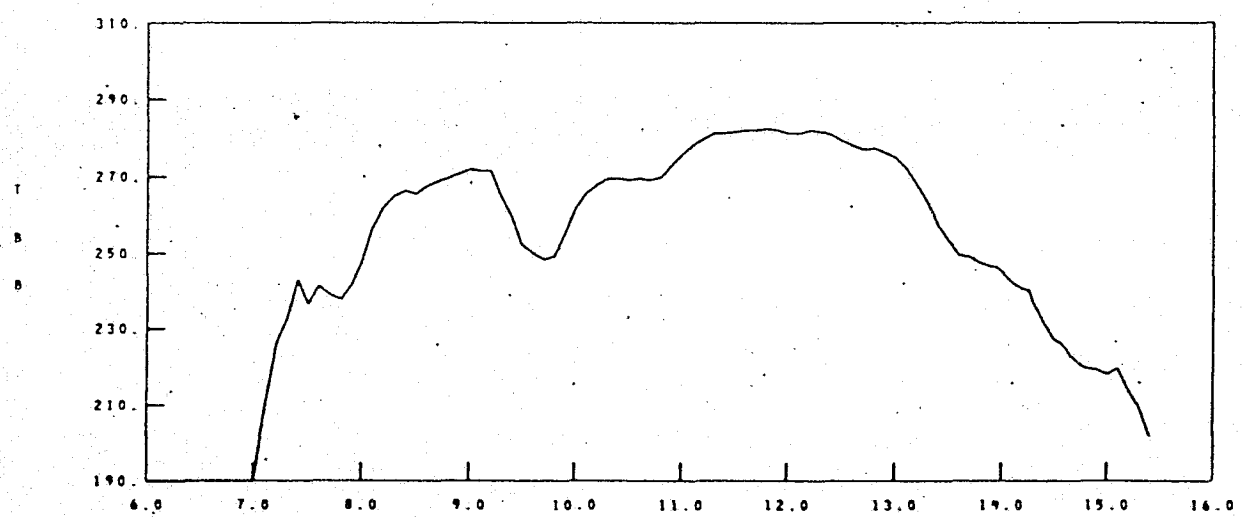
MM DD YY
1 24 74

HH MM SS
18 1 44

SUN ZENITH ANGLE
59.1

LATITUDE
34.27

LONGITUDE
78.49



A6-47

A6-48

S191 DATA 60

RR CC YY

1 24 74

HH MM SS

18 1 47

SUN ZENITH ANGLE

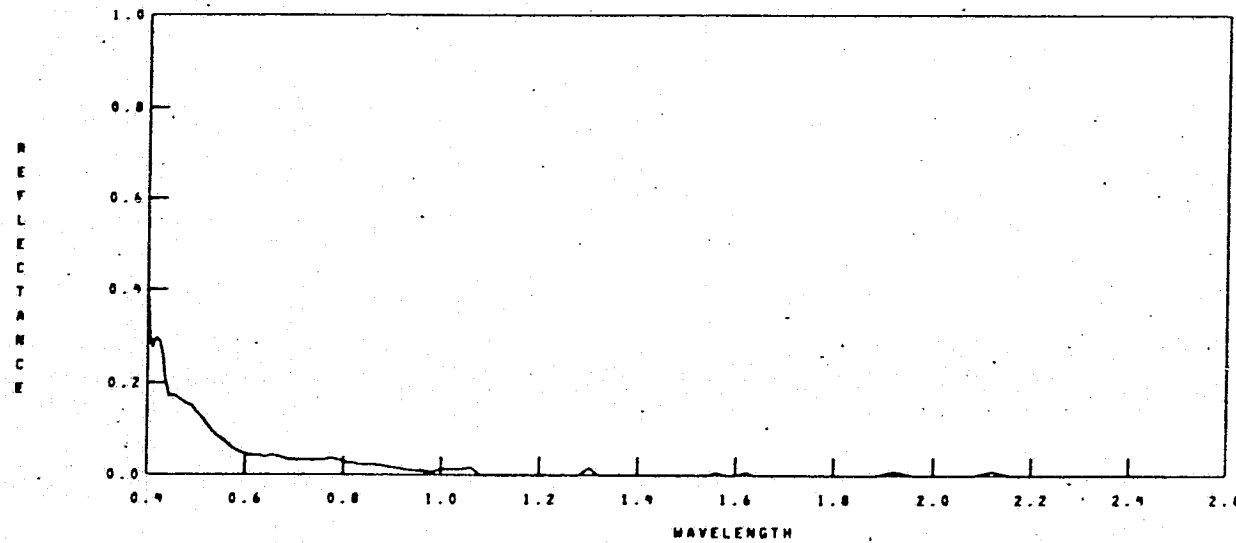
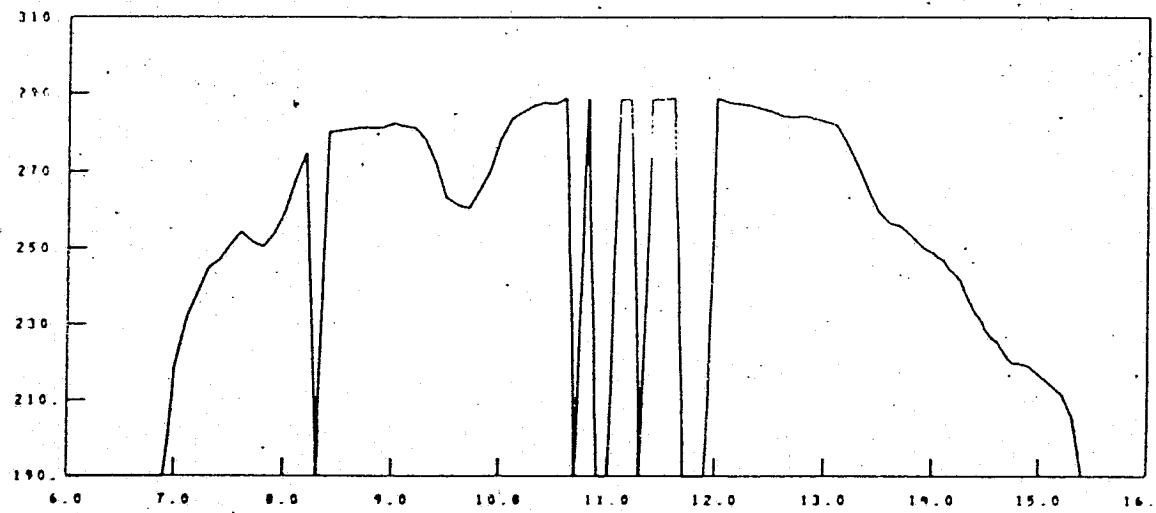
59.0

LATITUDE

34.12

LONGITUDE

78.29



S191-DATA 66

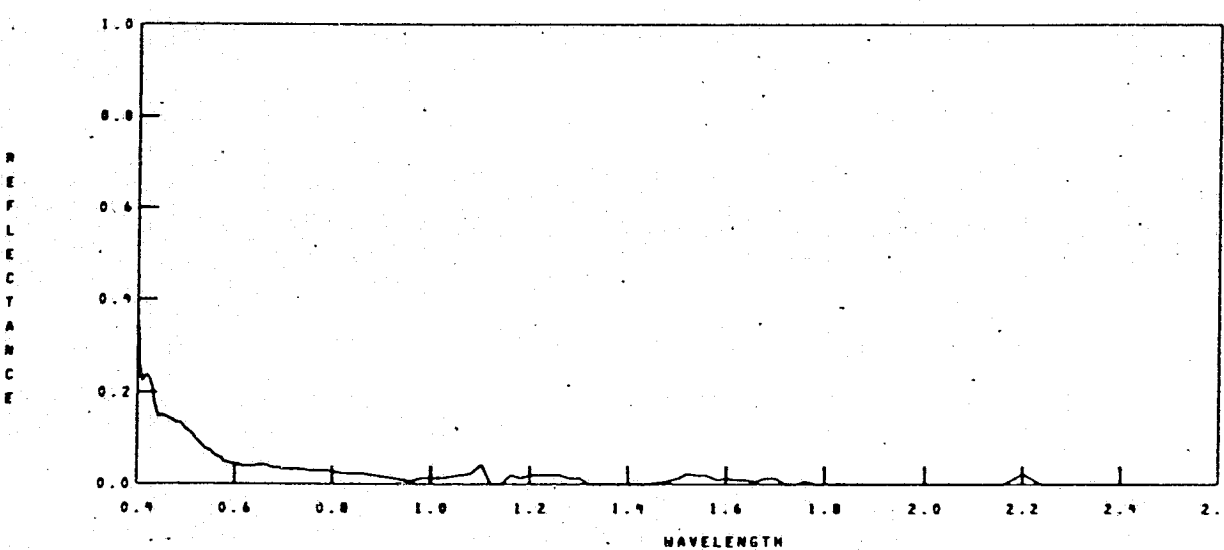
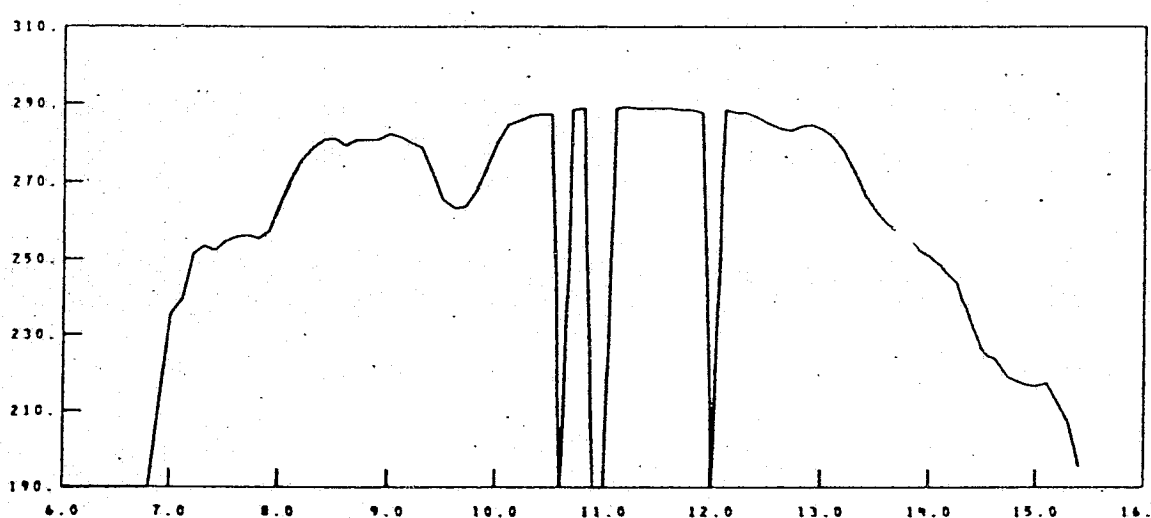
MM DD YY
1 29 74

HH MM SS
16 1 53

SUN ZENITH ANGLE
53.8

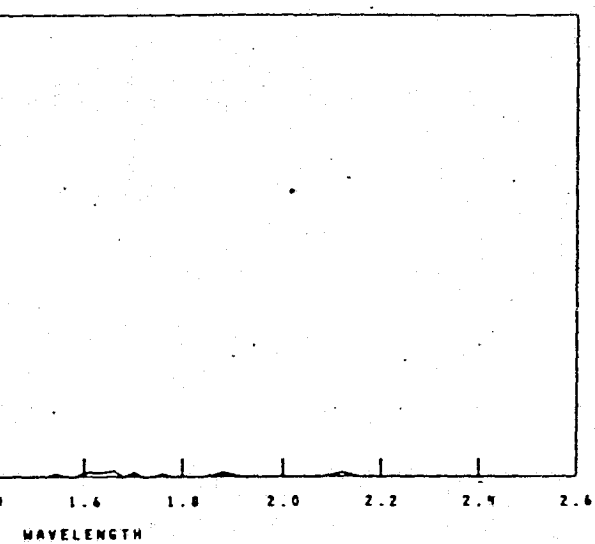
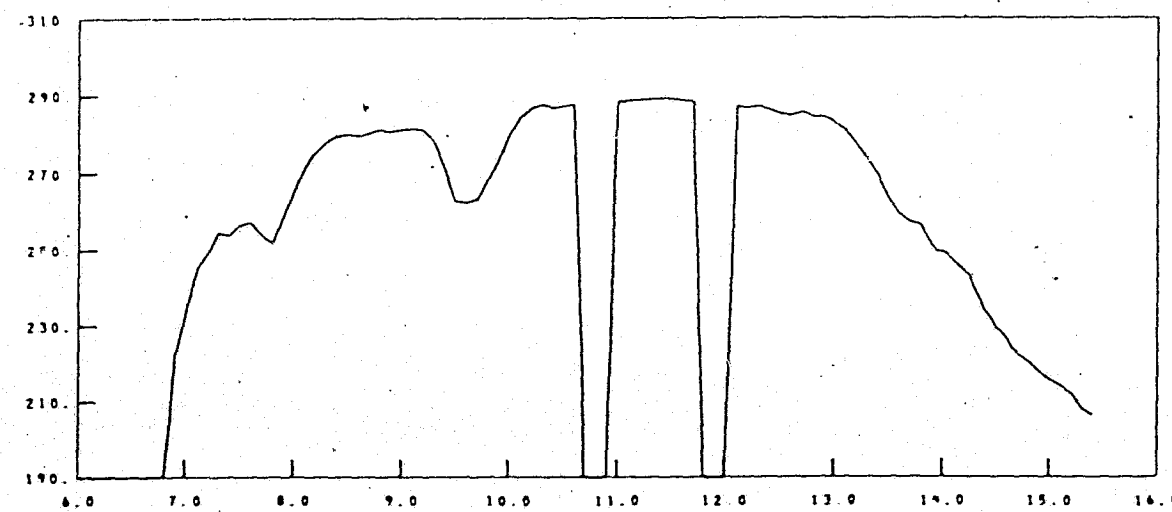
LATITUDE
33.89

LONGITUDE
77.98



A6-49

S191 DATA 72

RR DD YY
1 24 74HH MM SS
18 1 59SUN ZENITH ANGLE
53.7LATITUDE
33 66
LONGITUDE
77 67

A6-50

S191 DATA 38

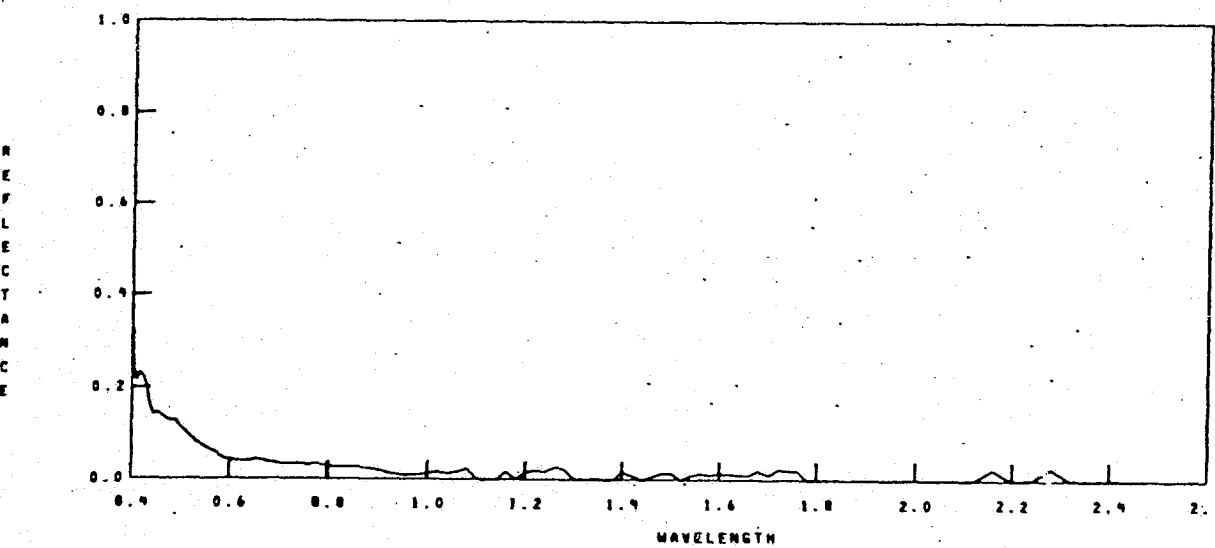
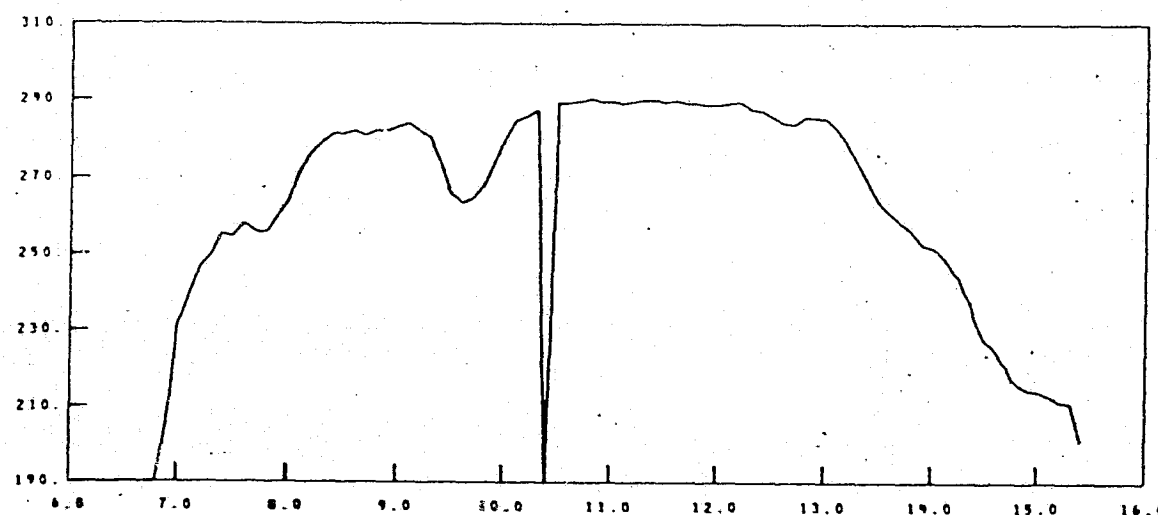
MM DD YY
1-24-78

HH MM SS
18 2 4

SUN ZENITH ANGLE
53.5

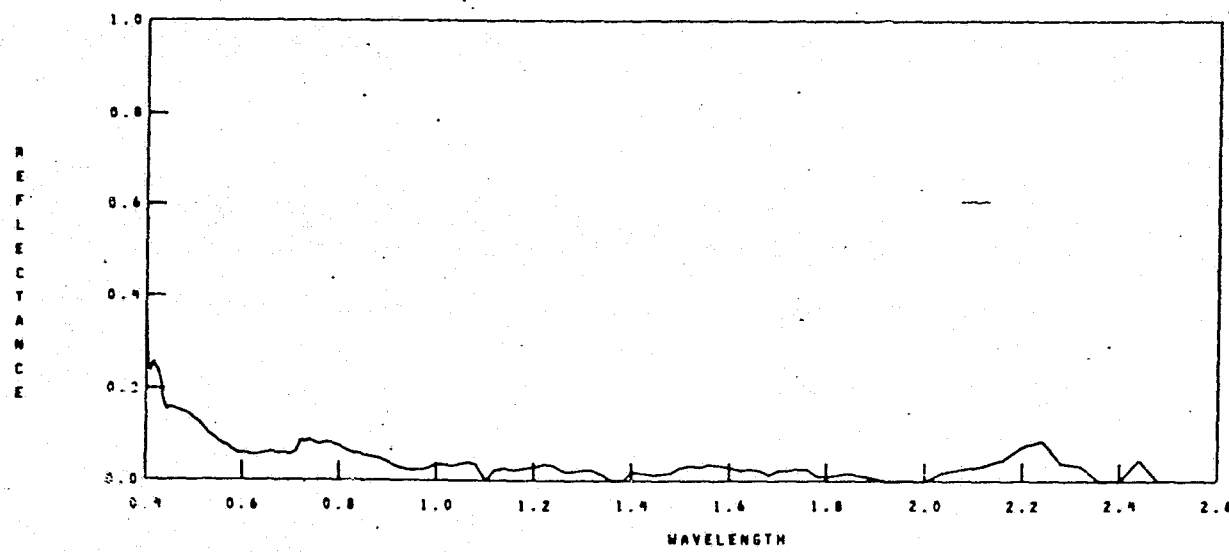
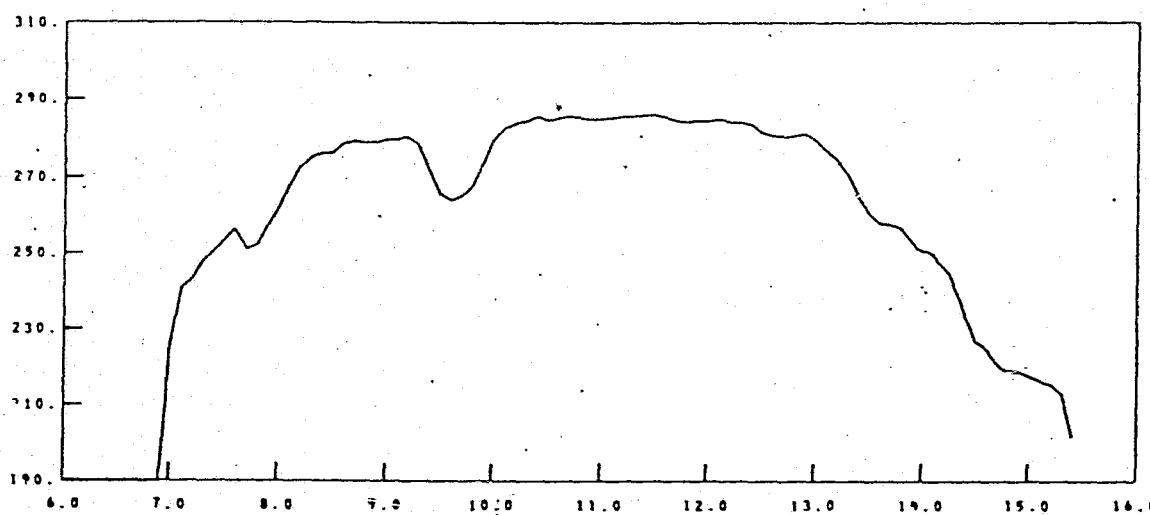
LATITUDE
33.43

LONGITUDE
77.36



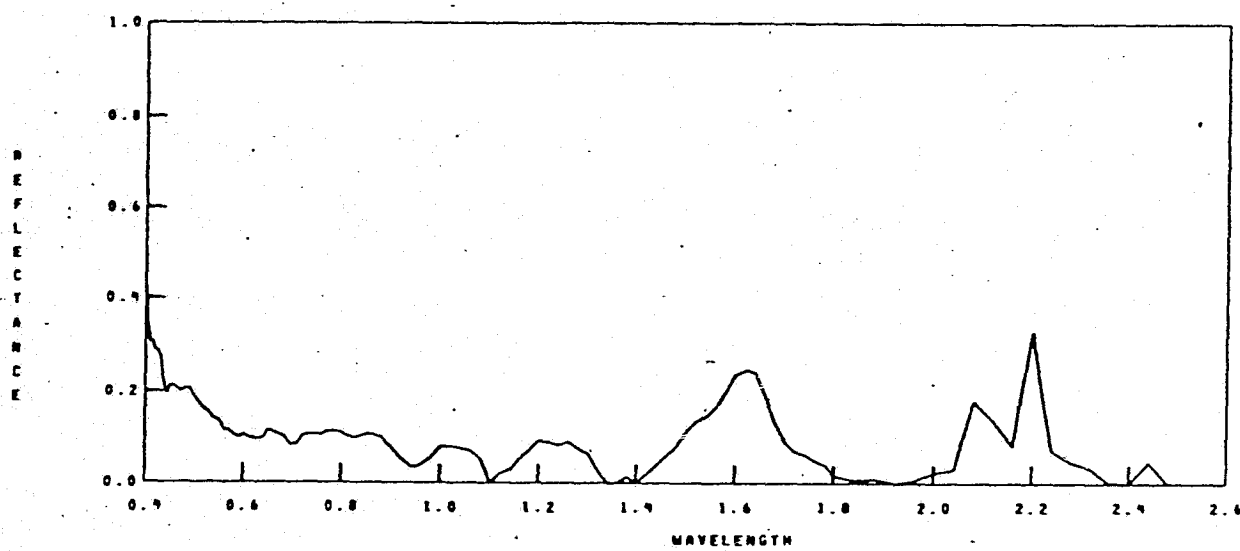
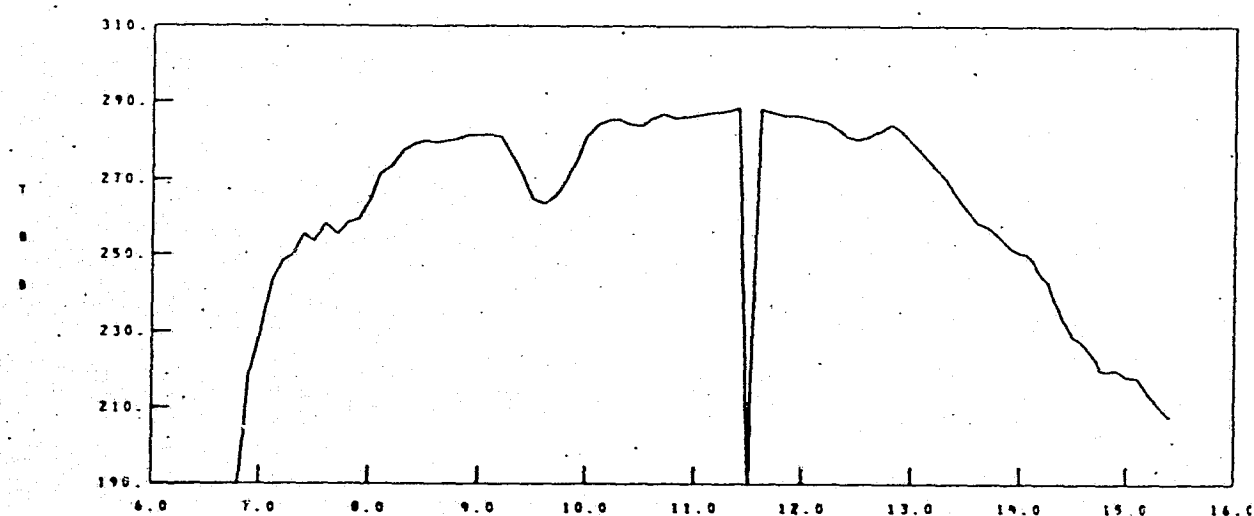
A6-51

5191 DATA 84

MM DD YY
12 24 79HH MM SS
18 2 11SUN ZENITH ANGLE
53.2LATITUDE
33.13LONGITUDE
76.96

A6-52

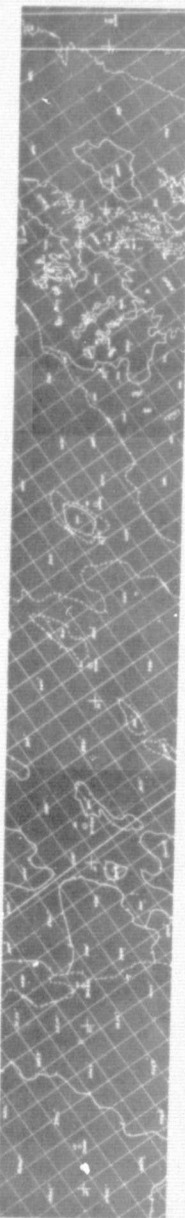
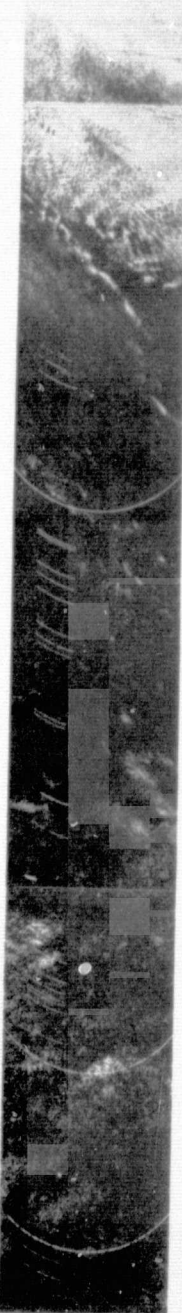
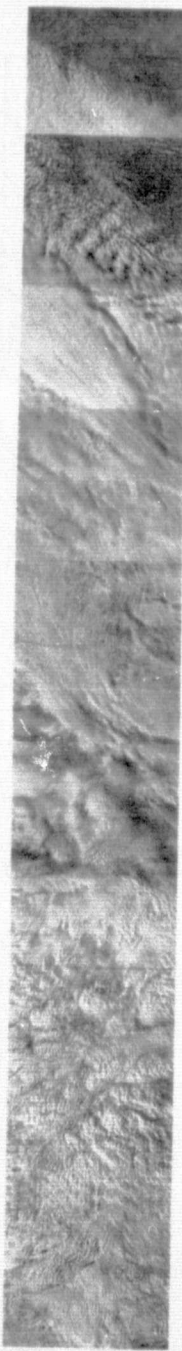
S191 DATA 90

MM DD YY
1 29 79HH MM SS
18 2 19SUN ZENITH ANGLE
53.1LATITUDE
32.82LONGITUDE
76.55

A6-53

DAY 025

1974

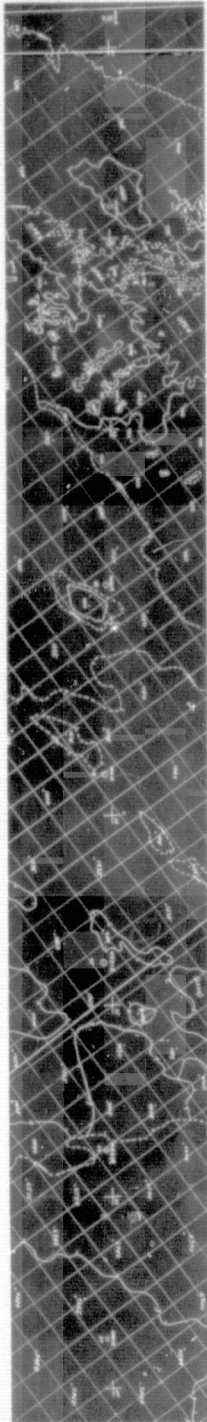
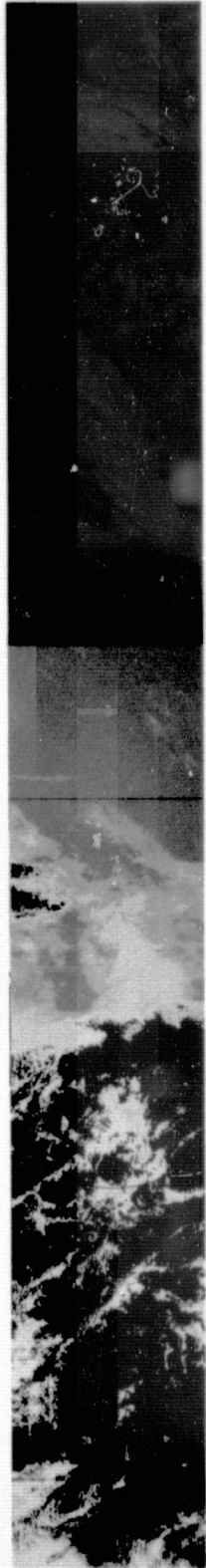
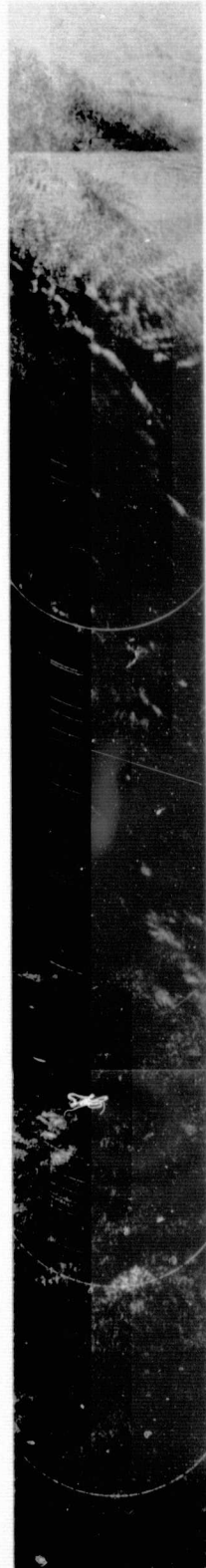
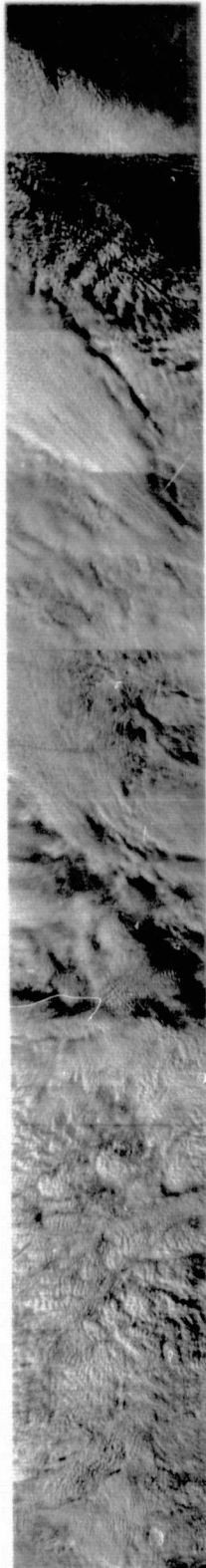


ORIGINAL PAGE IS
OF POOR QUALITY

A6-54

DAY 025

1974



A6-54 a

5191 DATA 14

MM DD YY

1 25 74

HH MM SS

17 17 13

SUN ZENITH ANGLE

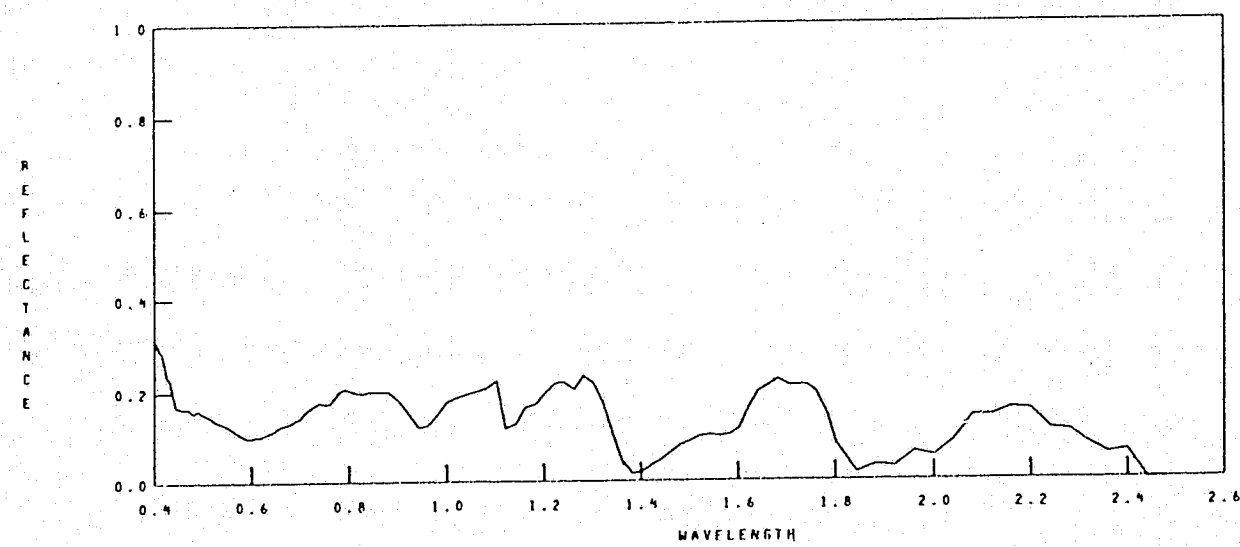
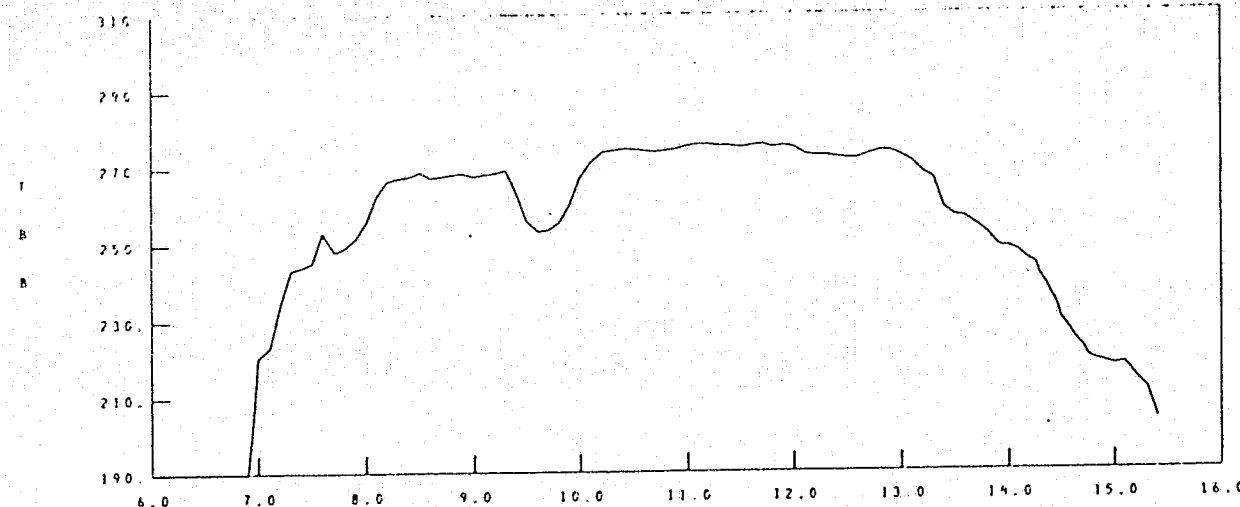
57.9

LATITUDE

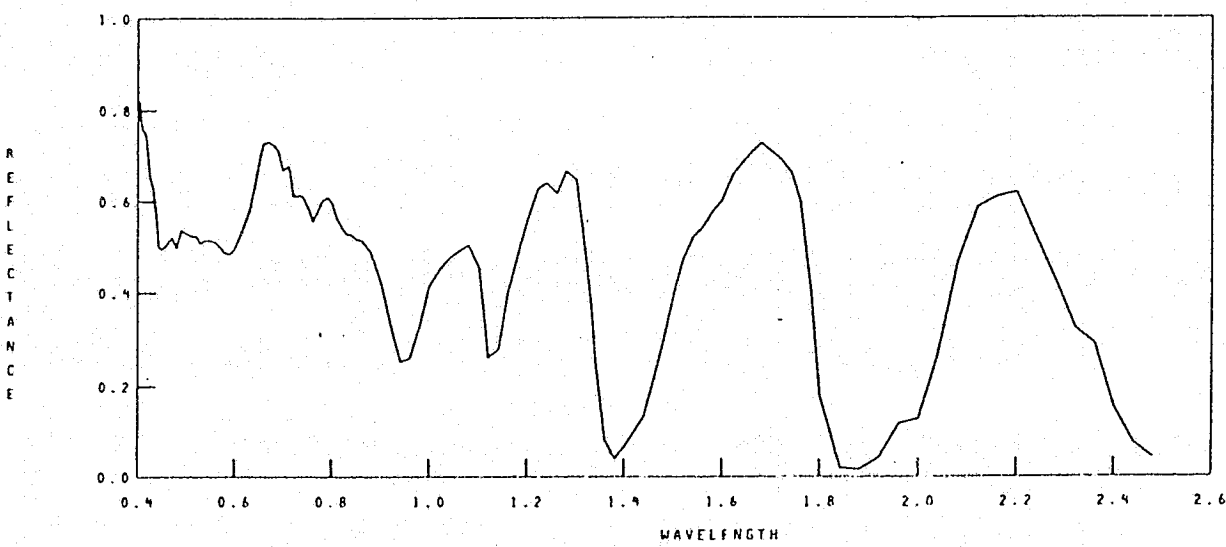
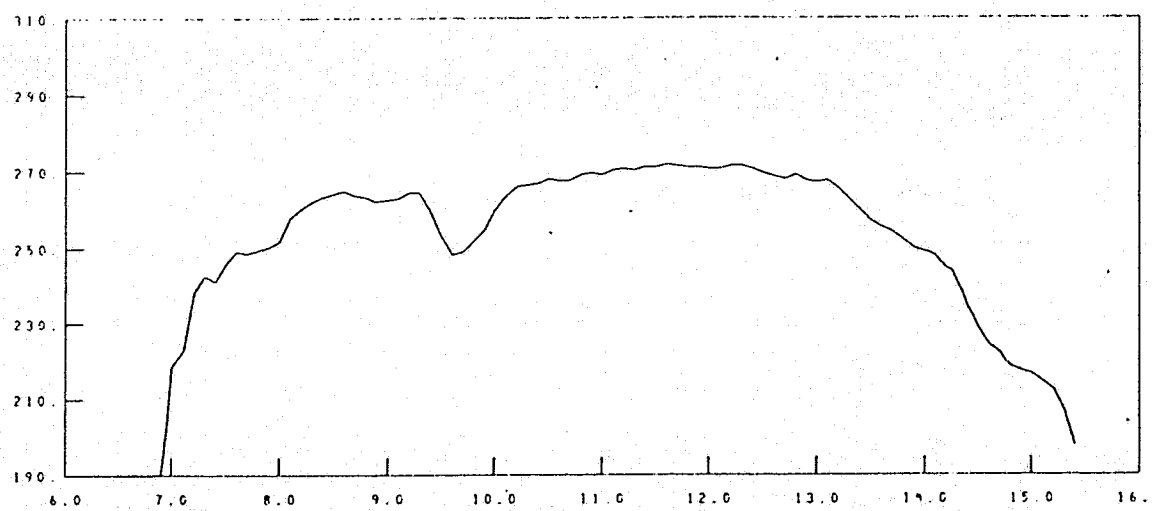
39.00

LONGITUDE

81.08

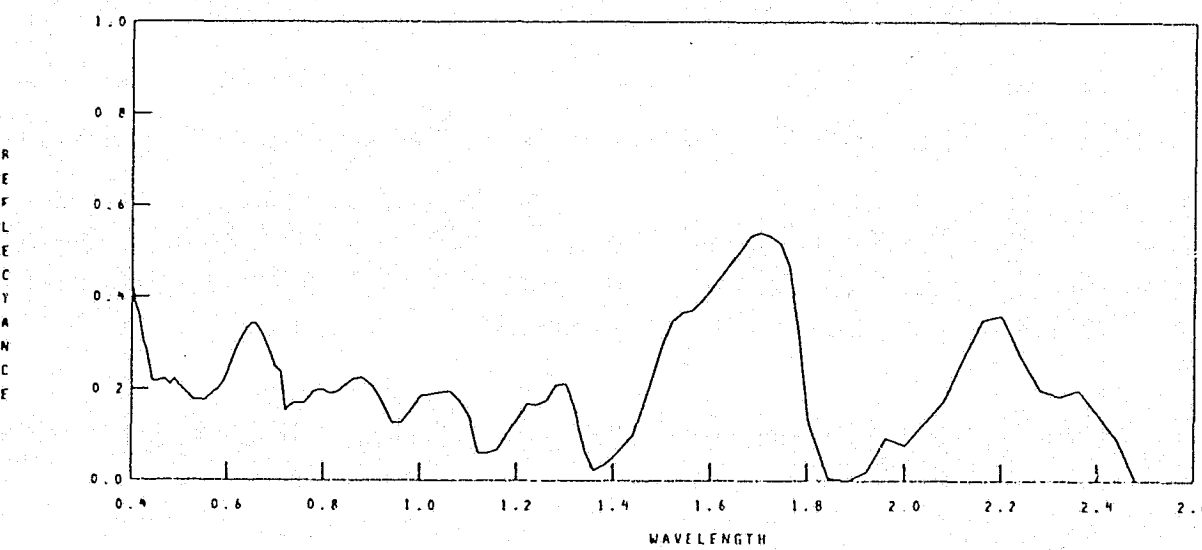
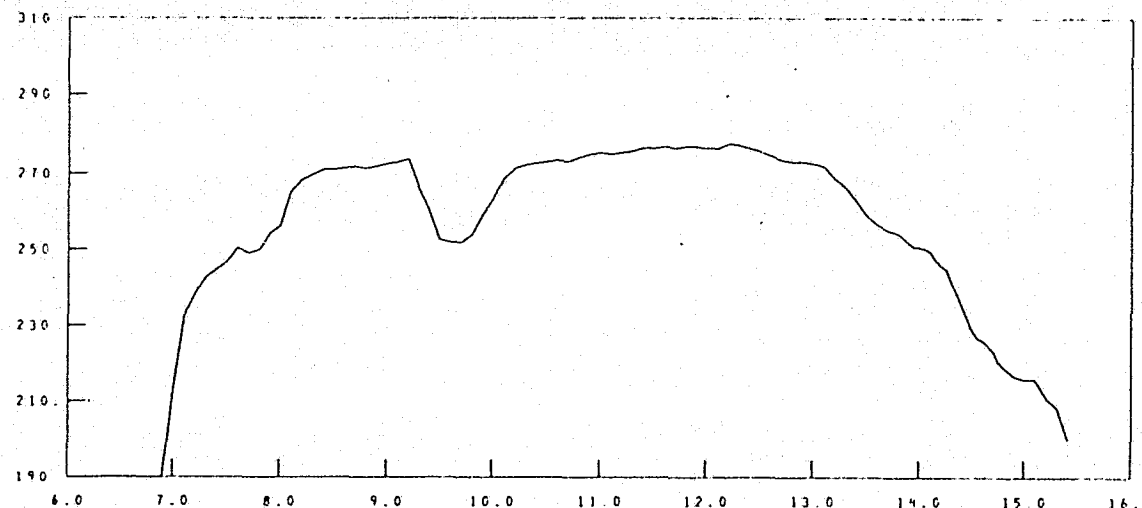


S191 DATA 18

MM DD YY
1 25 74HH MM SS
17 17 17SUN ZENITH ANGLE
57.9LATITUDE
38.86LONGITUDE
80.85

A6-56

S191 DATA 22

MM DD YY
1 25 74HH MM SS
17 17 21SUN ZENITH ANGLE
57.8LATITUDE
38.72LONGITUDE
80.60

A6-57

S191 DATA 26

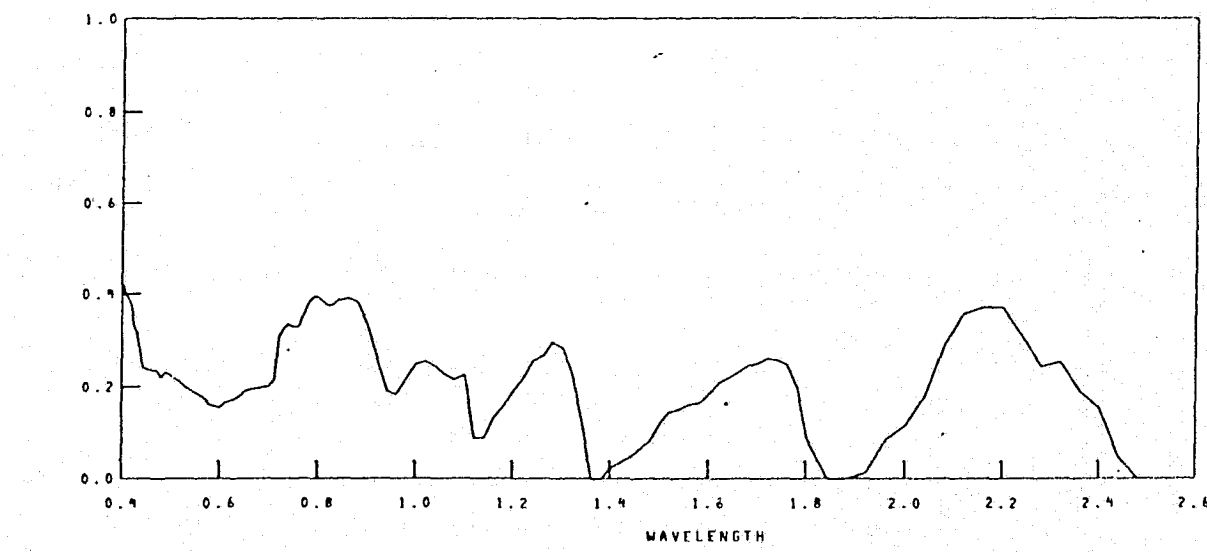
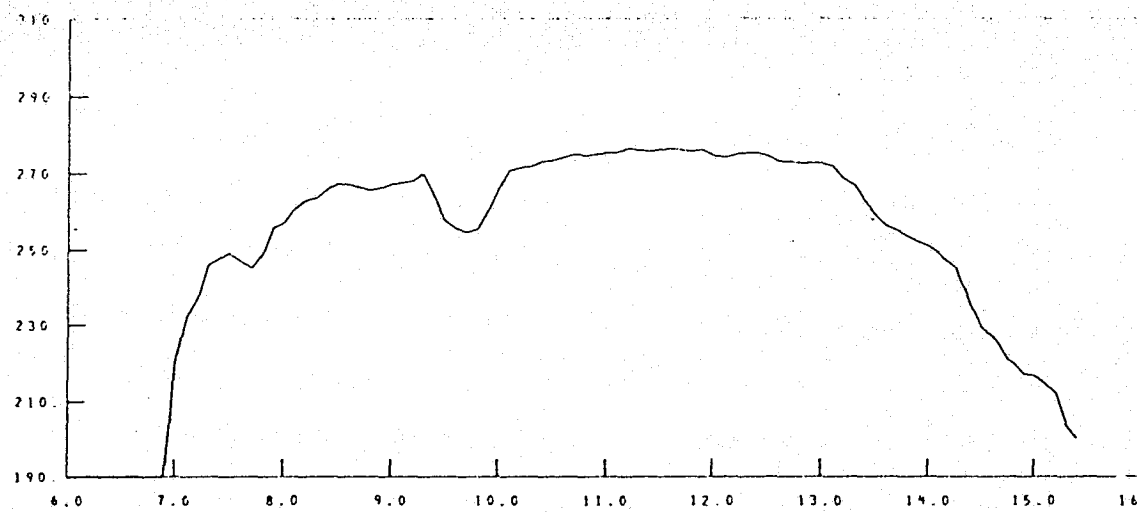
MM DD YY
1 25 74

HR MM SS
17 17 24

SUN-ZENITH ANGLE
57.6

LATITUDE
38.59

LONGITUDE
80.37



A6-58

5191 DATA 30

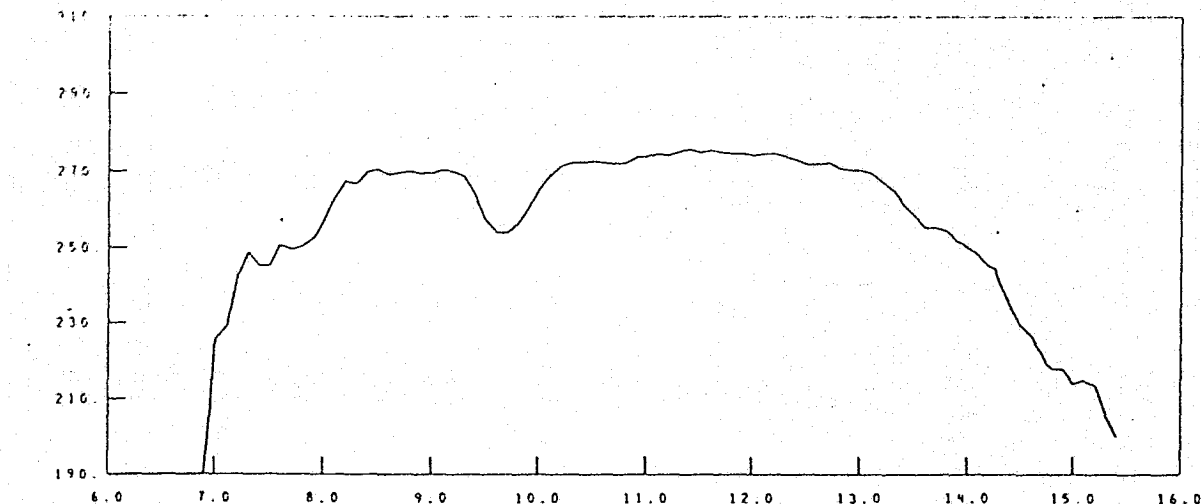
MM DD YY
1 25 74

HH MM SS
17 17 28

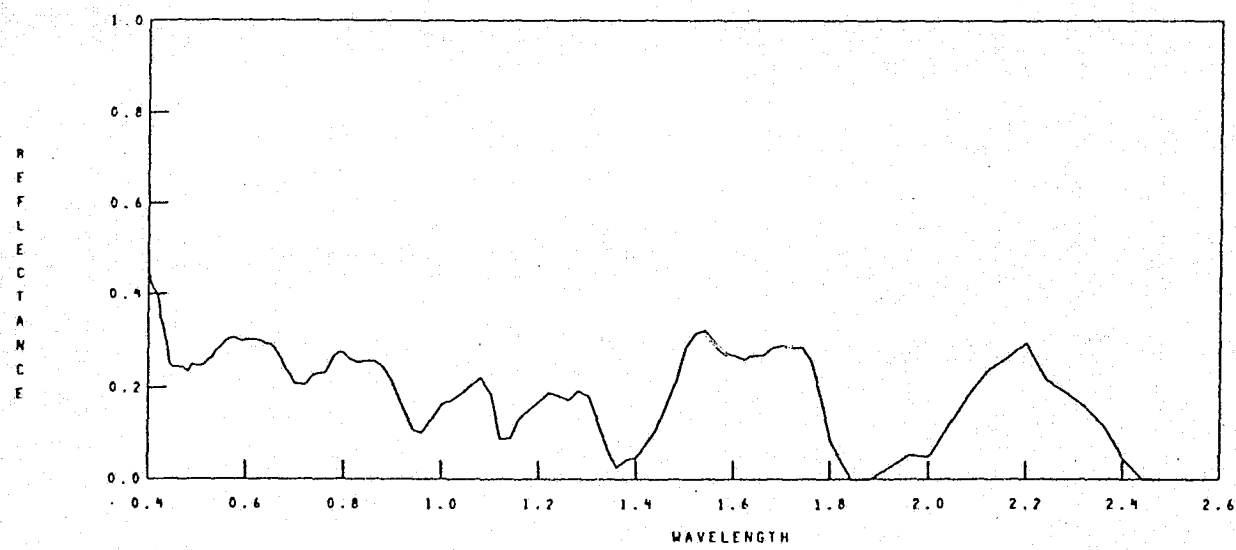
SUN ZENITH ANGLE
57.5

LATITUDE
38.45

LONGITUDE
80.14



A6-59



S191 DATA 34

MM DD YY

1 25 74

HH MM SS

17 17 33

SUN ZENITH ANGLE

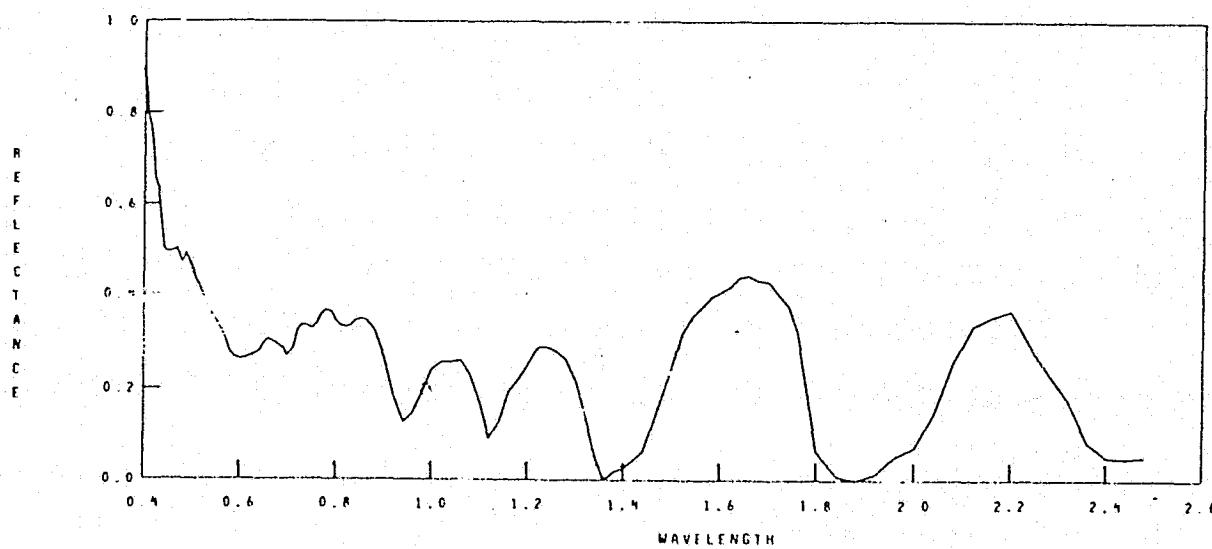
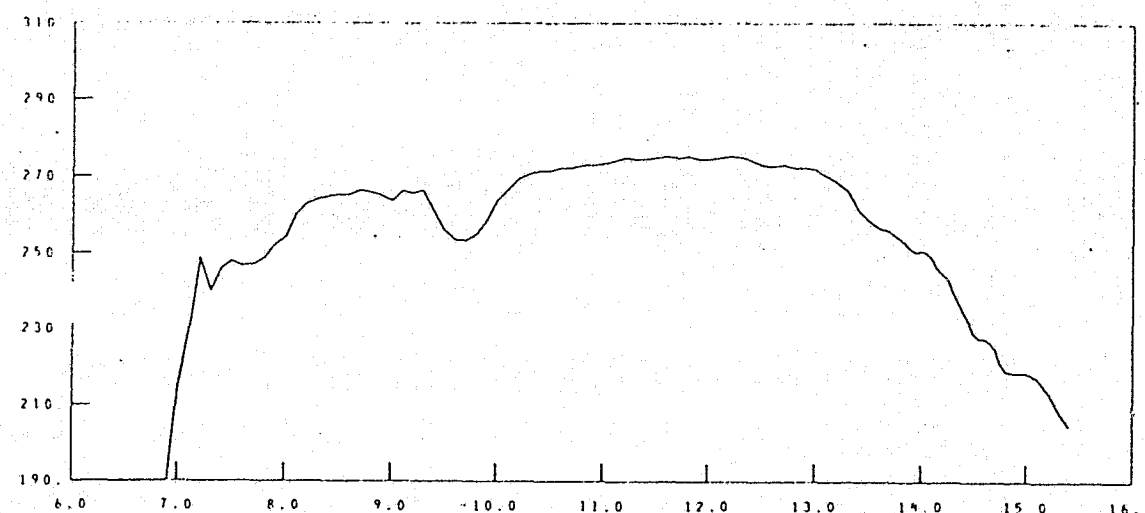
57.3

LATITUDE

38.28

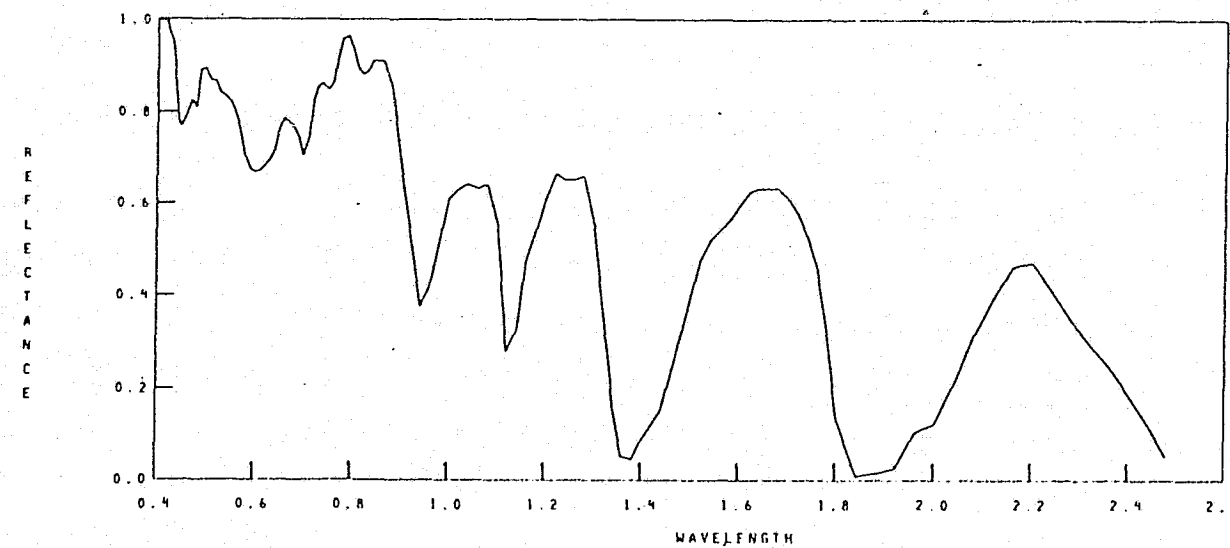
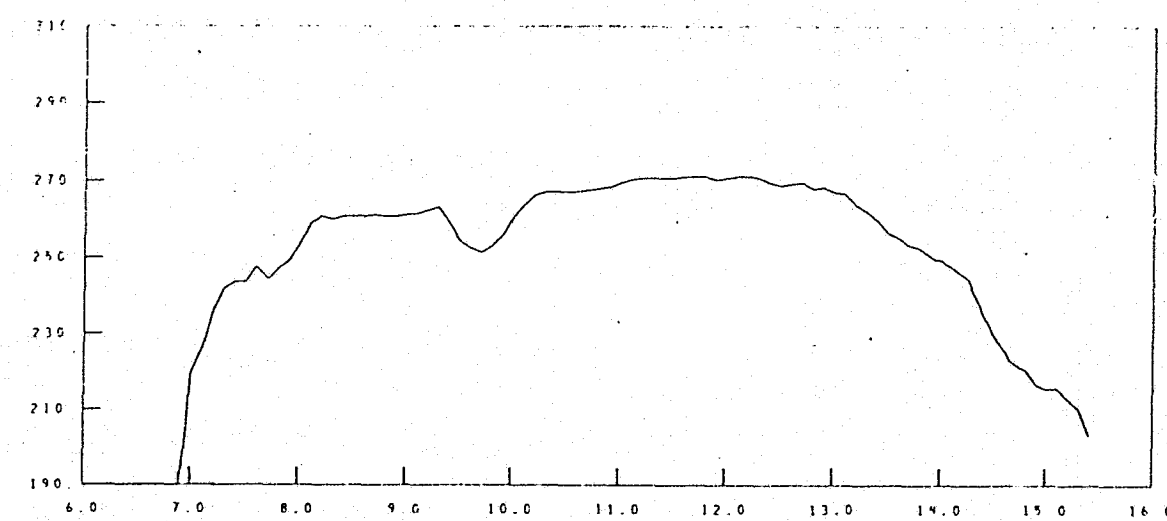
LONGITUDE

79.85



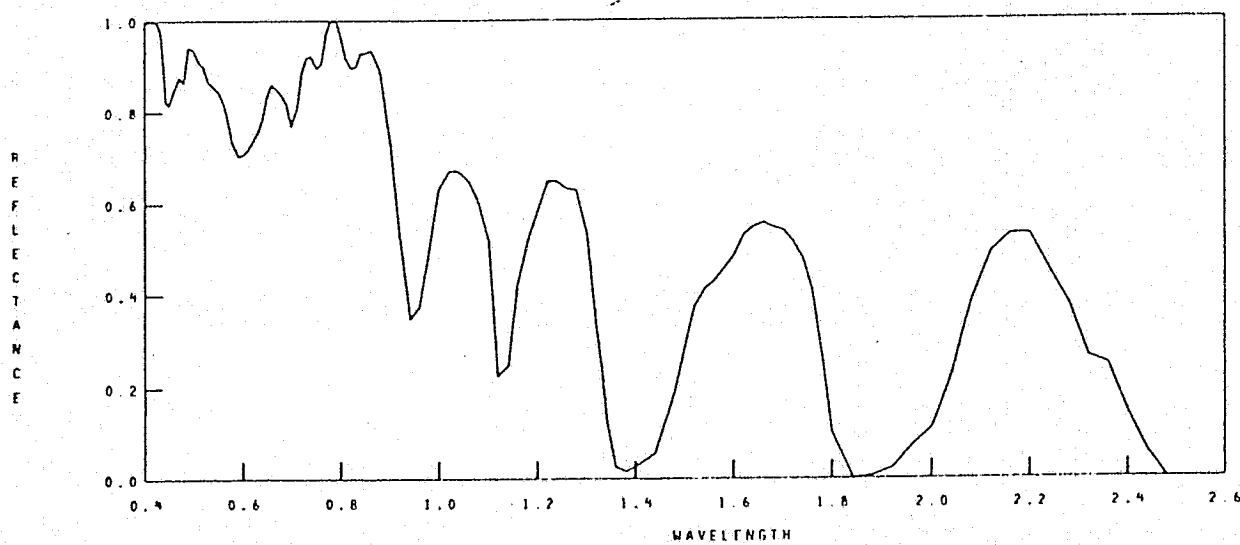
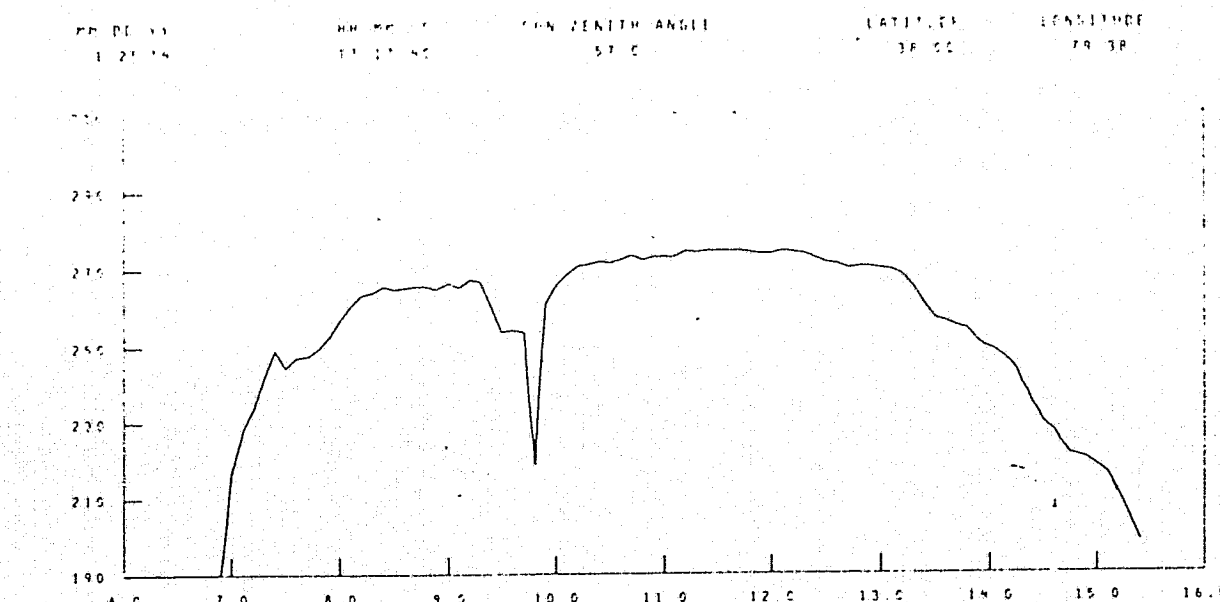
A6-60

S191 DATA 39

MM DD YY
125 74HH MM SS
17 17 37SPN ZENITH ANGLE
57.1LATITUDE
38.11
LONGITUDE
79.56

A6-61

1961 DATA 42



A6-62

5191 DATA 46

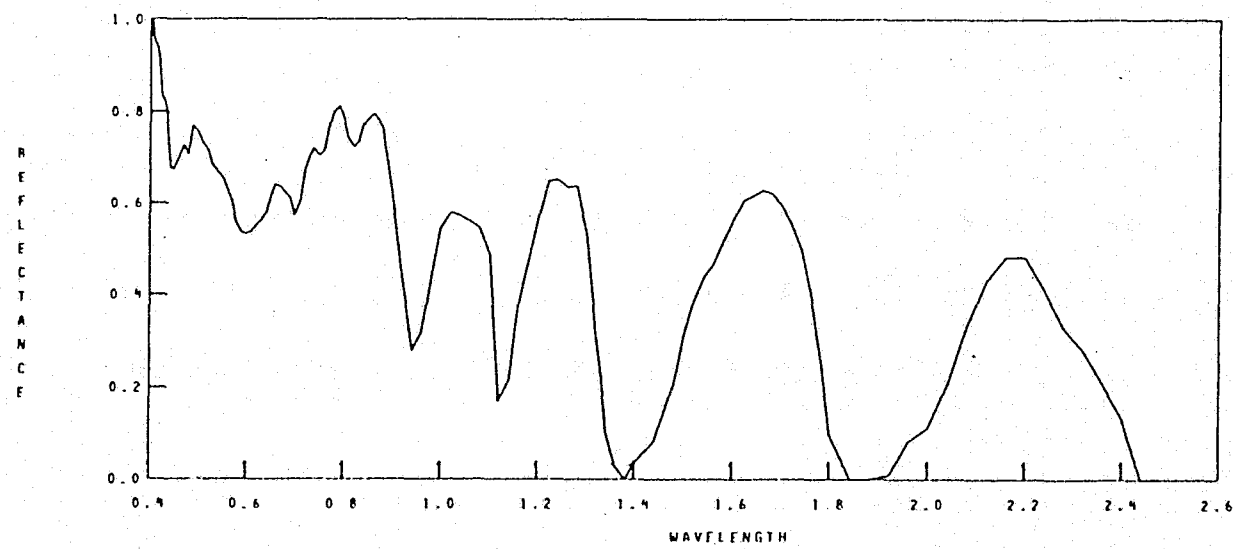
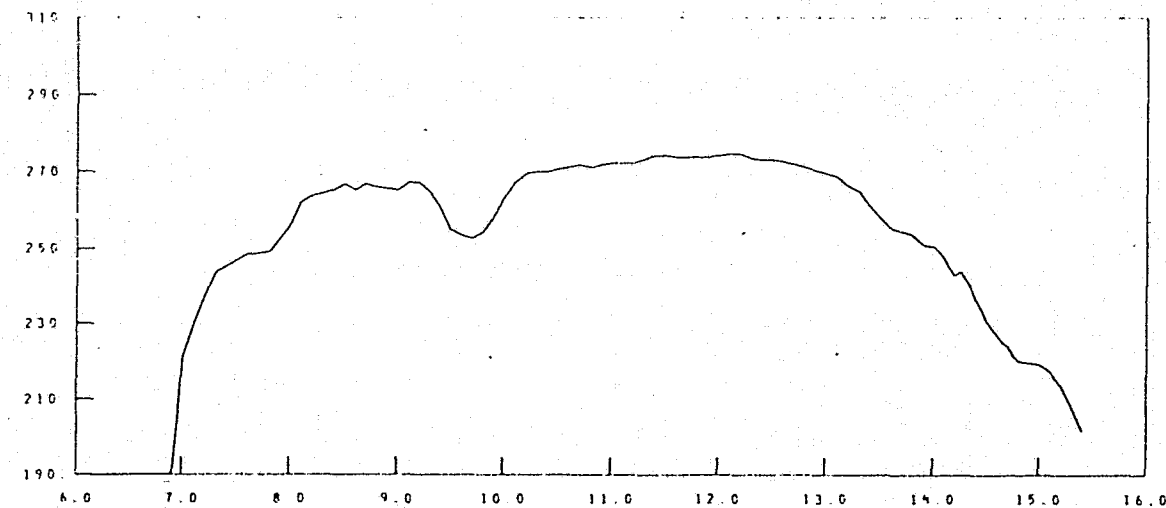
MM DD YY
1 25 74

HH:MM:SS
17:17:55

SUN ZENITH ANGLE
56.8

LATITUDE
37.83°

LONGITUDE
79.10



A6-63

5191 DATA 56

FM DD YY

12 74

HH MM SS

17 17 48

SUN ZENITH ANGLE

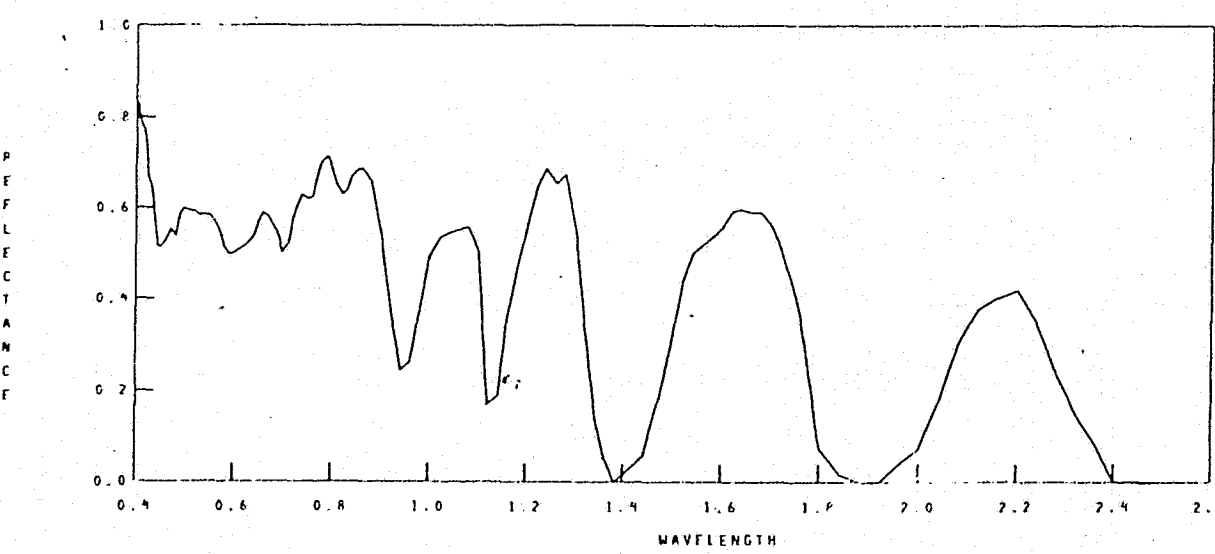
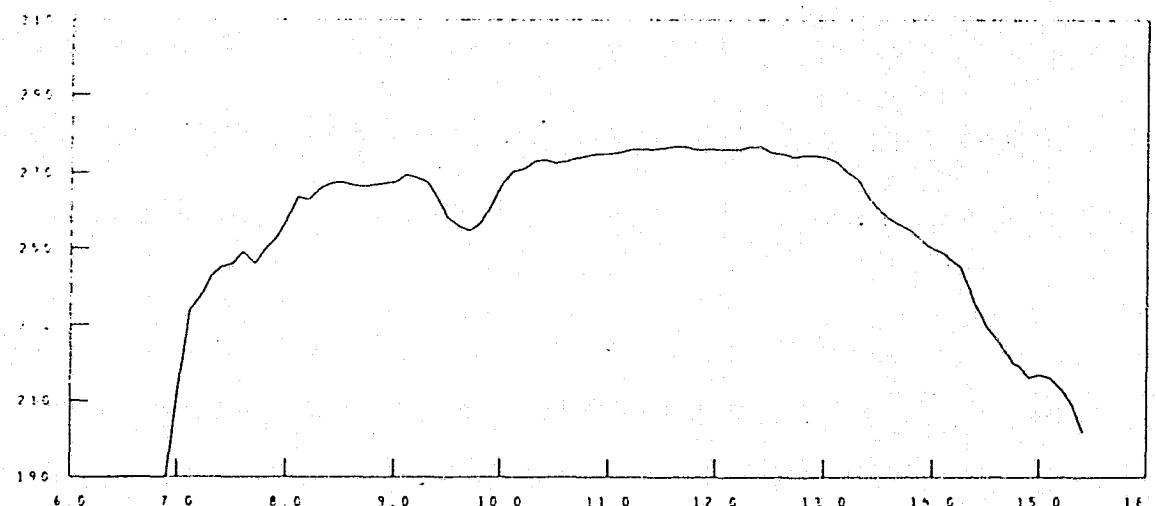
56.6

LATITUDE

37.69

LONGITUDE

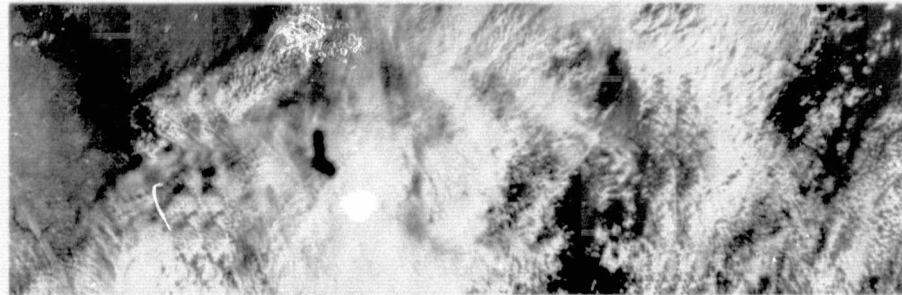
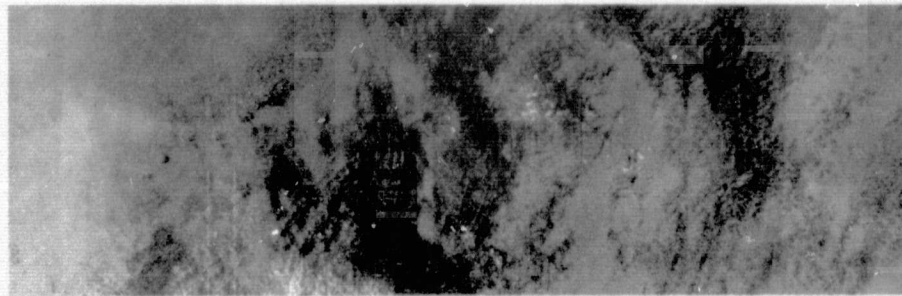
78.88



A6-64

DAY 031
1974

DATA
MISSING

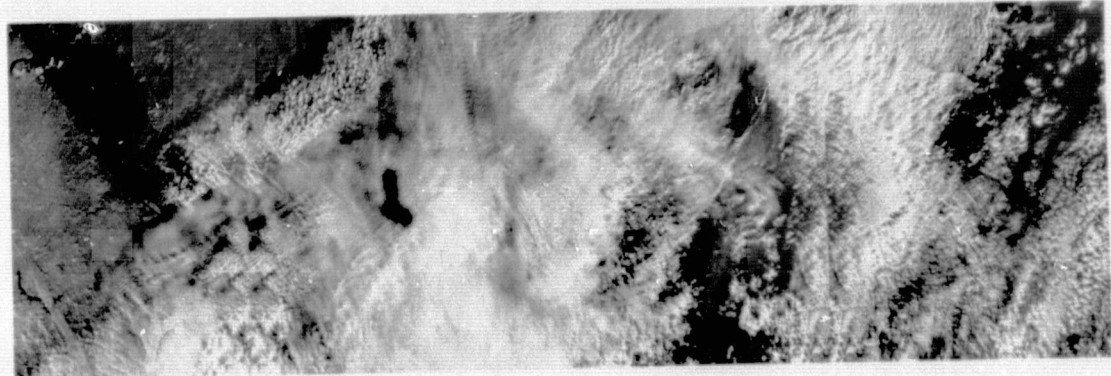
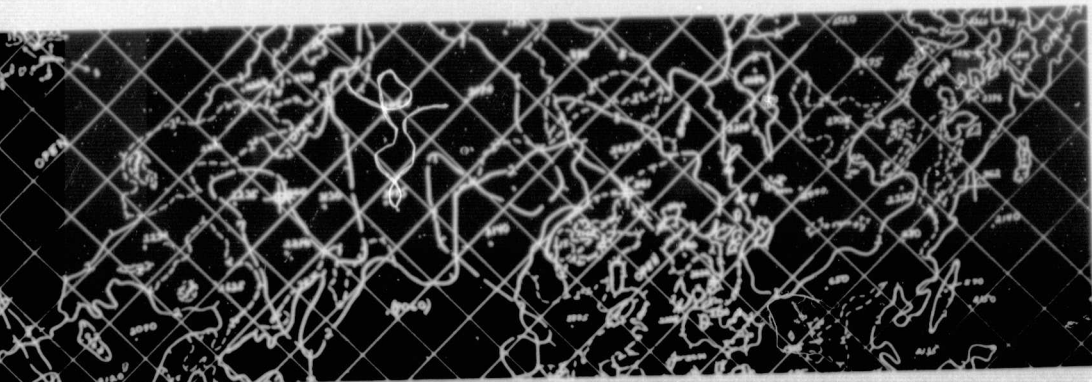


ORIGINAL PAGE IS
OF POOR QUALITY

A6-65

DAY 031
1974

DATA
MISSING



A6-65a

APPENDIX 2

Descriptions of Read and Analysis programs developed in support of
Skylab Investigation 556-1

(Addenda A-N give complete listings of the programs)